Aerodynamic simulations of offshore wind turbines by using a potential flow approach

Kristine Øren

Thesis for Master of Science Degree at the University
of Bergen, Norway

2024

Year:	2024
Title:	Aerodynamic simulations of offshore wind turbines by using a potential flow approach
Author:	Kristine Øren

Acknowledgements

I would like to thank my supervisors Cristian G. Gebhardt and Bruno A. Roccia for their constant support, insight, and knowledge during the writing of this thesis. I would like to especially recognize Bruno's and Cristian's work on the `UVLMeshGen` and `VLMSim` and for allowing and trusting my contribution to this project. It has been truly interesting and insightful to work with them in the past year.

I also wish to thank my family, friends, and fellow students for their support and encouragement. A special thanks goes to my mother and father, who have always been and continue to be very supportive and positive.

Abstract

This thesis explores the aerodynamic performance of floating offshore wind turbines (FOWTs) using a potential flow approach. The primary objective is to understand how the output power of an FOWT is affected by imposing different motions on the substructure. To this end, I employ an aerodynamic model based on the well-known unsteady vortex-lattice method (UVLM) to simulate the aerodynamic behaviour of the turbines in combination with a UVLM-oriented mesh generator (`UVLMeshGen`, developed at the University of Bergen) to build the aerodynamic grids. As part of this thesis, I have also integrated into `UVLMeshGen` the capacity of: meshing spar-like substructures, generating boundary surfaces intended for representing sea waves, and the kinematics associated with both the substructure's motion and sea waves.

Initially, the aerodynamic model of fixed and floating offshore wind turbines were validated against well-established benchmarks, including the NREL 5 MW, DTU 10 MW RWT, and Sandia 13.2 MW turbines. Following this, various motion scenarios were simulated to investigate the effects of individual and combined heave, surge, and wind turbine pitch motions on the power output. The results showed that the surge motion has the most significant impact on the power, while the heave motion has the least. However, the heave motion greatly affects the shape of the wake.

In addition, I analyze the effect of including sea waves, as a boundary surface with imposed kinematics, on the output power of stand-still FOWTs. The findings indicate that higher wave amplitudes produces a slight increase in power output, *the so-called blocking effect in aeronautics*. Such findings undoubtedly require further investigations in this direction to fully understand and characterize such a phenomenon.

Finally, simulations of multiple FOWTs demonstrated the importance of considering wake interactions when designing wind farm layouts. FOWTs placed in close proximity showed reduced power output due to wake interference, highlighting the need for accounting wake interactions when optimizing wind farm layouts and operating wind farms.

This research contributes to the field of renewable energy by enhancing the predictive capabilities of aerodynamic simulations for FOWTs. It provides a framework for future studies to incorporate more complex wave-structure interactions and optimise the design and placement of floating wind turbines to maximise the power production.

Contents

Chapter 1

Introduction

1.1 State of the art

In the last decades, wind energy has become an increasingly important source of renewable energy. There has been a significant increase in the scale of wind turbines (WTs), and some turbines such as the Vestas V236-15.0MW prototype are to be installed offshore [1]. Offshore wind has become a highly relevant energy source due to stable wind conditions found at sea [2]. Pioneer projects such as Horns Rev in Denmark have shown potential for steady power extraction with a rated power of 160 MW comprising 80 WTs [3], and more recently, the Hywind Tampen project for floating wind energy in the North Sea with 11 WTs and a total system capacity of 88 MW [4]. Offshore wind projects are currently being developed at larger scales worldwide [5].

One of the key challenges of this technology is the accurate characterization of the WT loads under flow conditions [6]. There are many ways to do this; from basic approaches such as blade element momentum (BEM) theory to complex models using computational fluid dynamics (CFD) techniques.

On one hand, the BEM Theory is a well-recognized method for the computation of the forces acting on the blades of a WT. This method is developed from momentum theory and blade element theory [7]. The theory simplifies the airflow analysis by assuming steady two-dimensional flow across segmented rotor blades, neglecting the influence of neighbouring segments and radial airflow variations. It does not account for dynamic effects like wind shear or turbulence, impacting rotor performance and stability. To improve its precision, corrections are made to account for these simplifications, as well as corrections for tip and hub vortices, non-stationary flow, large induction factors, and non-perpendicular incident flow [7], [8].

Figure 1.1 shows an actuator disk model used in BEM theory. The streamtube is where the incoming velocity V_∞ is analysed, the actuator disk is the surface that extracts energy from the incoming wind, followed by the downstream region where the wind velocity is reduced due to the extraction of energy. The flow velocity behind the actuator disk is denoted by V_w and is mainly associated with the flowfield downstream the wind turbine (i.e. in the wakes) [9].

Despite its computational efficiency and simplicity, BEM's effectiveness is constrained under certain conditions, therefore more complex methods for accurate analysis could be necessary. The work presented in [10] concludes that although BEM has a high computational efficiency, it is unreliable in modelling WTs at yawed configurations, among other working conditions.

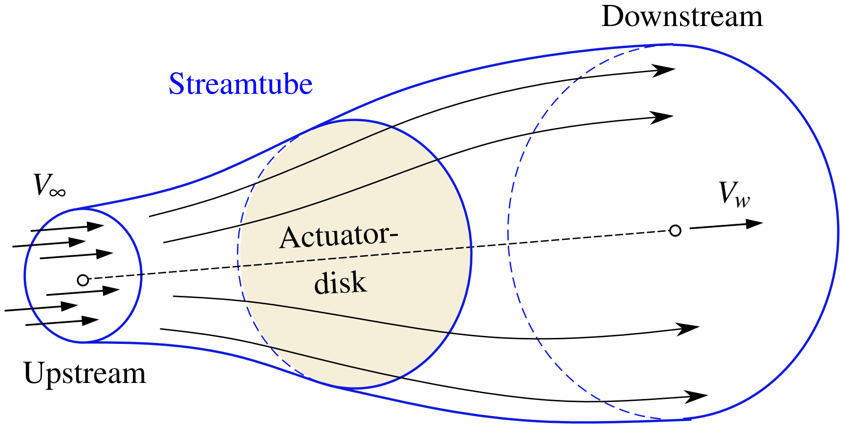

Figure 1.1: BEM example. Taken from [11].

On the other hand, the CFD provides a detailed description of the entire flow field. CFD methods are often very accurate but require significant computational resources. The governing equations for fluid flow are solved with CFD, typically the Navier-Stokes equations, numerically over a discretised domain. In solving these equations, numerical methods are applied to convert the partial differential equations into algebraic equations. Typically, this is done using the finite-volume method, the finite element method, or the finite difference method [12]. Figure 1.2 shows an example obtained by using a large-eddy simulation (LES) technique applied to a wind farm (where LES is a subset of CFD techniques).

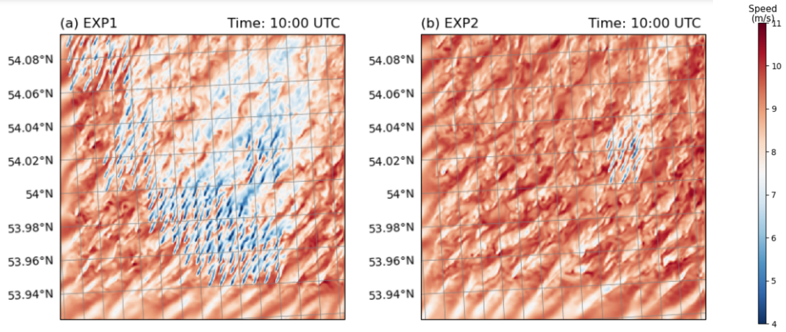

Figure 1.2: CFD simulation example: instantaneous 90-meter wind speed simulated by WRF-SADLES for the Alpha Ventus wind farm with (EXP1) and without (EXP2) the surrounding wind farms. Permission obtained from [13].

As an intermediate option between BEM and CFD approaches, I can mention the methods based on potential flows, in particular, the well-known unsteady vortex-lattice method (UVLM). This method has proven to be a more than a viable option, offering an excellent trade-off between precision and computational cost [14]. In addition, UVLM has been recognised as a good solver in the context of high geometric complexity and the presence of large displacement/rotations [15], [16], [17], [18]. Although this method is well-established and has been used to study several engineering applications (micro-air-vehicles, morphing wings and wind-turbines, among others), UVLM-based solvers require a detailed geometric description of lifting and non-lifting surfaces. Such requirements can become very tedious to satisfy when dealing with large problems characterized by highly complex geometries, since there are, in general, no programs to construct aerodynamic meshes. In this regard, Roccia et al. [19] developed a UVLM-oriented mesh generator intended for onshore wind farms, called `UVLMeshGen` (which stands for UVLM mesh generator). The `UVLMeshGen` has up until this point only accounted for onshore wind turbines. In light of the recent development of FOWTs, the main objectives of this work are to modify `UVLMeshGen` by including the substructure mesh, implementing the kinematics associated with the substructure, and implementing sea waves (as boundary surfaces) and its kinematics. The substructure is modelled based on the Equinor spar seen in Figure 1.3. The scale of this turbine is 1:165 and is a replica of the Hywind Tampen WT [4]. Further, to analyse the system, the already existing software called `VLMSim` (which stands for vortex-lattice method–simulation) is used. This in-house code is an aerodynamic simulator built upon the UVLM method [14].

Figure 1.3: Hywind Tampen WT scale replica, delivered to Bergen Offshore Wind Centre (BOW-UiB) by Equinor.

1.2 Research Question

If FOWTs are to be used more frequently to extract energy from the wind, it is important to have tools to best predict their aerodynamic performance. In the case of FOWTs there is an “extra ingredient” affecting the power production of the turbine: *the motion of the wind turbine caused by sea waves*. While onshore and non-floating offshore wind turbines are installed on structures fixed to the seabed (e.g. monopiles and jacket substructures, among others), the FOWTs may experience small-to-moderate displacements/rotations due to the sea waves. The movement of the turbine induced by the waves could cause the power output to change, which is crucial to take into account. Therefore, my main research question reads: *How is the power output of a FOWT affected when imposing motions on its substructure?* To this end, this thesis addresses the following specific objectives:

- Generate the aerodynamic grid of spar-like substructures as well as wave meshes (as boundary surfaces) using the linear wave theory.
- Implement the spar and wave grids into the existing mesh generator program `UVLMeshGen`, and gain expertise as user.
- Describe the kinematics of the whole FOWT considering the substructure’s motion and implement it into the `UVLMeshGen`.
- Create simulation scenarios based on: *i*) prescribed motions for the heave, surge and pitch, *ii*) different sea wave surfaces to investigate its influence on the turbine’s power production, and finally *iii*) two different offshore wind farms composed by two FOWTs.
- Carry out intensive aerodynamic simulations for all the considered scenarios by using the in-house aerodynamic solver called `VLMSim` [14].
- Analyse the results obtained from the numerical simulations and draw conclusions based on a critical thinking.

To my knowledge, there are few public available programs that are able to account for the motions that a wave would typically impose on FOWTs. It is my wish that the academic and industrial sectors have the software necessary to properly assess FOWT. Figure 1.4 presents a diagram that explains how the aerodynamic simulation framework adopted in this thesis works, the `UVLMeshGen` generates all the necessary meshes and input data that will then be used by the flow solver `VLMSim`. As output, the `VLMSim` provides the spatio-temporal evolution of the wakes and the pressure jump across the lifting surfaces (the blades). From this output data, I compute later, by using an in-house post-processor, the power generated by the WT as well as thrust force on the wind turbine rotor.

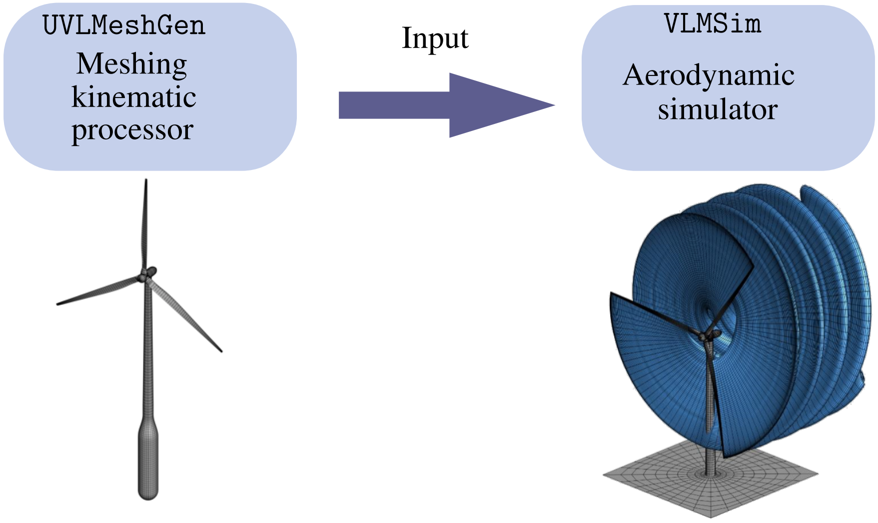

Figure 1.4: Aerodynamic simulation framework schematic.

In summary, this thesis aims to contribute to the `UVLMeshGen` by adding the following capacities: *i*) generation of spar-like substructures and sea waves (as boundary surfaces) aerodynamic grids, and *ii*) a full description of the kinematics for offshore wind turbines. In addition, an important part of this thesis is related to the design of several simulation scenarios considering different motion patterns for the substructure, sea waves and offshore wind farms. These cases are intended to shed a little more light on how power production and thrust forces are affected by imposing different motion patterns on the substructure. To the best of our knowledge, the author and her supervisors, the results reported here contain enough novelty to be published in a journal article.

Chapter 2

Aerodynamics and Waves

In this chapter, I will introduce various elements of the aerodynamic computational framework. To begin with, I will provide a brief overview of general aerodynamic theory. Further, there is a concise explanation of the aerodynamic model adopted here and its discrete version, the so-called Unsteady Vortex-Lattice Method. Lastly, the linear wave theory, which is used to model the waves in this work, is presented.

2.1 Wind Power

Wind turbines generate power through the conversion of the kinetic energy of the wind into mechanical power. The mechanical energy is converted into electrical energy by the generator. The power available in the wind is given by:

$$P_{wind} = \frac{1}{2}\rho A_{\mathrm{rotor}} V_{\infty}^{3}, \tag{2.1}$$

where P_{wind} is the power in Watts, ρ is the air density, typical kg/m^3, A_{rotor} is the area of the rotor in squared meters and, V_{∞} the free stream velocity in m/s. In reality, only a fraction of the power can be extracted by the WT. The efficiency of the WT is given by the power coefficient (C_p) which has a maximum efficiency ($C_{p,max}$), namely *Betz limit* [20] [21]. The extracted power from the WT can be expressed as:

$$\begin{gathered} P = P_{\mathrm{wind}} C_p, \\ \text{where} \quad C_p \leq \frac{16}{27}. \end{gathered} \tag{2.2}$$

As the incoming wind approaches the airfoil, it has to move along either the upper or lower surface. To generate lift, the air particles should meet simultaneously at the trailing edge of the aerofoil, so that the particles moving along the lower surface must have a lower velocity for this to occur, as seen in Figure 2.1. As a consequence, a higher pressure is formed on the lower surface, according to Bernoulli's principle, generating lift [22].

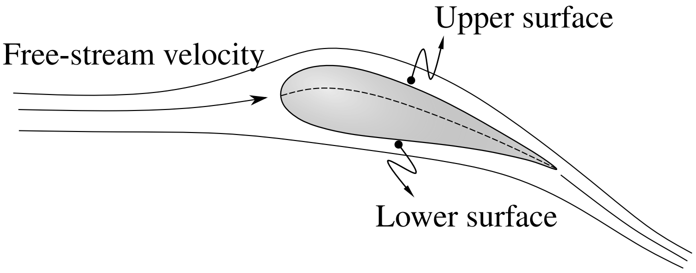

Figure 2.1: Flow pattern around an airfoil.

A section of a WT blade is described in Figure 2.2. The rotation plane is orientated perpendicular to the axis of the rotor shaft, the chord line connects the leading and trailing edges, where the air enters and leaves the blade, respectively. L represents the lifting force, perpendicular to the relative airflow, and D represents the drag force, parallel to the relative airflow. In addition, Ω is the angular velocity of the WT rotor in RPM (revolutions per minute) and r is the radial distance along the blade. The product of Ω and r gives the tangential velocity of the blade section. V_{total} is made up of the sum of vectors of Ωr and V_∞, the angle between the chord line and V_{total} is the angle of attack (AoA) and is denoted by α, ϕ is the total angle, composed of α and θ. Finally, θ is composed of θ_p and β, where θ_p is the pitch angle and β is the twist angle, accounting for the geometric twist of the blade [23].

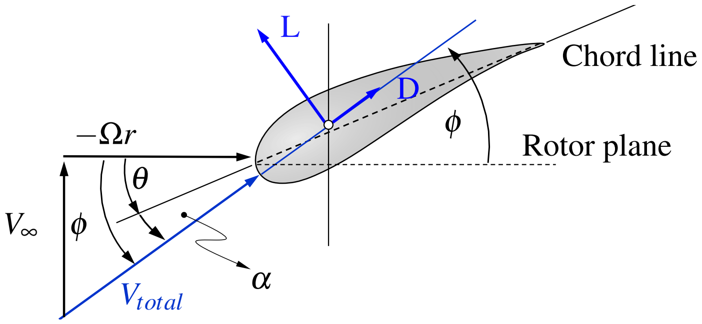

Figure 2.2: Description of velocities and forces on a typical WT blade section.

As the wind passes through the rotor, a wake forms behind the WT. This wake, characterised by reduced wind speeds and increased turbulence compared to V_∞, is a signature of the lifting forces acting on the rotor blades. This phenomenon is especially important to consider when placing multiple WTs in a wind farm. The presence of an upstream WT affects the airflow and consequently decreases the quality of V_∞ experienced by a downstream WT [24].

2.1.1 Corrections

It is often necessary in aerodynamic models to apply some corrections to better account for physical phenomena such as the reduction of lift near the blade tips due to vortex formations. This is automatically accounted for when using UVLM-based solvers. Figure 2.3 shows the tip vorticies of a WT [19].

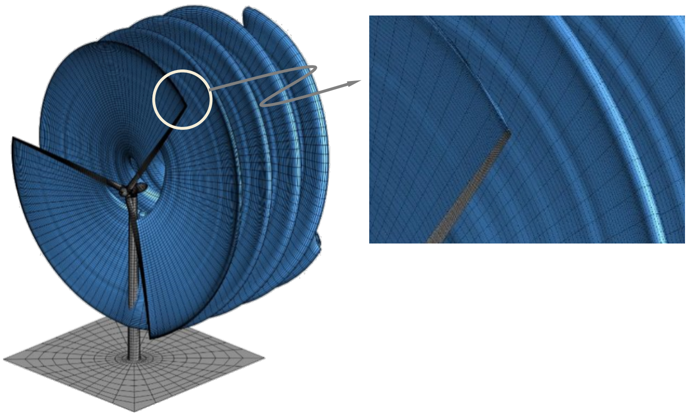

Figure 2.3: Numerical simulation of a complete wind turbine rotor including rotor tip vortices, where tip vortices are visible.

2.2 Aerodynamic model

Consider a body $\mathscr{B}$ with boundary $\partial\mathscr{B}$ that is in a fluid stream. The regions close to the solid surfaces are called boundary layers (BL). For boundary layers to form, the Reynolds number (*Re*) must be sufficiently large. For *Re* to be considered large, the inertial forces must be significantly greater than the viscous forces. Part of the vorticity in the BL is shed downstream into the flowfield, which forms the wakes behind the body. When $Re \to \infty$, the thickness of the BLs and the wakes tends to zero. This assumption allows for the BLs and wakes to be represented as continuous zero-thickness sheets of vorticity, respectively. Furthermore, the flow is considered incompressible due to the assumption of a low subsonic flow, which has a low Mach number. Following these assumptions, the unknown pressure and velocity fields are governed by the *Euler equation* and the *Continuity equation* for incompressible flows,

$$\partial_t \mathbf{V}(\mathbf{r},t) + (\mathbf{V}(\mathbf{r},t)\cdot\nabla)\mathbf{V}(\mathbf{r},t) = -\frac{1}{\rho}\nabla p(\mathbf{r},t), \tag{2.3}$$

$$\nabla\cdot\mathbf{V}(r,t) = 0, \tag{2.4}$$

where $\mathbf{r}$ is the position vector of a fluid particle at time t, $\mathbf{V}(\mathbf{r},t)$ is the absolute velocity of a fluid particle, ρ is the fluid density (assumed to be constant), $p(\mathbf{r},t)$ is the pressure field, $\partial_t(\cdot)$ stands for partial time derivative, and $\nabla(\cdot) = \partial_x(\cdot)\hat{\mathbf{i}} + \partial_y(\cdot)\hat{\mathbf{j}} + \partial_z(\cdot)\hat{\mathbf{k}}$ is a vector differential operator in $\mathbb{R}^3$.

The left-hand side (LHS) of the Euler equation describes the time derivative of the velocity $\partial_t\mathbf{V}(\mathbf{r},t)$ and the convective acceleration denoted as $(\mathbf{V}(\mathbf{r},t)\cdot\nabla)\mathbf{V}(\mathbf{r},t)$. The right-hand side (RHS) represents the forces due to pressure gradients, $-\frac{1}{\rho}\nabla p(\mathbf{r},t)$. Essentially, the Euler equation describes the change in velocity of a fluid particle due to the pressure forces acting on it.

The Continuity Equation describes the conservation of mass. The fluid density is constant within the flow field for incompressible fluids as they move through the velocity field, so the divergence of the velocity field $\mathbf{V}$ is zero.

By applying the Helmholtz decomposition, the velocity field $\mathbf{V}(\mathbf{r},t)$ can be described as the sum of the gradient of a scalar potential $\varphi(\mathbf{r},t)$ and the curl of a vector potential $\boldsymbol{\Psi}(\mathbf{r},t)$ as follows:

$$\mathbf{V}(\mathbf{r},t) = \nabla\varphi(\mathbf{r},t) + \nabla\times\boldsymbol{\Psi}(\mathbf{r},t). \tag{2.5}$$

The Helmholtz decomposition assumes that the gradient of a scalar field is irrotational and that the curl of a vector field has zero divergence. This property is inherent in the Helmholtz decomposition. Any vorticity in the velocity field is contained in the vector potential component. Applying the decomposition to the continuity equation and considering that $\nabla\cdot(\nabla\times\boldsymbol{\Psi}(\mathbf{r},t)) = 0$ (due to the divergence of a curl always being zero), we are left with the divergence of the gradient of the scalar potential, which must also be zero. The resulting equation is known as the *Laplace equation* for the scalar potential:

$$\nabla^2\varphi(\mathbf{r},t) = 0. \tag{2.6}$$

Furthermore, by using Eq. (2.5) along with the definition of the vorticity field $\boldsymbol{\Omega}(\mathbf{r},t) = \nabla\times\mathbf{V}(\mathbf{r},t)$ and the condition that $\nabla\cdot\boldsymbol{\Psi}(\mathbf{r},t) = 0$, I obtain the well-known *Poisson equation* for the vector potential:

$$\nabla^2\boldsymbol{\Psi}(\mathbf{r},t) = -\boldsymbol{\Omega}(\mathbf{r},t). \tag{2.7}$$

This equation relates the vector potential and the vorticity field. Although the Laplace and the Poisson equations do not have direct time-dependent terms, these are introduced through the boundary conditions (BCs). In potential flows there are two BCs, namely the regularity at infinite condition and the non-penetration condition.

The regularity at infinite condition requires that the velocity field associated with the flow disturbance, due to the body motion through the fluid, decays far away from the body and its wakes seen as:

$$\lim_{\|\mathbf{r}-\mathbf{r}_B\|\to\infty} \|\mathbf{V}_B(\mathbf{r},t)+\mathbf{V}_W(\mathbf{r},t)\| = 0, \tag{2.8}$$

where $\|\mathbf{r}-\mathbf{r}_B\|$ is the distance between an arbitrary point $\mathbf{r}$ and a point $\mathbf{r_B}$ that belongs to $\partial\mathscr{B}$. The velocity induced by the bound vortex sheets is represented by $\mathbf{V}_B$ and the velocity induced by the free vortex sheets (wakes) is represented by $\mathbf{V}_W$. The non-penetration condition ensures that no fluid flows through the body as the body is considered solid. The condition requires that the normal component of the fluid velocity relative to the body vanishes identically over the whole surface of the body:

$$[\mathbf{V}_\infty+\mathbf{V}_B(\mathbf{r},t)+\mathbf{V}_W(\mathbf{r},t)-\mathbf{V}_S(\mathbf{r},t)]\cdot\hat{\mathbf{n}}(\mathbf{r},t) = 0. \tag{2.9}$$

As the body moves and interacts with the fluid, it induces a velocity field $\mathbf{V}_B(\mathbf{r},t)$, representing the perturbation caused by the body. Additionally, there may be other velocity disturbances within the fluid, denoted by $\mathbf{V}_W(\mathbf{r},t)$. The body surface velocity is denoted by $\mathbf{V}_S(\mathbf{r},t)$. The normal vector to the boundary $\partial\mathscr{B}$ is denoted as $\hat{\mathbf{n}}$. In addition to the boundary conditions (BCs) accounted for, the Kelvin and Kutta conditions must also be satisfied. The Kelvin circulation theorem states that for an inviscid barotropic fluid with conservative body forces, the circulation Γ around any closed loop C that moves with the fluid remains constant over time. This is mathematically expressed as $\frac{d\Gamma(t)}{dt} = 0$ where $\Gamma(t)$ is the circulation at time t, provided that the loop follows the fluid motion. Kutta's condition states that the flow will leave the trailing edge smoothly and therefore the pressure on the upper and lower surfaces must vanish along the edges where separation occurs, also called separation zones, SZs. This condition forces the fluid particles in the SZ to leave $\mathscr{B}$ at the local velocity flow, resulting in the well-known vorticity shedding phenomenon. The velocity field is obtained by solving the Poisson PDE. This results in the well-known Biot-Savart law, which takes the following form for three-dimensional flows:

$$\mathbf{V}(\mathbf{r},t) = \frac{1}{4\pi}\int_{V(s,t)} \frac{\boldsymbol{\Omega}(s,t)\times(\mathbf{r}-\mathbf{s})}{\|\mathbf{r}-\mathbf{s}\|^3}\,dV(\mathbf{s},t), \tag{2.10}$$

where $\mathbf{r}$ is the target point, $\boldsymbol{\Omega}(\mathbf{s},t)$ is the distributed vorticity located within a compact region $V(\mathbf{s},t)\subset\mathbb{R}^3$, and where $\mathbf{s}$ is a position vector of a point belonging to $V(\mathbf{s},t)$. Additionally, this equation can be adapted to describe vortex lines, which are scenarios where a finite amount of vorticity is distributed over a two- or three-dimensional region. Despite this, the circulation, or strength, denoted by Γ, remains finite and unchanging. Consider a small volume element dV of this vortex line, which resembles a cylinder with a differential cross-sectional area dA and a differential length ds. Performing an integration along the filament's length results in the widely recognised Biot–Savart law specialised for an arbitrary vortex curve $C(\mathbf{s}) \subset \mathbb{R}^3$:

$$\mathbf{V}(\mathbf{r},t) = \frac{\Gamma}{4\pi} \int_{C(\mathbf{s},t)} \frac{\hat{\mathbf{T}}(\mathbf{s},t) \times [\mathbf{r} - \mathbf{s}(\mathbf{s})]}{|\mathbf{r} - \mathbf{s}(\mathbf{s})|^3} ds(\mathbf{s}), \tag{2.11}$$

where $\hat{\mathbf{T}}(\mathbf{s})$ is the unit tangent vector to $C(\mathbf{s})$.

2.2.1 Convection of the Wakes

Fluid particles are swept away from the sharp trailing edge of a body $\mathscr{B}$ into its wake. Over time, as the wake moves far downstream, its influence on the flow around the body decreases. This can be described as fading memory, because the effects of the wake diminish as it travels further away. The location $\mathbf{r}_f(t)$ of any fluid particle at a given time t can be determined by integrating the local fluid velocity $\mathbf{V}(\mathbf{r}_f(\tau),\tau)$ over time. τ is a dummy integration variable. The term ”dummy integration variable” refers to an auxiliary variable used to facilitate the integration process without affecting the final outcome. The local fluid velocity is the sum of the velocity induced by the body, the velocity induced by the wake, and the free stream velocity:

$$\mathbf{r}_f(t) = \int_0^t \mathbf{V}(\mathbf{r_f}(\tau),\tau)\, d\tau, \tag{2.12}$$

$$\text{where } \mathbf{V}(\mathbf{r_f},t) = \mathbf{V_B r_f},t) + \mathbf{V_W},(\mathbf{r_f},t) + \mathbf{V}_\infty \tag{2.13}$$

2.2.2 Aerodynamic Loads

Assuming the absence of rotor forces within the body and considering that the flow field outside the boundary layers of $\mathscr{B}$ and its wakes is free of rotation, the Euler equations can be applied along a streamline. This process leads to the formulation of the Bernoulli equation in its unsteady form, seen as:

$$\begin{gathered}\int_{C(s)} \partial t(\mathbf{V} \times \boldsymbol{\Psi}) \cdot \hat{\mathbf{T}} ds + \frac{\partial \phi}{\partial t} \\ + \frac{1}{2}[\nabla\phi + \mathbf{V} \times \boldsymbol{\Psi}] \cdot [\nabla\phi + \mathbf{V} \times \boldsymbol{\Psi}] + \frac{1}{\rho} p(\mathbf{r},t) = E(t),\end{gathered} \tag{2.14}$$

where $E(t)$ is a spatially uniform function of time [25]. As the distance along a streamline from the point P_x on the surface of a body $\mathscr{B}$ to a reference point in the far field $||\mathbf{r}|| \to \infty$, several variables approach constant values or zero: $\phi \rightarrow \phi_\infty =$ constant, $p = \frac{p_\infty}{\rho} =$ constant, $\nabla \times \mathbf{\Psi} \rightarrow 0$, $\nabla\phi \rightarrow \mathbf{V}_\infty$ and $E(t) \rightarrow \frac{1}{2}\mathbf{V}_\infty \cdot \mathbf{V}_\infty + \frac{p_\infty}{\rho}$. After a few algebraic operations, the pressure jump across the lifting surface at point P_x is defined as:

$$\begin{aligned}\frac{D_p}{\rho} = &\int_L^U \left(\frac{\partial}{\partial t}(\nabla \times \mathbf{\Psi}) \cdot \hat{\mathbf{T}}(s)\right) ds + \left[\frac{\partial \phi}{\partial t}\rho\right]_U - \left[\frac{\partial \phi}{\partial t}\rho\right]_L \\ &+ \frac{1}{2}\left[(\nabla\phi + \nabla \times \mathbf{\Psi}) \cdot (\nabla\phi + \nabla \times \mathbf{\Psi})\right]_U \\ &- \frac{1}{2}\left[(\nabla\phi + \nabla \times \mathbf{\Psi}) \cdot (\nabla\phi + \nabla \times \mathbf{\Psi})\right]_L,\end{aligned} \tag{2.15}$$

where point L is below the vortex sheet at P_x, U is above the vortex sheet at P_x, and $D_p = (\rho)_L - (\rho)_U$. The reader is referred to [14] for a more detailed description of the theory behind the unsteady version of the Bernoulli equation.

2.2.3 Unsteady Vortex-Lattice Method

For UVLM-based computational implementations, the continuous bounded vortex sheets are discretised into a lattice of short straight vortex segments of circulation Γ. Such segments divide $\partial\mathscr{B}$ into a finite number of area elements B_k (also called panels or boundary elements). The subscript k defines the number of panels and implies that this should apply to all panels. The wakes emitted from the separation zones (trailing edges, wing or blade tips, and leading edges) are also represented by vortex lattice [26].

Often, the complete system is first divided into a collection of lifting and non-lifting surfaces. The entire body ∂B is the boundary of the entire system that is made up of the union of smaller boundaries B_i:

$$\partial B = \bigcup_{i=1}^{N_B} \partial B_i, \tag{2.16}$$

where N_B is the total number of discrete bodies in the system. Further, each individual surface boundary ∂B_i is decomposed into a finite set of boundary elements B_k^i:

$$B_i = \bigcup_{k=1}^{N_{pbi}} B_k^i, \tag{2.17}$$

where N_{pb_i} is the number of panels related to each sub grid ∂B_i. From this, the total number of panels N_{pb} of the whole surface ∂B is calculated as:

$$N_{pb} = \sum_{i=1}^{N_B} N_{pbi}. \tag{2.18}$$

In general, quadrilateral elements (QEs) are used as panels, as they work better than other elements for a UVLM approach [19] [16]. The edges of each B_k^i are represented by finite, straight vortex segments of circulation $\mathbf{\Gamma}(t)$. Their contributions to the velocity field are calculated by the following discrete version of Eq. (2.11):

$$V(\mathbf{r}^d;t) = \frac{\mathbf{\Gamma}(t)}{4\pi}\frac{(\mathbf{r}_1^d \times \mathbf{r}_2^d)}{\|\mathbf{r}_1^d\|\|\mathbf{r}_2^d\|}\frac{(\|\mathbf{r}_1^d\| + \|\mathbf{r}_2^d\|)}{\|\mathbf{r}_1^d\|\|\mathbf{r}_2^d\| + \mathbf{r}_1^d \cdot \mathbf{r}_2^d + (\delta_c(\|\mathbf{u}\|)^2}, \tag{2.19}$$

where $\mathbf{r}_1$ and $\mathbf{r}_2$ are the position vectors of the point where the velocity is evaluated relative to the end of the straight vortex segment $\mathbf{u} = \mathbf{r}_1 - \mathbf{r}_2$ and δ_c is a cut-off parameter [27]. This is introduced to modify the singular kernel in Eq. (2.11). This is to avoid the singularity that occurs when the point $\mathbf{r}$ is very close to the vortex curve, i.e. when $[\mathbf{r} - \mathbf{s}(s)]$ approaches zero [28] [29]. The cut-off radius δ_c can be further modified by including a time-dependent growth core-vortex model as follows:

$$\delta_c(t) = \sqrt{4\alpha_s\delta_v(t + t_0)}, \tag{2.20}$$

$$t_0 = \frac{r^2c_0}{4\alpha_s\delta_v}, \tag{2.21}$$

where $\alpha_v = 1.25643$ is the Ossen parameter, ν is the kinematic viscosity of air, t is the time elapsed since the vortex segment was shed into the wake, rc_0 is usually set to 10% of the vortex segment length, and δ_v represents the additional dissipation due to viscosity, which is defined in terms of the vortex segment circulation Γ. For a more detailed description, the reader is referred to [30] [31].

2.2.4 Aerodynamic influence coefficients

When using UVLM-based solvers, the main unknowns to be determined are the vortex segments intensities (circulations) on the bound-vortex lattices. To this end, The non-penetration boundary condition presented continuously in Eq. (2.9) is imposed at the control points (CP) in the geometric centres of each B_k^i. This results in a system of linear algebraic equations, which usually have time-varying coefficients. These systems can be expressed in terms of vortex-ring circulations $\mathbf{G}_j(t)$, substantially reducing the computational time when rings are used instead of segments [32]. Such vortex rings are obtained by considering that each panel is surrounded by a closed loop of vortex segments with the same circulation. In this way, each straight segment is made up of two loops. With these assumptions, the linear system takes the following form:

$$\begin{gathered}\sum_{j=1}^{N_{pb}} a_{ij}(t)\mathbf{G}_j(t) + \left[V_\infty^d + V_w^d(\mathbf{r}_i,t) - V_s^d(\mathbf{r}_i,t)\right]\cdot \hat{\mathbf{n}}_i(t) = 0,\\ i = 1,2,\ldots,N_{pb},\\ \mathbf{A}(t)\mathbf{G}(t) = \mathbf{RHS}(t),\end{gathered} \tag{2.22}$$

where $a_{ij}(t)$ are the aerodynamic influence coefficients, $\hat{\mathbf{n}}_i$ is the unit vector normal at the i-th CP, $\mathbf{A}(t)$ is the aerodynamic influence matrix, $\mathbf{G}(t)$ gather the unknown ring circulations, and $\mathbf{RHS}(t)$ is the right-hand side. $\mathbf{RHS}(t)$ gather the contributions of $\mathbf{V}_w$, $\mathbf{V}_\infty$ and $\mathbf{V}_s$ along the normal direction at each CP. The reader should note that $a_{ij}(t)$ represents the normal component of the velocity in the CP of the ith element associated with a vortex ring around the jth element having unit circulation [14].

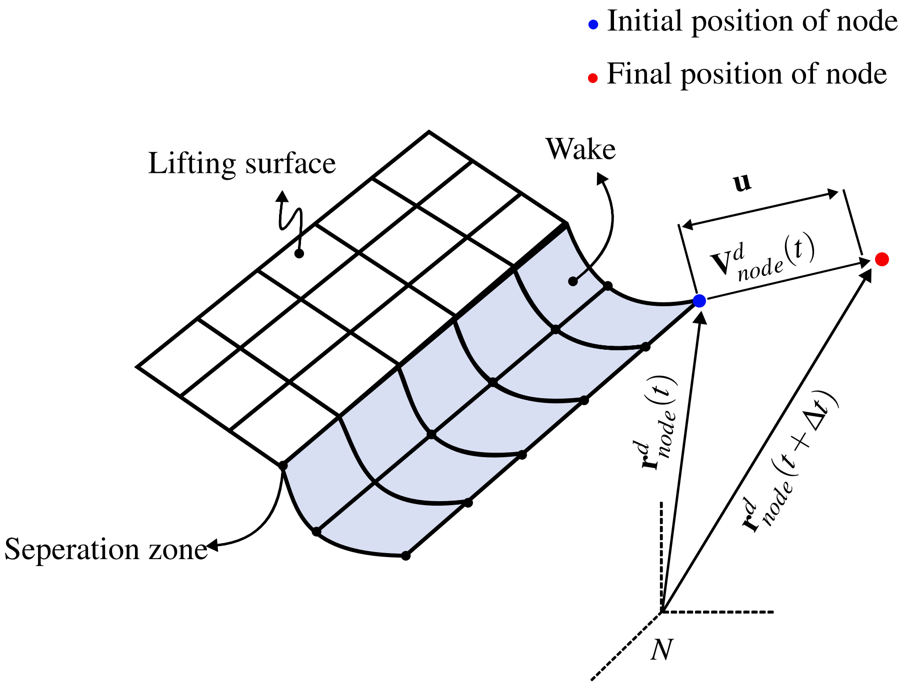

Figure 2.4: Description of the convection scheme for a point within the wakes.

2.2.5 Free-Vortex-Lattice Convection

In order to propagate the wake an explicit first-order method is applied. This uses quantities calculated at the previous time step and is given by:

$$\mathbf{r}^d_{\text{node}}(t+\Delta t) \approx \mathbf{r}^d_{\text{node}}(t) + \mathbf{V}^d_{\text{node}}(t)\Delta t, \tag{2.23}$$

where Δt is the time step. The subscript '*node*' is introduced to refer to the corners of the vortex segments. Figure 2.4 shows a convection procedure of how $\mathbf{r}$ evolves through time.

2.2.6 Aerodynamic Loads (Discretisation)

A discrete version of the pressure jump is presented. Next, the reader is referred to [14] for a detailed explanation of how to obtain the continuous version. The aerodynamic loads on the rotor blades are computed in three steps; 1) Calculating the pressure jump at the control point of each element using the unsteady Bernoulli Equation; 2) Computing the force at each element as the product of the pressure jump times the element area times the unit normal vector; 3) The resulting forces and moments are calculated as the vector sum of the forces and their moments about a common point. The velocity field is assumed to be divided mainly into two parts: $\mathbf{V}_B^d + \mathbf{V}_\infty^d$ associated with $\nabla\psi^d$ and $\mathbf{V}_w^d$ associated with $\nabla \times \psi^d$. The unsteady term due to the vector potential $\int \partial(\nabla \times \psi^d) \cdot \hat{\mathbf{T}}(s)\, ds$ is very difficult to handle in this form. Invoking the equivalence between a doublet and a vortex ring of constant circulation, the contribution of the free-vortex lattice can be considered as an analogous contribution of a discrete distribution of doublets [33] [14]. After some algebraic manipulations, the discrete version of the Bernoulli equation can be expressed as:

$$\begin{aligned}\frac{Dp^d}{\rho_F} = &\left[(\partial_t\phi^d + \partial_t\psi^d)\Big|_U - (\partial_t\phi^d + \partial_t\psi^d)\Big|_L\right] \\ &+\frac{1}{2}(\mathbf{V}_\phi^d + \mathbf{V}_\psi^d)\cdot(\mathbf{V}_\phi^d + \mathbf{V}_\psi^d)\Big|_U \\ &-\frac{1}{2}(\mathbf{V}_\phi^d + \mathbf{V}_\psi^d)\cdot(\mathbf{V}_\phi^d + \mathbf{V}_\psi^d)\Big|_L,\end{aligned} \tag{2.24}$$

$$\begin{aligned}=&[(\partial_t\phi^d + \partial_t\psi^d)|_U - (\partial_t\phi^d + \partial_t\psi^d)|_L] \\ &+\frac{1}{2}\left(\mathbf{V}_U^d\cdot\mathbf{V}_U^d - \mathbf{V}_L^d\cdot\mathbf{V}_L^d\right),\end{aligned} \tag{2.25}$$

where D_p^d is the discrete pressure jump, $\mathbf{V}_U^d = (\mathbf{V}_\phi^d + \mathbf{V}_\psi^d)|_U$, and $\mathbf{V}_L^d = (\mathbf{V}_\phi^d + \mathbf{V}_\psi^d)|_L$.

After some algebraic manipulation, the pressure jump for each panel B_k is obtained as:

$$D_k^d = \rho\left[\mathbf{V}_{m,k}^d - \mathbf{V}_k\right]\cdot\Delta\mathbf{V}_k^d + \rho\frac{\mathbf{G}_k(t) - \mathbf{G}_k(t-\Delta t)}{\Delta t}. \tag{2.26}$$

The vector force on the boundary element B_k is calculated as the product of Eq. (2.26) times the element area A_k times the normal vector located at the CP_k,

$$\mathbf{F}_k = Dp_k^d A_k \hat{\mathbf{n}}_k. \tag{2.27}$$

This section has provided a description of the UVLM applied in this work. The reader is referred to [27] for a more detailed description of the UVLM and the discretisation.

2.3 Wave Theory

This section describes the process of modeling waves as a boundary layer to the FOWT simulations. I will not be solving the equations of waves, but rather impose the motion of the waves on the FOWT. It is beyond the scope of this thesis to consider the solutions and so the inclusion of the waves are in order to give the reader an idea of how a boundary layer affects an FOWT. In modelling ocean gravity waves, we assume that the water is incompressible and that the effects due to capillarity and viscosity are negligible. Internal waves are also neglected, as we assume a constant density. The velocity vector **u** is given by the velocities of the components in the directions x, y, and z. It is assumed that the velocity field can be described by a velocity potential Φ and that the fluid velocity **u** is obtained from the gradients of the velocity potential. Under the assumptions that the fluid is incompressible and irrotational, the potential will satisfy the Laplace equation throughout the fluid:

$$\mathbf{u} = \nabla\Phi, \tag{2.28}$$

$$\nabla^2\Phi = \frac{\partial^2\Phi}{\partial x^2} + \frac{\partial^2\Phi}{\partial y^2} + \frac{\partial^2\Phi}{\partial z^2} = 0. \tag{2.29}$$

The Laplace equation is solved by imposing a set of boundary conditions. Assuming that the waves propagate in the positive x direction, the velocity in the y direction is zero, $\frac{\partial\Phi}{\partial y} = 0$, and there is zero vertical velocity at the bottom, assuming the bottom is horizontal so that $\frac{\partial\Phi}{\partial z} = 0$ at $z = -d$.

There are two boundary conditions to be imposed on the free surface: one kinematic and one dynamic. The kinematic condition implies that once the particles are on the free surface, they will remain there; i.e., the particles on the free surface must follow the motion of the free surface. This can be expressed as follows:

$$\frac{\partial\zeta}{\partial t} = \frac{\partial\Phi}{\partial z} - \frac{\partial\Phi}{\partial x}\frac{\partial\zeta}{\partial x} \text{ at } z = \zeta, \tag{2.30}$$

where ζ is the free surface elevation. At any given point along the x-axis, the first term represents the rate of change in the height of the ocean's free surface. This rate must be equivalent to the sum of the terms on the right side of the equation: the first term on the right corresponds to the upward velocity of the water, while the second term represents the product of the water's horizontal velocity and the gradient of the surface. This relationship must hold exactly at the level of the ocean's free surface as it exists at that moment.

The dynamic boundary condition is related to the pressure at the free surface. The pressure on the free surface must equal the atmospheric pressure (assumed to be zero for simplicity) plus the dynamic pressure due to the fluid motion. Bernoulli's equation provides this dynamic boundary condition, ensuring that the pressure remains consistent across the interface. The condition can be expressed as:

$$\frac{\partial \Phi}{\partial t} + \frac{1}{2}(\nabla \Phi)^2 + g\zeta = 0 \text{ at } z = \zeta, \tag{2.31}$$

where g is the acceleration due to gravity. This equation states that the sum of the unsteady potential term, the kinetic energy per unit mass, and the potential energy per unit mass must remain constant along the free surface.

Linear wave theory is based on solutions to the Laplace equation, leading to the derivation of the wave dispersion relation. This relates the frequency $\omega_{(wave)}$ to the wavelength λ under the assumption that the depth of the water is greater than half the wavelength [34].

Figure 2.5 describes a regular sine wave that progresses in the positive direction x, where η represents the vertical displacement of the water surface from its normal undisturbed level, A_{wave} is the amplitude of the wave and can be described as $A_{wave} = 2a$, where a is the height of the wave. k is the wave number, related to λ as $k = \frac{2\pi}{\lambda}$, and measures how many cycles of the wave occur per unit distance. x is the spatial coordinate along which the wave propagates and t is the temporal dimension over which the wave is analysed. The angular frequency of the wave is related to the frequency f by $\omega_{wave} = 2\pi f$ and measures how many cycles occur over time:

$$\eta = \frac{H}{2}\cos(kx - \omega_{wave}t) \tag{2.32}$$

For a linear wave, k and ω_{wave} are connected by a dispersion relation given by:

$$\omega_{wave}^2 = gk\tanh(hk), \tag{2.33}$$

where h is the sea depth [35].

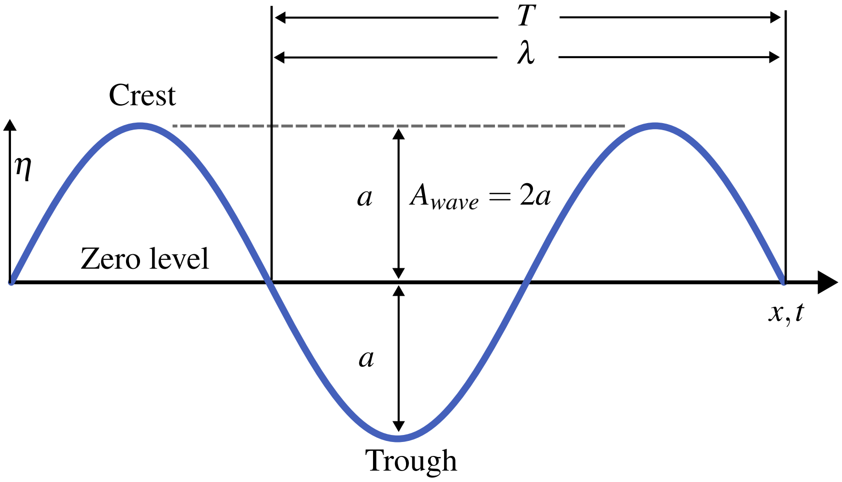

Figure 2.5: Schematic of a simple sine wave.

As the reader should note, the linear wave theory description included in this thesis is significantly shorter than the aerodynamic subsection. The reason behind this imbalance is because the main goal of this thesis is not to solve for the sea wave equations but to generate prescribed wave patterns based on well-known solutions from the linear wave theory. Such wave patterns, understood here as boundary surfaces for UVLM-based solvers, may affect the shape of the wakes being shed from the blades, through the so-called *blocking effect* in aeronautics, and in turn the power output. My intention is to investigate this phenomenon and its relevance to offshore wind turbines.

Chapter 3

Geometric Modelling and Kinematics

In this chapter, the geometric properties of the FOWT are described. This chapter aims to explain my contribution to the `UVLMeshGem`, which is the addition of a spar-type floating substructure and wave generation, as well as the movement of the structure and the waves. First, a general description of a FOWT is provided, then a detailed explanation of the geometric modelling of the substructure, and lastly a description of the movement of the FOWT. This section also includes a description of the wave model and kinematics.

3.1 Wind turbine description

A wind turbine consists of five different components; blade, hub, nacelle, tower, and substructure as seen in Figure 3.1 and as described below:

- Blade - Captures the energy of the wind.
- Hub -The central part of the machine to which the blades are attached. It enables the rotation of the blades and transmits the rotational movement to the gearbox or directly to the generator in the case of gearless designs.
- Nacelle - Where the gearbox, the generator, controller, yaw system, cooling and heating systems as well as anemometer and wind vane are placed.
- Tower - Supports the nacelle, hub, and blades. It elevates the structure.
- Subtructure - For offshore turbines, a monopile or a jacket is connected to the sea bed and supports the rest of the turbine. In the case of FOWT, a structure such as a spar keeps the turbine floating.

The blades, hub, nacelle and tower are already modelled in the `UVLMeshGen`, whilst the substructure is developed in this work and will be explained in detail.

3.2 Geometric modelling

This section describes the geometric modelling of the spar substructure using a geometric object 2 (GO_2) based on [19]. The modelling of the sea is described and a new geometric object 3 (GO_3) is introduced. This chapter also includes descriptions of the modifications available in `UVLMeshGen` as well as user functions.

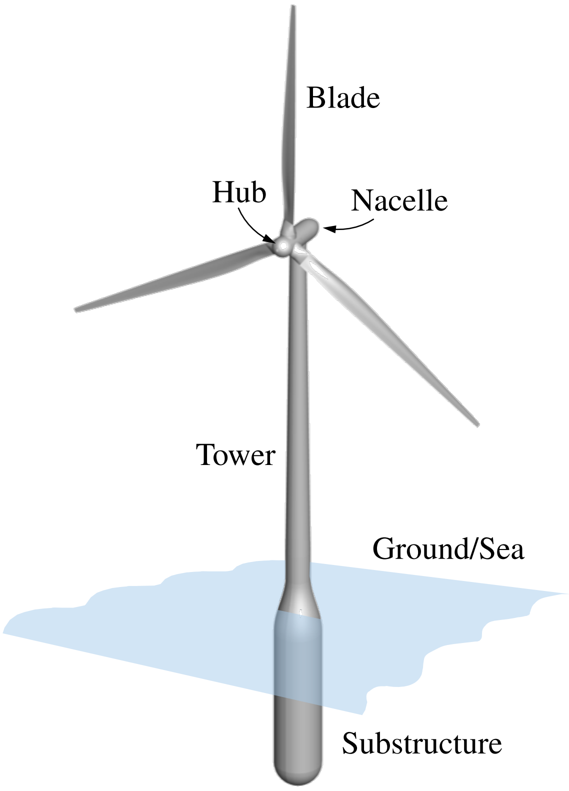

Figure 3.1: Wind turbine schematic.

3.2.1 Geometric objects GO_1 and GO_2

Two different geometric entities are defined in [19]; geometric object 1 (GO_1) and (GO_2).

GO_1 is a geometric object comprising a rectangular plate with a circular or ellipsoidal hole. The object is meshed using Fernandez-Guasti-squircular (FG-squircular) mapping, which refers to an intermediate shape between a square and a circle. This enables the transformation of a circular domain into a square region, mathematically represented as: $D = \left\{(u,v) \in \mathbb{R}^2 \mid u^2+v^2 \leq r^2\right\}$ into a square region parameterized as $S = \left\{(x,y) \in \mathbb{R}^2 \mid x^2+y^2-x^2y^2 \leq r^2\right\}$

Here, D represents the circular domain and S represents the transformed square region. The mapping facilitates a seamless transition from the circular domain D to the square domain S, characterised by sets of concentric circles and corresponding FG-squircles, respectively [36].

GO_2 is utilised for surface generation in computer-aided design, mainly through ruled skinning, a variant of lofting and skinning processes. The process of ruled skinning is defined as the creation of a surface by connecting a series of profile sections with ruled surfaces. A ruled surface in this context is mathematically defined as:

$$R(u,v) = C_1(u) + vr(u), \qquad \mathbb{R} \ni v = (1-v)C_1(u) + vC_2(u), \tag{3.1}$$

where $\mathbf{C}_k : \mathbb{R} \to \mathbb{R}^3$ is a parameterisation for the curve $C_k \subset \mathbb{R}^3$. Each point on the ruled surface is intersected by at least one line from this family, forming a continuous smooth surface. This method is integral to creating intricate surfaces with high precision in geometric modelling. The reader is referred to [19]for a detailed description of the geometric entities GO_1 and GO_2. In this work, GO_2 is used in order to build the spar substructure.

3.2.2 Geometric object GO_3

A new entity GO_3 is defined as a rectangular plane. Mathematically, object GO_3 is represented by a domain R in the Cartesian coordinate system $\mathbb{R}^2$, defined as $R = \left\{(x,y) \in \mathbb{R}^2 \mid 0 \leq x \leq L, 0 \leq y \leq W\right\}$, where L and W denote the maximum length and width of the rectangle, respectively. This entity is used to model the wave. A visualisation of the geometric entities can be seen in Figure 3.2.

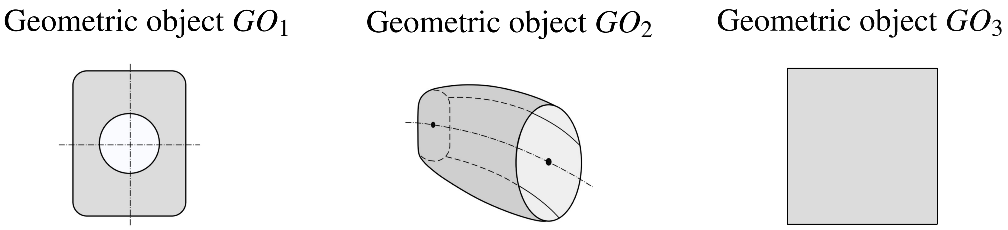
Geometric object GO_1 Geometric object GO_2 Geometric object GO_3

Hole plate Skinned surface Flat surface

Figure 3.2: Geometric entities

3.2.3 Discretisation

The discretisations of GO_1, GO_2, and GO_3 are achieved by a structured grid approach. The rectangle is subdivided into a finite array of QEs, ensuring coverage of the surface. For further aerodynamic analysis, this discretisation provides an accurate representation of the rectangular domain. Each quadrilateral element within this grid is defined by its vertices in the Cartesian plane.

Its coordinates are determined by the subdivisions along the length and width of the rectangle. GO_2 is used to model the substructure in this work, and GO_3 is used to model the wave boundary layer.

3.3 Substructure modelling

The mesh of the substructure is generated as the union of four meshes, from bottom to top; *1)* a hemisphere, *2)* a cylinder, *3)* a cubic parabola and *4)* another cylinder. These are all ruled surfaces and are therefore generated by GO_2 entities. This section provides detailed descriptions of each component. An exploded view of the substructure can be seen in Figure 3.3. Table 3.1 provides a summary of the variables associated with the components.

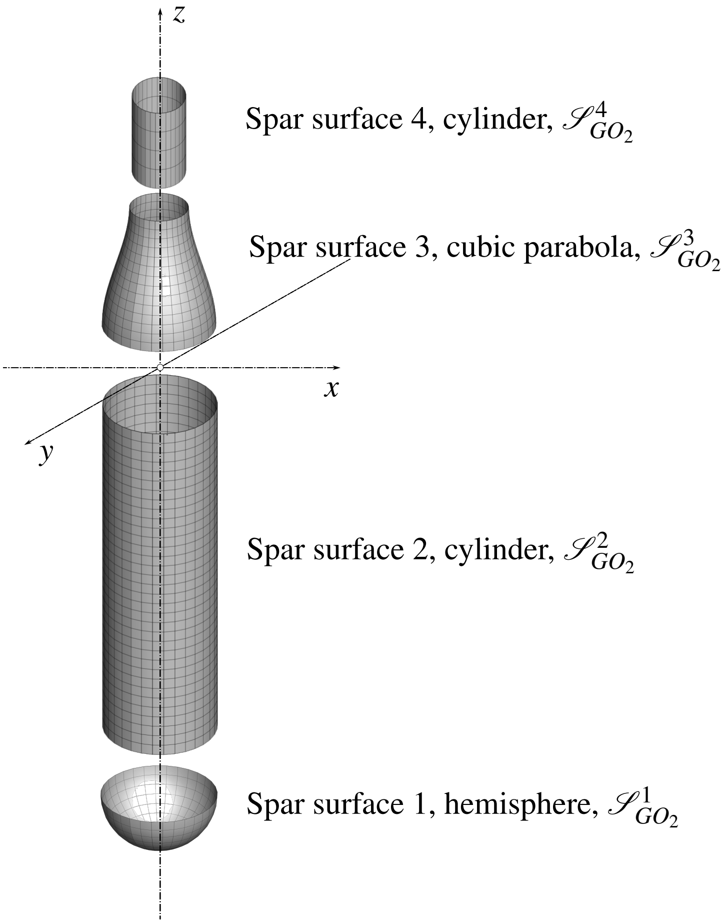

Figure 3.3: Exploded view of the spar substructure.

3.3.1 The hemisphere

The bottom of the substructure is a hemispheric shape, cut along the equatorial plane, $\frac{\pi}{2} \leq \phi \leq \pi$. The Cartesian coordinates can be calculated from the spherical coordinates as follows:

$$\begin{aligned} x &= \upsilon \sin\phi_s \cos\theta_s, \\ y &= \upsilon \sin\phi_s \sin\theta_s, \\ z &= \upsilon \cos\phi_s \end{aligned} \tag{3.2}$$

where υ is a coordinate along the radial direction. In restricting ϕ_s, the same equations can be used to calculate the coordinates of a hemisphere. The angular coordinate, θ_s, is a measure of the angle around the cylindrical axis, varies between 0 and 2π radians, and is linearly distributed over this range. The subscript s is introduced to denote relation to the substructure.

3.3.2 The cylinder

The radial distance, indicated as r, is the radius of the base of the cylinder and is a constant value for the cylindrical surface. The height, denoted z, is the vertical distance along the cylinder axis, linearly spaced from 0 to the total length of the cylindrical part of the spar. The transformation of these cylindrical coordinates to Cartesian coordinates (x, y, z) follows:

$$\begin{aligned} x &= r \cdot \cos\theta_s, \\ y &= r \cdot \sin\theta_s, \\ z &= z \end{aligned}$$

3.3.3 The cubic parabola

The geometry of the top of the substructure is a cubic parabola. In general, a cubic parabola is defined by the function

$$f(x) = ax^3 + bx^2 + cx + d, \tag{3.3}$$

where a, b, c and d are constant and $a \neq 0$ to ensure the function is cubic and x is the variable. This geometry is utilised in the substructure to allow for a varying radius along the vertical length of the parabola.

3.3.4 Spar substructure assembling

Variables in the structure can be changed by modifying the `DataSheet.DAT` file referenced in the WT configuration file. It is stressed that the `DataSheet.DAT` file should correspond to the turbine that the user is investigating. The WT parameters are well accounted for in [19]. The substructure parameters are seen in Table 3.1. It is possible to change the number of nodes along the vertical axis, defining a finer or coarser grid. Changing the number of nodes along the circumferential direction for the individual geometries is possible but not recommended. The user is recommended to change the number of nodes along the circumferential direction only for the entire structure.

Table 3.1: Substructure static variables

Variable	**Structure field name**	**Description**
*	`RTopSpar`	Radius of the coupling connection between the tower and the spar (It has to be equal to the radius of the tower at ground level)
*	`RBottomSpar`	Radius of the floating spar at the bottom
*	`LTotSpar`	Length of the floating spar
*	`LCylSpar`	Length of the cylindrical part of the floating spar
*	`LTopSpar`	Length of the upper part of the floating spar
*	`NcircSpar`	Number of nodes along the circumferential direction on the spar
*	`ZBottomSpar`	Number of nodes along the longitudinal direction (z-axis) of the spar
*	`ZCylSpar`	Number of nodes along the longitudinal direction (z-axis) of the spar
*	`ZTranSpar`	Number of nodes along the longitudinal direction (z-axis) of the spar
*	`ZTopSpar`	Number of nodes along the longitudinal direction (z-axis) of the spar

The spar substructure is modelled and implemented in the `UVLMeshGen`, completing the structure of the FOWT. Further, a wave boundary layer can be modelled as an addition to the FOWT simulation framework.

3.4 Wave Modelling

In addition to the substructure consisting of entities GO_2, the wave is also modelled in the programme. The wave consists of a GO_3 entity and its discretisation can be seen in Figure 3.4. The reader should note that this figure is puerly for visualisation purposes and does not actually represent any specific simulation conducted in this work. This is an example wave where there is only one wave coming from a direction of 0°, the wavenumber $k = 0.1$ and th amplitude of the wave $A_{wave} = 5$m. It is adjusted by the wave function and dispersion relation to fit typical wave patterns. Table 3.2 presents the variables related to wave modelling. This function is allocated within the `Sea Files` folder and is a user function so that the user can engineer the wished wave. Furthermore, within the main script called `MainProgram`, the `SeaSize` can be modified on the x and y-axis. To include the sea configuration in the simulation, the variables within `Sea_FLAG` should be adjusted accordingly as described in Table 3.3. It is important to note that the wave modeling does not involve creating a physical hole for the WT. The model represents the waves and their interactions with the floating wind turbine structure without any modifications to the wave surface for the FOWT's placement.

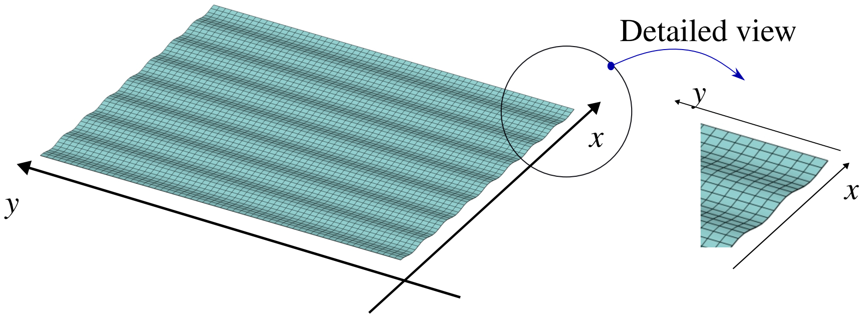

Figure 3.4: Example of a discretised wave using GO_3 elements.

Table 3.2: Wave model static variables

Variable	**Structure field name**	**Description**
*	`NumberWaves`	The number of waves simulated
*	`g`	Acceleration due to gravity, 9.81 m/s^2
*	`h`	Depth of the water in which the wave is propagating (m)
*	`K`	Wave number (rad/m)
*	`Amp`	Amplitude of the wave (m)
*	`Theta`	Phase angle of the wave (rad)

Table 3.3: `Sea_FLAG` configuration

Variable	**Structure field name**	**Description**
*	`ON/OFF`	Sea ON or Sea OFF
*	`userfunction`	Referring to the corresponding kinematics file, defining the kinematics of the sea surface
*	`x`	Discretization of the sea along the x-direction
*	`y`	Discretization of the sea along the y-direction

The user can modify the wave to the desired user function, making the simulation framework versatile.

3.5 Kinematics of the wind turbine

This section explains the theory of kinematics related to the FOWT and the wave. First, a description of the characteristic motions in relation to a FOWT, then a detailed description of the translation and rotation of the substructure. Further, the kinematics of the waves are also accounted for. A description of the kinematic variables in `UVLMeshGen` is provided.

3.5.1 Rigid body motion

The motion of a rigid body (here a FOWT) in a three-dimensional space can be described in terms of six characteristic motions. This can be further described as translational movements or rotational movements. The translational movements define the movements along the x, y and z -axis called *Surge*, *Sway*, and $Heave$, respectively. The rotational movements describe the rotations around the x, y and z -axis, namely $Roll$, $Pitch$, and *Yaw*, respectively. Roll and pitch are tilting motions along the respective axis. Yaw is a turning movement about the vertical axis. A visual description of the motions can be found in Figure 3.5.

3.5.2 Translation of the structure

The translational movements of the structure are crucial to describe the movements in a three-dimensional space. The surge refers to the forward and backward movement of the FOWT along the x-axis. The Sway is the movement from side to side following the y -axis. In offshore environments where asymmetric wind forces or wave action can affect the structure, this lateral translation is critical. The heave represents the vertical movements of the turbine along the z-axis, which is particularly significant due to the influence of waves and tides.

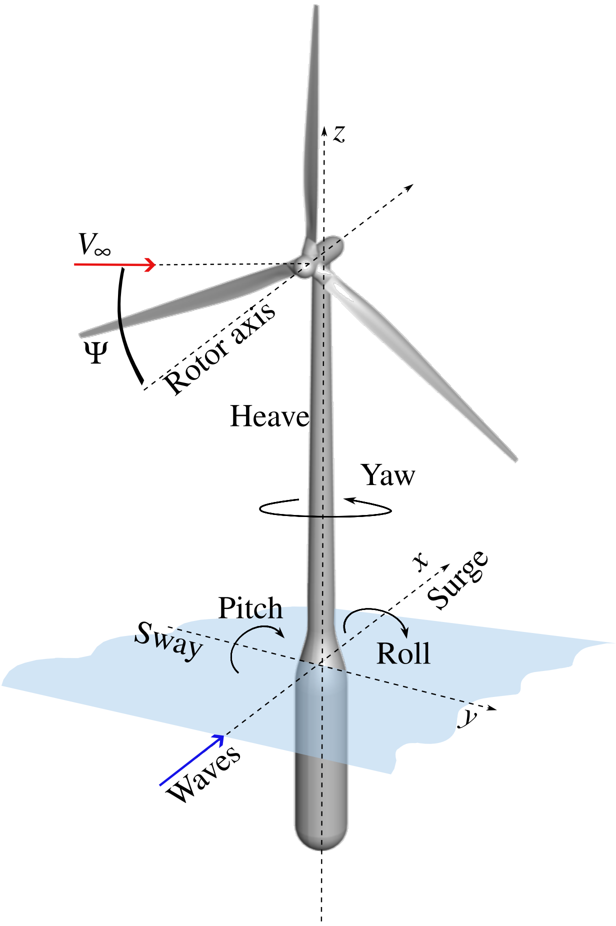

Figure 3.5: Characteristic motions of a FOWT.

3.5.3 Rotation of the substructure

In designing and implementing our rotational transformations, we adhere to the principles outlined in Rodrigues' Rotation Formula. This formula is a cornerstone of three-dimensional rotations. It provides a robust and efficient method for rotating a vector in a three-dimensional space around a given axis by a given angle. Rodrigues' Rotation Formula is given by:

$$\mathbf{v}_s = \mathbf{v}\cos\theta_s + (\mathbf{k}\times\mathbf{v})\sin\theta_s + \mathbf{k}(\mathbf{k}\cdot\mathbf{v})(1-\cos\theta_s), \tag{3.4}$$

where $\mathbf{v}_s$ is the rotated vector, $\mathbf{v}$ is the original vector, θ_s is the angle of rotation and $\mathbf{k}$ is the unit vector along the axis of rotation

The rotation of a rigid body in the space can be described by using different set of parameters, such as Euler angles or Euler parameters, among others. To describe the rotation of the substructure of the wind turbine, I consider a parameterisation based on Euler angles, specifically a 3-2-1 sequence. Such a sequence is given by a 3-rotation by α_s (substructure yawing), followed by a 2-rotation through β_s (substructure pitching) and 1-rotation through γ_s (substructure rolling). Figure 3.6 shows a schematic of the rotation sequence. The sequence 3-2-1 represents the rotation between the inertial frame N and a reference frame B fixed to the substructure. In addition, I introduce two auxiliary reference frames named A and A', which are necessary to fully describe each one of the rotations in the mentioned sequence.

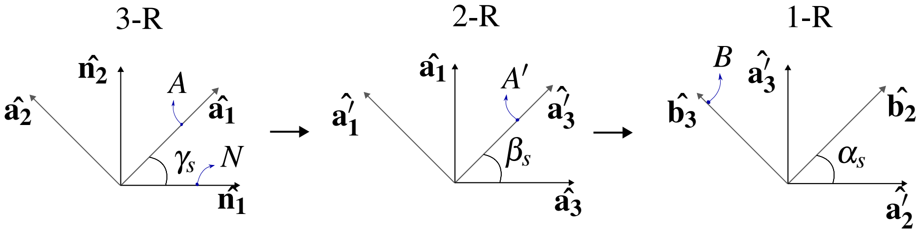

Figure 3.6: Schematic for a 3-2-1 rotation sequence using Euler angles.

Each one of these rotations are given by the following orthogonal matrices:

$$\mathbf{T}_{AN} = \begin{bmatrix} \cos\gamma_s & \sin\gamma_s & 0 \\ -\sin\gamma_s & \cos\gamma_s & 0 \\ 0 & 0 & 1 \end{bmatrix} \quad \mathbf{T}_{A'A} = \begin{bmatrix} \cos\beta_s & 0 & -\sin\beta_s \\ 0 & 1 & 0 \\ \sin\beta & 0 & \cos\beta_s \end{bmatrix} \quad \text{and}$$
$$\mathbf{T}_{BA'} = \begin{bmatrix} 1 & 0 & 0 \\ 0 & \cos\alpha_s & \sin\alpha_s \\ 0 & -\sin\alpha_s & \cos\alpha_s \end{bmatrix}, \tag{3.5}$$

where $\mathbf{T}_{AN} : N \longrightarrow A$ is the rotation matrix between the inertial frame N and the auxiliary reference frame A, $\mathbf{T}_{A'A} : A \longrightarrow A'$ is the rotation matrix between the auxiliary reference frame A and the auxiliary reference frame A', and $\mathbf{T}_{BA'} : A' \longrightarrow B$ is the rotation matrix between the auxiliary frame A' and the body-fixed frame B (the one attached to the substructure).

The transformation map between the inertial frame N and the body-fixed frame B, $\mathbf{T}_{BN} : N \longrightarrow B$, can be mathematically represented by the following matrix product,

$$\mathbf{T}_{BN} = \mathbf{T}_{BA'}\mathbf{T}_{A'B}\mathbf{T}_{AN}, \tag{3.6}$$

which after some algebraic manipulations takes the following form,

$$\mathbf{T}_{BN} = \begin{bmatrix} \mathbf{c}\beta_s\mathbf{c}\gamma_s & \mathbf{s}\gamma_s\mathbf{c}\beta_s & -\mathbf{s}\beta_s \\ \mathbf{s}\alpha_s\mathbf{s}\beta_s\mathbf{c}\gamma_s - \mathbf{s}\gamma_s\mathbf{c}\alpha_s & \mathbf{s}\alpha_s\mathbf{s}\beta_s\mathbf{s}\gamma_s + \mathbf{c}\alpha_s\mathbf{c}\gamma_s & \mathbf{s}\alpha_s\mathbf{c}\beta_s \\ \mathbf{s}\alpha_s\mathbf{s}\gamma_s + \mathbf{s}\beta_s\mathbf{c}\alpha_s\mathbf{c}\gamma_s & -\mathbf{s}\alpha_s\mathbf{c}\gamma_s + \mathbf{s}\beta_s\mathbf{s}\gamma_s\mathbf{c}\alpha_s & \mathbf{c}\alpha_s\mathbf{c}\beta_s \end{bmatrix}, \tag{3.7}$$

where the abbreviations $\sin = \mathbf{s}$ and $\cos = \mathbf{c}$ were used to keep the expressions as short as possible. The inverse transformation, $\mathbf{T}_{NB} : B \longrightarrow N$, is obtained simply by taking the transpose of $\mathbf{T}_{BN}$, that is, $\mathbf{T}_{NB} = \mathbf{T}_{BN}^T$.

The kinematic description of the entire wind turbine is an essential part of this thesis, since positions and velocities are used by UVLM-based solvers. To this end, I describe here the position and velocity of an arbitrary material point P belonging to the blade (see Fig. 3.7). Positions and velocities for the rest of the wind turbine components can be derived by following a similar procedure. First, let the inertial frame N to have origin O and the reference frame B attached to the substructure to have origin O'. The reader should recall that the rotation transformation between the substructure and the inertial frame N was properly described above by following a 3-2-1 sequence (see Eq. (3.6)). Then, the position vector between points O and $O'$is written as $\mathbf{r}^{O'/O} = u_1\hat{\mathbf{n}}_1 + u_2\hat{\mathbf{n}}_2 + u_3\hat{\mathbf{n}}_3$, where u_1 is the surge displacement, u_2 is the sway displacement, u_3 is the heave displacement, and $\{\hat{\mathbf{n}}_1, \hat{\mathbf{n}}_2, \hat{\mathbf{n}}_3\}$ is a basis for the inertial frame N. By following a classical kinematic chain description, the position vector of a point P on the blade with respect to the origin of N is as follows,

$$\mathbf{r}^{P/O} = \mathbf{r}^{O'/O} + \mathbf{r}^{p^t/O'} + \mathbf{r}^{p^n/p^t} + \mathbf{r}^{p^h/p^n} + \mathbf{r}^{p^{hb}/p^h} + \mathbf{r}^{P/p^{hb}}, \tag{3.8}$$

where $\mathbf{r}^{p^t/O'}$ is the position vector of the point p^t located at the top of the tower and laying on its longitudinal axis with respect to O', $\mathbf{r}^{p^n/p^t}$ is the position vector of the point p^n located at intersection between the longitudinal axis of the tower and the shaft axis of the rotor with respect to p^t, $\mathbf{r}^{p^h/p^n}$ is the position vector of the point p^h located at the hub and laying on the shaft axis of the rotor with respect to p^n, $\mathbf{r}^{p^{hb}/p^h}$ is the position vector of the point p^{hb} located at the connection hub-blade with respect to p^h, and finally $\mathbf{r}^{P/p^{hb}}$ is the position vector of point P with respect to p^{hb}. A schematic of the kinematic chain descripion can be seen in Figure 3.7.

The velocity vector of P is obtained by taking the total derivative with respect to time of Eq. (3.8) and performed by an inertial observer, i.e.,

$$\begin{aligned} \mathbf{V}^P = & \frac{{}^N d}{dt}\mathbf{r}^{O'/O} + \frac{{}^N d}{dt}\mathbf{r}^{p^t/O'} + \frac{{}^N d}{dt}\mathbf{r}^{p^n/p^t} + \frac{{}^N d}{dt}\mathbf{r}^{p^h/p^n} + \\ & + \frac{{}^N d}{dt}\mathbf{r}^{p^{hb}/p^h} + \frac{{}^N d}{dt}\mathbf{r}^{p/p^{hb}}, \end{aligned} \tag{3.9}$$

where $\frac{^N d}{dt}\mathbf{r}^{O'/O}$ is the translational velocity of the substructure, which can be written as $\mathbf{V}_{sub} = \dot{u}_1\hat{\mathbf{n}}_1 + \dot{u}_2\hat{\mathbf{n}}_2 + \dot{u}_3\hat{\mathbf{n}}_3$. The dot over the variables $(\dot{\cdot})$ indicates the time derivative and is a standard notation in dynamic systems.

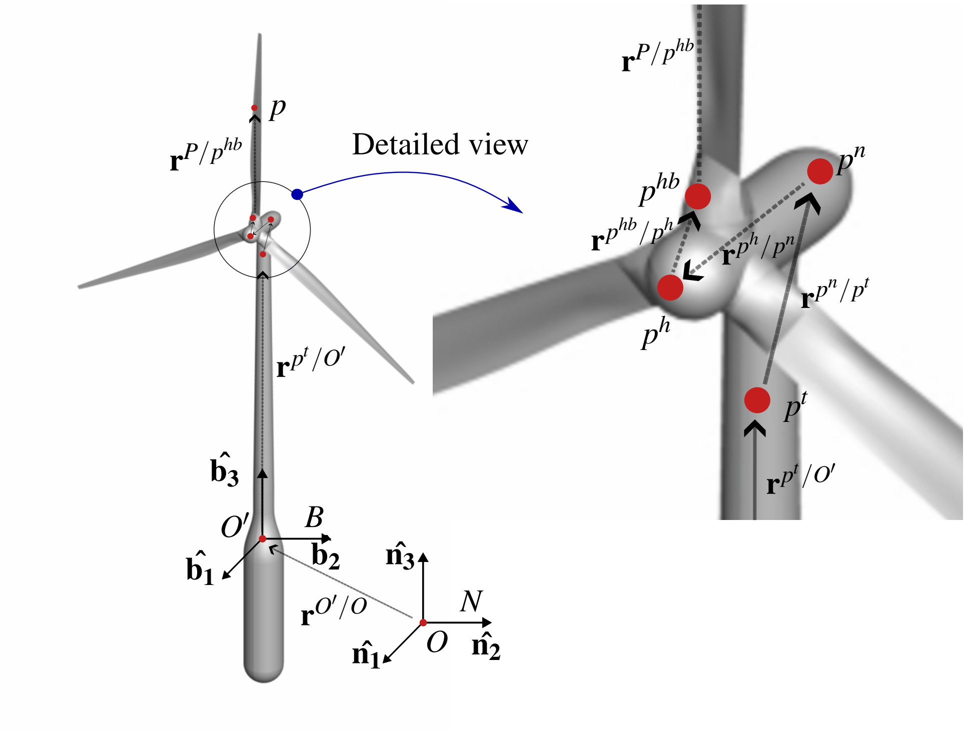

Figure 3.7: Description of the kinematic chain for a material point located in the blade.

Using some classical results from mechanics, Eq. (3.9) can be rewritten as:

$$
\begin{aligned}
\mathbf{V}^P = {} & \mathbf{V}_{sub} + \boldsymbol{\Omega}_{sub} \times \mathbf{r}^{p^t/O'} \\
& + (\boldsymbol{\Omega}_{sub} + \boldsymbol{\Omega}_{nacelle}) \times \mathbf{r}^{p^n/p^t} \\
& + (\boldsymbol{\Omega}_{sub} + \boldsymbol{\Omega}_{nacelle} + \boldsymbol{\Omega}_{hub}) \times \mathbf{r}^{p^h/p^n} \\
& + (\boldsymbol{\Omega}_{sub} + \boldsymbol{\Omega}_{nacelle} + \boldsymbol{\Omega}_{hub} + \bar{\boldsymbol{\Omega}}_{hub}) \times \mathbf{r}^{p^{hb}/p^h} \\
& + (\boldsymbol{\Omega}_{sub} + \boldsymbol{\Omega}_{nacelle} + \boldsymbol{\Omega}_{hub} + \boldsymbol{\Omega}_{blade}) \times \mathbf{r}^{P/hb},
\end{aligned}
\tag{3.10}
$$

where $\boldsymbol{\Omega}_{sub}$ is the angular velocity vector of the substructure, $\boldsymbol{\Omega}_{nacelle}$ is the angular velocity vector of the nacelle with respect to the tower and accounts for the nacelle yaw motion, $\boldsymbol{\Omega}_{hub}$ is the angular velocity vector of the hub with respect to the nacelle and accounts for the rotation of the hub, $\boldsymbol{\Omega}_{blade}$ is the angular velocity vector of the blade with respect to the hub and accounts for the blade pitch motion (if any), and × is the well-known cross product.

The user can generate different kinematic scenarios by turning on and off the `Kinematic_FLAG`. When the kinematics is turned on, the parameters shown in Table 3.4 can be individually turned on and off to study each movement's impact. Within each kinematic file, the amplitude and angular frequency can be altered.

Table 3.4: Kinematic variables

Variable	**Structure field name**	**Description**
*	`Rotor`	Rotor kinematics, turbine (ON / OFF)
*	`Yaw`	Yaw motion, turbine (ON / OFF)
*	`Pitch`	Pitch motion, turbine (ON / OFF)
*	`Heave`	Heave motion, substructure (ON / OFF)
*	`Surge`	Surge motion, substructure (ON / OFF)
*	`Sway`	Sway motion, substructure (ON / OFF)
*	`SubRoll`	Roll motion, substructure (ON / OFF)
*	`SubPitch`	Pitch motion, substructure (ON / OFF)
*	`SubYaw`	Yaw motion, substructure (ON / OFF)

The user is able to generate many different simulation scenarios by using the theory of this section.

3.6 Wave kinematics

In this work, the waves are based on sinusoidal functions that describe sine and cosine waves. It should be stressed that I am not solving the wave equations and that the purpose of the wave boundary layer is to investigate the effect of its presence on the power output of the FOWT. The imposed motions, coming from the linear wave theory, of sine-waves and cosine-waves can be described as:

$$y(x,t) = A_{wave}\sin(kx - \omega t + \phi_{wave}), \tag{3.11}$$

$$y(x,t) = A_{wave}\cos(kx - \omega t + \phi_{wave}), \tag{3.12}$$

respectively, where $y(x,t)$ is the displacement at position x and time t, and ϕ_{wave} is the phase angle which determines the wave's phase speed at $t = 0$. To allow for combinations of waves coming from different directions and include temporal change, the above equations are modified into the following equation:

$$z(x,y,t) = A\cos(kx\cos(\theta_{wave}) + ky\sin(\theta_{wave}) - \omega_{wave}t) + z_{offset}, \tag{3.13}$$

where $z_{offsett}$ is an additional parameter to adjust the initial position along the z-axis in the wave simulation. Further, the effects of the waves using the principle of superposition is given by:

$$\begin{aligned} z_{\text{superposed}}(x,y,t) = \sum_{i=1}^{n} A_i \cos\big(& k_f x \cos(\theta_{\text{wave},i}) \\ &+ k_f y \sin(\theta_{\text{wave},i}) - \omega_{\text{wave},i} t\big) + z_{\text{offset}}, \end{aligned} \tag{3.14}$$

where n is the number of waves being considered and A_i, $\theta_{\text{wave},i}$, and $\omega_{\text{wave},i}$ are the amplitude, direction, and angular frequency of the i-th wave, respectively.

The wave kinematics can be turned on or off in a similar way as the kinematics of the substructure. First, the size of the sea can be determined by the variable `SeaSize`, which gives the option to determine a start and end value in both x-and y-direction for the two-dimensional sea mesh. Further, the `Sea_FLAG` must be turned on and the `Ground_FLAG` must be turned off to investigate the sea. Within the `Sea_FLAG` variable, a user function must be provided that defines the kinematics of the sea surface. Within this function, all parameters described in the above equations should be accounted for as seen in Table 3.2. Figure 3.8 shows the capability of the `UVLMeshGen` to create more complex waves. *Example wave 1* was generated assuming three different waves coming from directions 0°, 45°and 115°. The wavenumber k = 0.1 for all three profiles, and the amplitudes are 5m, 7m and 8m, respectively. *Example wave 2* was generated assuming four different waves coming from directions 0°, 90°, 115°and 162°. The parameter k is 0.1 for the first three profiles and 0.15 for the last one, and the amplitudes are 5m, 7m, 8m and 13 m, respectively. These wave profiles serves as visual examples of the capability of the `UVLMeshGen` and are not actual simulation cases that will be analysed in this work.

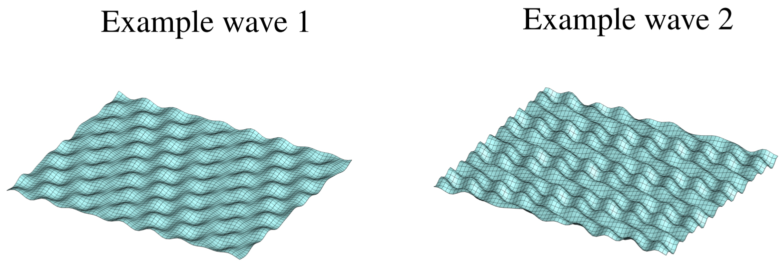
Example wave 1

Example wave 2

Figure 3.8: Example of waves

The wave boundary layer can be added to the movements imposed on the FOWT, effectively creating a large number of simulation options.

Chapter 4

Results and Discussion

In this chapter, the numerical results are presented and discussed. In this work, three different turbines are used; the DTU 10MW RWT, the Sandia 13.2 MW, and the NREL 5 MW reference turbine [37], [38], [39]. First, a verification of the entire simulation framework consisting of the `UVLMeshGen` and `VLMSim` flow solver is conducted. I aim to investigate if the power production of the NREL 5 MW turbine changes when the motions of heave, surge and pitch are imposed on the substructure. Therefore, the motions are individually simulated to investigate the influences of each kinematic. Then, I consider different combinations of such motions giving raise to several simulation scenarios. It should be noted that all the motion patterns considered here are inspired by the work presented in [10]. Secondly, the addition of a sea wave, as a boundary surface, to a stand-still turbine is investigated. Third, a full FOWT without any motion on its substructure but considering different sea configurations is investigated. Lastly, as simple showcases to exhibit the capabilities of the simulation framework, two different offshore wind farm layouts are studied.

A full overview of the simulation scenarios can be seen in Table 4.1. There are five main simulation parts: 1) isolated motions, 2) combined motions, 3) wave effect on the output power, 4) full FOWT simulations, and 5) multiple FOWTs. Part 1) consists of *Sim. A*, *Sim. B* and *Sim. C* and are scenarios in which the isolated motions of heave, surge and pitch are simulated individually, respectively. Part 2) consists of scenarios from *Sim. D* to *Sim. H*. Specifically, *Sim. D* and *Sim. E* combine heave and surge, where the former simulation considers a circular pattern motion for the substructure (wind and wave aligned) and the latter considers also a circular pattern motion for the substructure, but the wind and wave are 180 out of phase (not aligned). Further *Sim. F* combines heave and pitch, *Sim. G* combines surge and pitch, and lastly *Sim. H* combines all three motions. In Part 3), consisting of *Sim. I*, investigates the effect of imposing a sea wave surface which propagates with a prescribed kinematics on the power output of a FOWT. Then, in Part 4), consisting of *Sim. J*, considers a FOWT with all the components activated (hub, blades, nacelle, tower and substructure). This case considers: a full FOWT without movement and without a wave, a full FOWT without movement but with the presence of a wave and lastly, a full FOWT with heave motion and the presence of a wave. Finally, Part 5) presents two cases concerning multiple FOWTs within two different offshore wind farm layouts (*Sim. K*).

Table 4.1: Simulation cases

Simulation name	**Description**
Sim. A	Isolated Heave
Sim. B	Isolated Surge
Sim. C	Isolated Pitch
Sim. D	Combined Heave & Surge, aligned
Sim. E	Combined Heave & Surge, unaligned
Sim. F	Combined Heave & Pitch
Sim. G	Combined Surge & Pitch
Sim. H	Combined Heave & Surge & Pitch
Sim. I	Wave Effect on the Output Power
Sim. J	Full FOWT simulations
Sim. K	Multiple FOWTs

4.1 Verification of Simulation Framework

To validate the implementation of the substructure to the simulation framework composed of `UVLMeshGen` and `VLMSim`, some simulations are performed for the three turbines: the DTU 10MW RWT, the Sandia 13.2 MW and the NREL 5 MW. It should be noted that both the DTU 10MW RWT and the Sandia 13.2 MW are based on an upscaling of the NREL 5MW. A detailed description of the upscaling can be found in [37] and [38] respectively. To best validate the new contributions that I made to the framework and produce reliable results, the NREL 5 MW is chosen as the main simulation turbine.

Due to the large number of simulations to be carried out, in this thesis I consider only the rotor blades (with exception of cases *Sim. J* and *Sim. K*) in order to reduce the computational cost of the aerodynamic simulations.

4.1.1 NREL 5 MW

The NREL 5MW turbine is a conceptual design that has become a standard for research and development of wind energy. This Reference Turbine is not a physical turbine, but rather a detailed model that provides a comprehensive set of specifications for simulations and analyses. The specifications of this turbine can be found in Table 4.2. By standardising many aspects of turbine modelling and simulation, the NREL 5 MW Reference Turbine has had a significant impact on wind energy research. It has facilitated numerous studies of turbine performance, grid integration, and wind farm optimisation through its comprehensive set of data and models and, therefore, serves as a common benchmark [40].

Table 4.2: NREL 5-MW Wind turbine properties

Parameter	Value
Rated Power	5 MW
Nr. of blades	3
Rotor, hub Diameter	126 m, 3m
Hub height	90 m
Cut-In Wind Speed	3 m/s
Rated Wind Speed	11.4 m/s
Cut-Out Wind Speed	25 m/s
Cut-In Rotor Speed	6.9 RPM
Rated Rotor Speed	12.1 RPM

Based on the work in [40], the standard test cases for the NREL 5 MW turbine are defined and simulated, as seen in Table 4.3. Here, the turbine is simulated at the rated rotor speed ($\Omega = 12.1$ RPM), uniform wind speeds and the corresponding blade-pitch angles.

Table 4.3: Standard test case for NREL 5 MW with blade pitch variation - Combined Results

Θ (deg)	V_∞ (m/s)	Power (kW)	Thrust (kN)
0.000	11.4 (rated)	3517.8	696.4
3.830	12.0	4376.3	528.6
6.600	13.0	4538.8	435.5
8.700	14.0	4466.1	376.6
10.450	15.0	4334.7	336.0
12.060	16.0	4127.8	301.8
13.540	17.0	3896.6	274.1
14.920	18.0	3656.4	251.4
16.230	19.0	3402.5	232.0
17.470	20.0	3156.9	215.9
18.700	21.0	2847.2	199.5

As seen in Table 4.3, the power is highest at a pitch angle of 6.600° at a value of 4538.8 kW and a thrust value of 435.5 kN. The power was expected to be the highest under the rated conditions of the turbines and would equal 5 MW.

However, it is clear that this is not the case. This suggests that there might be a difference in the values presented in the description of the NREL 5 MW turbine and the real simulation values [40]. The method used to calculate the power output presented in [40] is BEM which does not consider the full description of the geometry of the blade, while the UVLM method does consider a detailed description of the blade geometry which also explains the difference in power output seen here. It is my wish to conduct some experiments for the NREL 5 MW at the conditions that correspond to the maximum power output. Therefore, further investigations are conducted to tune the values to match the rated power. First, the rated condition of $V_\infty = 11.4$ m/s and $\Omega = 12.1$ RPM was fixed while the blade pitch angle changed as seen in Appenidx A. I found that the rated conditions described in the definition of the turbine do not correspond to a power output of 5 MW even when varying the blade pitch angle [40]. The highest power output is at a 3.0° blade pitch angle at approximately 4 MW as seen in Figure 4.1.

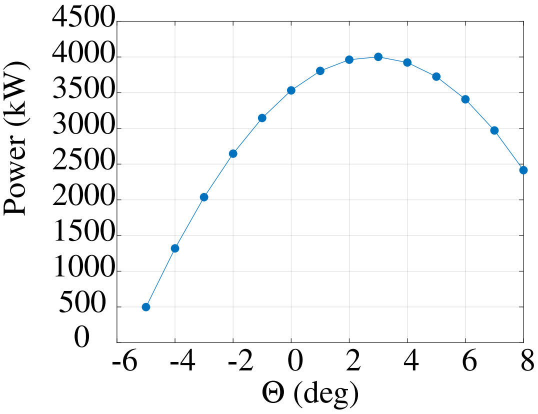

Figure 4.1: NREL 5MW Varying Pitch angle at standard conditions.

As the power did not reach 5 MW at any pitch angle for the fixed rated conditions, a new method was applied; interpolating the pitch angle and corresponding free stream velocity for the greatest value of power seen in Appendix A. The rotor speed remains the same at $\Omega = 12.1$ RPM. I found that the highest possible power production using this method with the available data is at a blade pitch angle of 5.5° and, correspondingly, $V_\infty = 12.6$ m/s. This gives a power output of 4549.2 kW. This was found at the turbine's standard configuration where the tilt has a value of 5 and a precone of 2.5. However, this work draws inspiration from the scenarios presented in [10]. Therefore, the tilt and the precone were set to 0 for the condition of $\Theta = 5.5°$ and $V_\infty = 12.6$ m/s, which gives a power value of 4634.2 kW and a thrust value of 483.7 kN. Moving forward, this work will use this case as a standard case to conduct experiments. This will be referred to as *The reference case* hereinafter and the power curves of the following simulations will include a dotted line to indicate this reference power. This work considers four different yaw angles (Ψ) for all simulation scenarios: Ψ = 0°, 15°, 30° and 45°. The yaw occurs when the rotor plane is not perpendicular to the wind direction, as seen in Figure 4.2. The standard reference power and thrust values when varying Ψ can be found in Table 4.4. the power decreases significantly when Ψ increases. The area exposed to V_∞ is reduced, causing the blade to experience a varying relative velocity and AoA. As a result, the energy conversion efficiency of the turbine is also reduced [41]. The effective wind speed V_{eff} should therefore be considered and is defined by:

$$V_{eff} = V_\infty \cos \gamma_{tilt} \cos \Psi, \tag{4.1}$$

where γ_{tilt} is the tilt angle. However, since this work considers $\gamma_{tilt} = 0$, V_{eff} can be described as $V_{eff} = V_\infty \cos \Psi$. Recalling Equation (2.1) for the power output of a wind turbine and including V_{eff}, the new power output considering the yaw angle can be defined as:

$$P = \frac{1}{2} \rho A V_{eff}^3 \cos^3(\Psi) C_P. \tag{4.2}$$

Table 4.4: NREL 5 MW reference cases with varying rotor yaw angle

Ψ (deg)	Power (kW)	Thrust (kN)
0	4634.2	483.7
15	4310.4	440.5
30	3364.8	325.51
45	1876.9	177.9

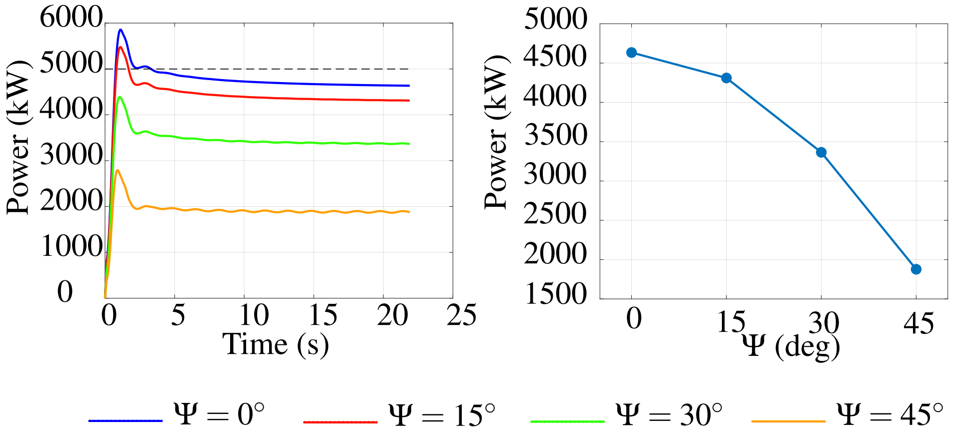

Figure 4.2: NREL 5MW Power curves, no movement, different Ψ.

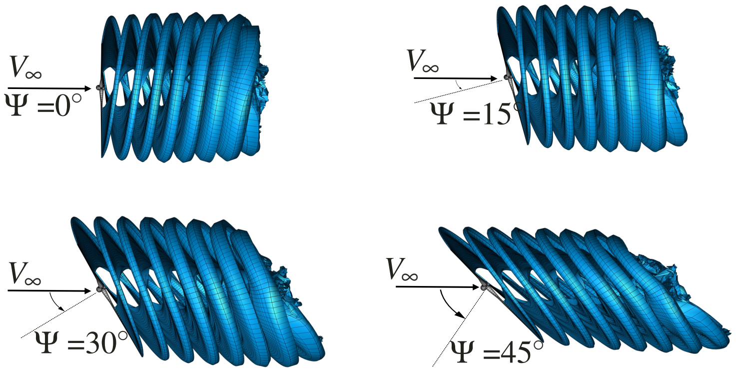

Figure 4.3: NREL 5MW Wake propagation, Standard condition with different Ψ.

The reference case serves as a good reference point for simulations. However, to further verify the abilities of the `UVLMeshGen`, and its new addition of a substructure, some further WTs are examined.

4.1.2 DTU 10 MW RWT

The DTU 10MW RWT is a conceptual model developed by the Technical University of Denmark (DTU) as part of an initiative to support next-generation large-scale wind turbines. The model is publicly available and serves as a high-fidelity design of an offshore wind turbine. As mentioned, the DTU 10 MW RWT turbine is an upscaling of the NREL 5 MW. For the detailes of this upscaling the reader is referred [42]. The relevant parameters for this turbine are found in Table 4.5 [37].

Table 4.5: DTU 10 MW Wind turbine properties

Parameter	Value
Rated Power	10 MW
Nr. of blades	3
Rotor, hub Diameter	178.3 m, 5.6 m
Hub height	119 m
Cut-In Wind Speed	4 m/s
Rated Wind Speed	11.4 m/s
Cut-Out Wind Speed	25 m/s
Minimum Rotor Speed	6.0 RPM
Maximum Rotor Speed	9.6 RPM

Multiple cases are simulated for the DTU 10 MW RWT where the pitch angle varies from 0.000° to 9.292° as seen in Table 4.6. I found that the power peaks at a $\Theta = 9.292°$, $V_\infty = 14$ m/s with a power of 10306.0 kW and a thrust value of 967.6 kN. The power curve of this case can be seen in Figure 4.4. This power output does not match the expected 10 MW. The parameters are taken from [42] and there might be a difference between the parameters stated in this report and the actual configuration. Similarly to the NREL 5 MW, the power of the DTU 10 MW RWT (presented in [42]) was calculated using BEM which again might also explain the difference in the power output.

Table 4.6: DTU 10 MW RWT simulation parameters

Θ (deg)	V_∞ (m/s)	Power (kW)	Thrust (kN)
0.000	8	1504.8	815.2
0.896	6	1233.3	512.8
2.751	4	773.9	242.7
4.502	12	7946.0	1277.6
7.266	13	9612.1	1086.7
9.292	14	10306.0	967.6

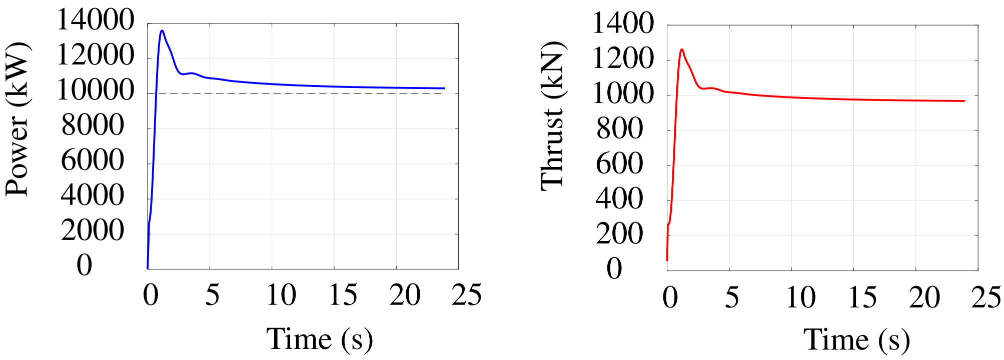

Figure 4.4: Power and thrust curves of DTU 10 MW RWT at $\Theta = 9.292°$ $V_\infty = 14$ m/s.

Even though the power output of the DTU 10 MW RWT did not exactly equal 10 MW, it provides a verification that the substructure can be implemented successfully. One final simulation is conducted to give the reader a full overview of the abilities of the `UVLMeshGen`.

4.1.3 Sandia 13.2 MW

The Sandia 13.2 MW is developed by Sandia National Laboratories and is also an upscaling of the NREL 5 MW. The properties of this turbine can be found in Table 4.7. Only one case is presented for this turbine; a standard case with no kinematic movement of the structure except from the blades. The case is simulated at rated conditions. Although it would be interesting to investigate this larger wind turbine further, the specific information needed to do so is limited to my knowledge. This case is meant to serve as a base for further research and as a verification of the simulation framework. Under rated conditions, the Sandia 13.2 MW was found to have a power output of 13200 kW, as seen in Figure 4.5, and a thrust of 1558.5 kN. This power output is the exact same as for the rated conditions and therefore this serves as a good verification.

Table 4.7: Sandia 13.2 MW Wind turbine properties

Parameter	Value
Rated Power	13.2 MW
Nr. of blades	3
Rotor, hub Diameter	205 m, 5.0 m
Hub height	146.4 m
Cut-In Wind Speed	3 m/s
Rated Wind Speed	11.3 m/s
Cut-Out Wind Speed	25 m/s
Minimum Rotor Speed***	6.0 RPM
Maximum Rotor Speed	7.44 RPM

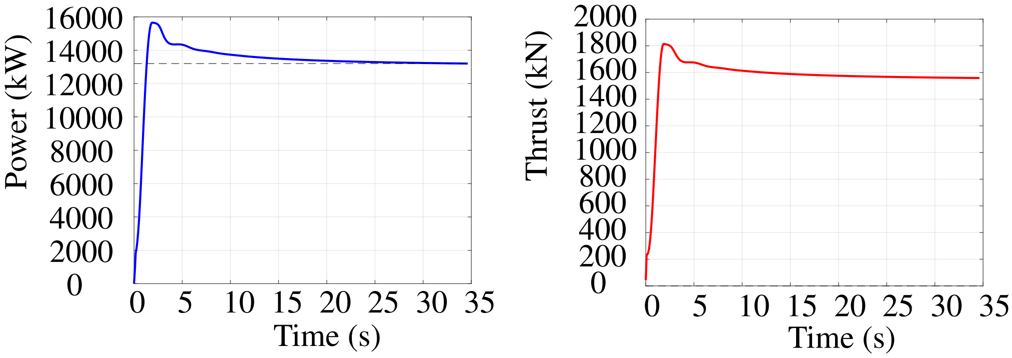

Figure 4.5: Power and Thrust curve for Sandia 13.2 MW.

While the Sandia 13.2 MW did produce the expected power output using the `UVLMeshGen` and `VLMSim`, the NREL 5 MW and DTU 10 MW RWT did not. As mentioned this might be due to differences in simulation data as well as that the previous simulations of these WTs do not consider geometry. Nonetheless, the objective of the verification is to show that the simulation framework is well-fitted for the implementation of a spar substructure. The verification of the actual simulation framework is already well established and the reader is referred to [19] and [14] for further details of this validation.

4.2 Aerodynamic Simulations Considering the Substructure motion

In this section, I study the aerodynamic behaviour and power output of FOWTs when considering imposed motion on the substructure. The motions of heave, surge, and pitch are investigated. For each motion, there are 12 simulation cases in which all cases have some common parameters, as seen in Table 4.8. The individual parameters of each motion can be found in Table 4.9. The individual motions of heave, surge, and pitch are also combined to define more complex simulation cases. The reader is referred to Table 4.1 for a description of the simulation cases. The simulation time was originally set to 400 timesteps, but for some simulations, this has been increased to 600. Ideally, the simulation time should be long for all cases. However, this has been reduced to allow the desired simulations to be performed within the given time frame for this work. It should be noted that to reduce computational costs, the simulations of the FOWT only consider the rotor, effectively neglecting the rest of the structure. However, the motion affects the rotor as if it had been imposed at the global reference point located in the substructure, which is presented in Chapter 3. Another thing to note is that I will especially focus on *Case 3* across the simulations. This is the case for which $\Psi = 0°$whilst $\hat{A}$ is at its peak. Generally, it is desired to have a small Ψ as discussed in 4.1.1. The turbine can, in real life, be adjusted to achieve a small Ψ, within limits. Since this work aims to investigate the influence of the different kinematics on the power output of the FOWT, the largest $\hat{A}$ has been chosen to display a more significant change. This is why *Case 3* is specifically considered. Further, the `VLMSim`- post processor which is used to analyse the results, is generally able to calculate the frequency of the signals of the power outputs. However, in some cases, the spectrum of the signal contains a mix of harmonics, and the post-processor overestimates the frequencies. The reader should therefore note that some frequencies are an estimate, as they have been calculated manually according to:

$$f = \frac{1}{T}, \tag{4.3}$$

where T is calculated as A_{x2}-A_{x1}, and where $x1$ and $x2$ are the amplitudes of the first two peaks in the signal.

Table 4.8: Common values for simulation cases

Parameter	Description	Value
β	Blade pitch angle	5.5°
Ω	Rotor speed	12.1 RPM
V_∞	Free stream velocity	12.6 m/s
ϕ	Phase	0 rad
T_w	Period	9 s
f	Frequency	0.11 Hz
Ψ	Rotor yaw angles	0°, 15°, 30°, 45°
H_w	Wave amplitudes	1 m, 3 m, 5 m

Table 4.9: Simulation parameters

Case nr.	Ψ (deg)	$\hat{A}_{\text{Heave}}$ (m)	$\hat{A}_{\text{Surge}}$ (m)	$\hat{A}_{\text{Pitch}}$ (deg)
1	0	1	0.20	0.60
2	0	3	0.61	1.70
3	0	5	1.01	2.80
4	15	1	0.20	0.60
5	15	3	0.61	1.70
6	15	5	1.01	2.80
7	30	1	0.20	0.60
8	30	3	0.61	1.70
9	30	5	1.01	2.80
10	45	1	0.20	0.60
11	45	3	0.61	1.70
12	45	5	1.01	2.80

4.2.1 Isolated motions

The isolated motions are investigated individually. This work is based on the parameters in [10], and so I have followed the same equation to model the surge and pitch motions:

$$X(t) = X_0 + \hat{A}\sin(2\pi f t + \phi_p), \tag{4.4}$$

where X is the surge/pitch displacement, X_0 is an offset displacement for the surge and pitch, $\hat{A}$ is the amplitude of the motion, f is the frequency of the motion, and ϕ_p is the phase angle of the motion which equals zero for the isolated motions. The heave equation follows a sinusodial variation with time as with surge and pitch and can be seen as:

$$Z(t) = Z_0 + \hat{A}\sin(2\pi f t), \tag{4.5}$$

where Z is heave displacement, and Z_0 is the heave offset. The frequency f is the same for all motions (0.11 Hz) and is taken from [10].

Isolated Heave

First, the heave is investigated as an isolated motion (*Sim A*). Three different amplitudes of the heave motion, $\hat{A}_{\text{heave}}$, were chosen; 1 m, 3 m and 5 m. This is based on the wave heights presented in [10]. I acknowledge that in a real-life situation, the amplitude of the heave will not be the same as the amplitude of the wave. However, the purpose of this simulation is to investigate the influence of different heave values on the power and thrust values. It is therefore assumed that $A_{wave} = \hat{A}_{\text{heave}}$ in this work.

Figure 4.6 shows the power and thrust curve evolving in time for *Case 3*. A dotted line is seen to indicate the power of *the reference case* for comparison. When stabilised, the power output is very close to that of *the reference case*, at a value of 4647.2 kW. For comparison, *the reference case* has a power output of 4634.2 kW at $\Psi = 0°$. The thrust of *Case 3* can also be compared similarly with *the reference case* with values of 484.7 kN and 483.7 kN, respectively. Table 4.10 shows the power related data for *Sim. A*, the rest of the simulation data can be found in Appendix C. The amplitude of the power is generally small. This could be because the relative airflow with respect to the movement of the structure does not change significantly because the heave motion is vertical and orthogonal with respect to V_∞. This leads V_{total} to remain unchanged, and so the AoA remains unchanged.

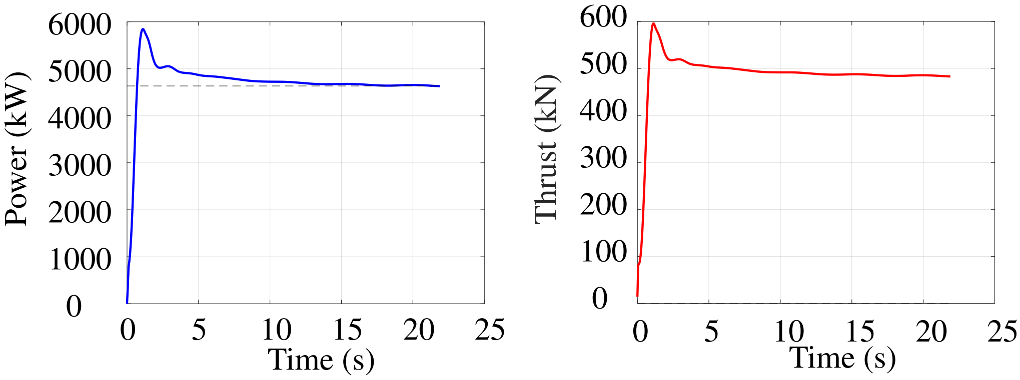

Figure 4.6: Power and thrust curve for isolated heave (*Sim. A*, *Case 3*).

Table 4.10: Power data of isolated heave simulations

Case nr.	Mean P (kW)	Freq P (Hz)	Amp. P (kW)	Max. P (kW)
1	4634.0	-	-	-
2	4645.4	0.06	0.2	4645.6
3	4647.2	0.215	6.0	4653.2
4	4314.7	6525	0.0	4314.7
5	4324.2	0.6299	1.4	4325.5
6	4326.8	0.2342	8.0	4334.8
7	3371.6	0.6299	6.2	3377.8
8	3375.7	0.7026	4.0	3379.8
9	3380.5	0.7942	1.4	3381.9
10	1886.0	0.6299	17.2	1903.2
11	1894.6	0.6198	14.4	1909.0
12	1903.0	0.567	10.5	1913.6

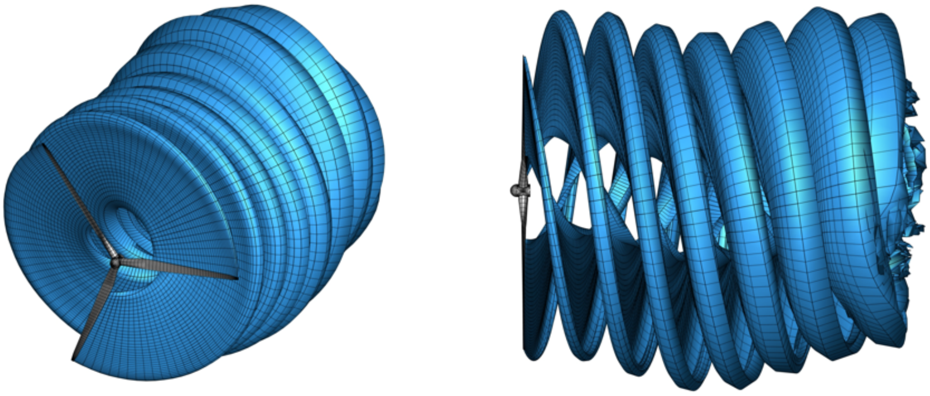

Figure 4.7: Wake profiles of *Sim. A*, *Case 3*, isolated view and side view of the wake propagation.

Figure 4.7 shows the wake profile of the isolated heave motion. First, an isolated view is shown where the turbine blades are clearly visible, and we see how the airflow changes further downstream. The second image is the side view of the same wake profile. Here, it is possible to analyse the oscillatory nature of the propagation. Although the oscillations in the power output are small, the heave motion does show a significant oscillatory impact on the FOWT’s wake profile. There are slight disturbances visible towards the end of the simulations, where the wake slowly starts to curve inward as seen in the isolated view.

These variations in the flow are called *starting vorticies*. According to the Kutta-Joukowski theorem described in section 2.2, the lift on an aerofoil is proportional to the circulation around it. As the blade starts to move, the starting vortex is created to satisfy the Kutta condition, which states that the flow must leave the trailing edge smoothly. In terms of frequency, it is not clear why the output does not approximate the frequency of the imposed motion of 0.11 Hz. The frequency spectrum might be affected by the wake somehow, but it is unclear if this phenomenon is a manifestation of the underlying physics behind this study or an artificial artefact. In order to fully understand why this happens, further investigations are required, which is beyond the scope of this thesis.

Isolated Surge

Surge is then investigated as an individual motion (*Sim B*). Originally, this was simulated at 400 time steps, but it was found that the power curve did not have time to stabilise. Therefore, a new simulation was conducted consisting of 600 time steps. The amplitude of the power is generally large, as can be seen in Figure 4.8 where the power oscillates significantly about the reference power of 4634.2 kW. The power of *Case 3* has an amplitude of 624.5 kW, which confirms the large oscillations seen in Figure 4.8. Table 4.11 shows the power data for the isolated surge motion. The rest of the simulation data can be found in Appendix D.

Table 4.11: Power data of isolated surge simulations

Case nr.	Mean P (kW)	Freq P (Hz)	Amp. P (kW)	Max. P (kW)
1	4620.5	0.1100	127.4	4747.9
2	4620.9	0.1107	378.8	4999.7
3	4622.2	0.1107	624.5	5246.7
4	4299.9	0.1121	121.4	4421.2
5	4300.6	0.1114	362.7	4663.3
6	4302.0	0.1107	598.0	4900.0
7	3264.1	0.1137	0.4	3264.5
8	3366.6	0.1142	317.3	3683.9
9	3367.8	0.1135	523.2	3891.0
10	1881.5	0.1137	1.4	1882.9
11	1885.7	0.1179	258.1	2143.8
12	1888.3	0.1156	417.1	2305.4

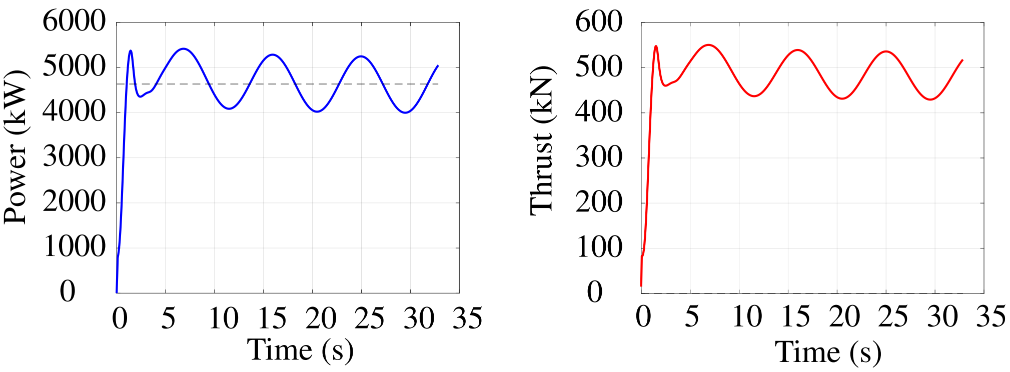

Figure 4.8: Power and thrust curve for isolated surge (*Sim. B*, *Case 3*).

I suggest that the reason for the significant oscillation of the surge power is that the AoA increases or decreases as the structure moves back and forth (with or against V_∞). Consider that V_∞ follows a positive x-axis and that the structure moves along this x-axis. The relative incoming wind velocity, V_{rel}, can be described as $V_{rel} = V_\infty - V_{Surge}$. When the structure follows a negative x-axis, V_{Surge} taking on a negative value, V_∞ still moves in a positive x-direction. This means that V_{rel} is larger when the structure moves against the direction of V_∞. These significant changes in V_{rel} cause the AoA to change as seen in Figure 4.9 and so the power curve to oscillate significantly, peaking where V_{rel} is the largest, as can be seen in Figure 4.8.

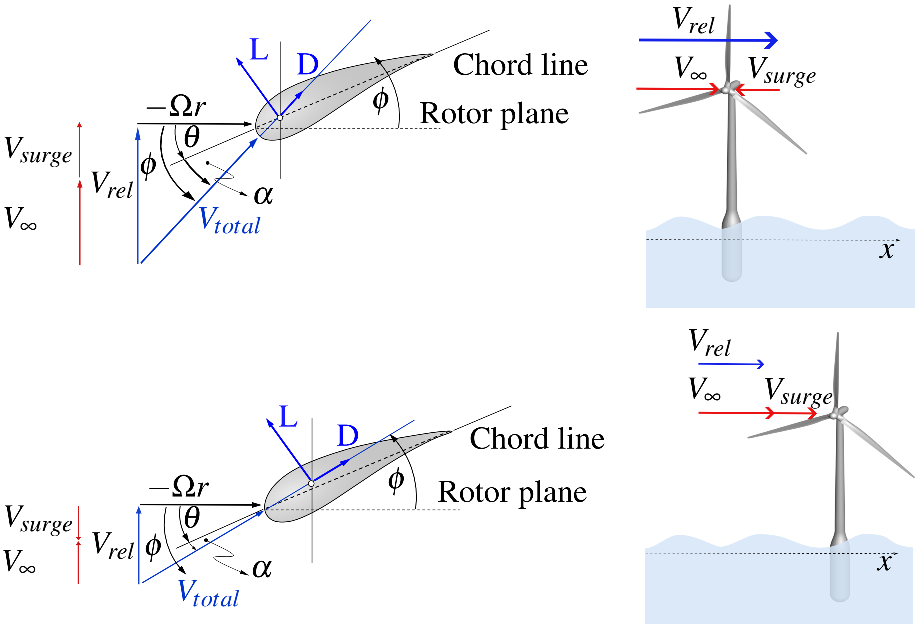

Figure 4.9: Relative airflow due to a surge motion.

The wake profile of the isolated surge motion is seen to be fairly regular, although starting vorticies can be seen in the sideview of the propagation seen in Figure 4.10. The surge motion does not significantly impact the wake structure within the given simulation time.

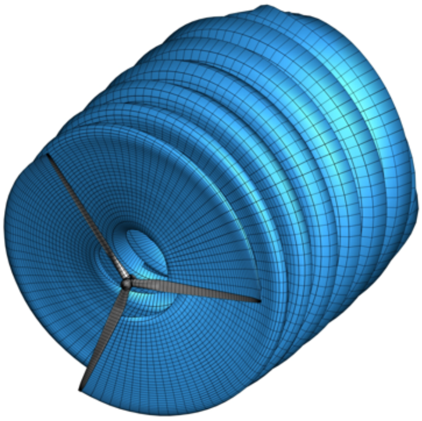

(a)

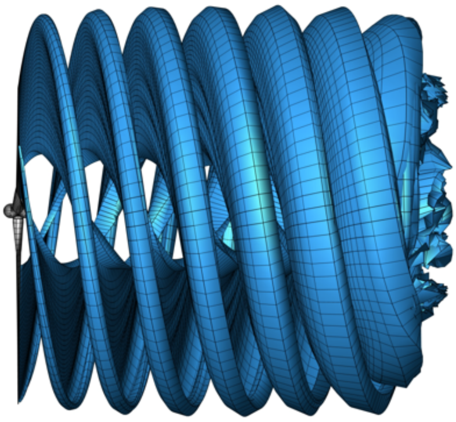

(b)

Figure 4.10: Wake profiles of *Sim. B*, *Case 3*, isolated view and side view of the wake propagation.

Isolated Pitch

Further, the isolated pitch motion is investigated (*Sim. C*). Another motion parameter is to be considered in this case; the displacement, X_0. The displacement values can be found in [10]. This parameter is relevant for the pitch motion because of the initial tilt that the turbine experiences, likely due to the weight of the nacelle and rotor, making the turbine lean forward slightly. In all simulations with a pitch movement, this parameter is included. As seen in Figure 4.11 and Table 4.12 the power oscillates about the reference power. The varying amplitude of the power can be explained in the same way as for the isolated surge, and the reader is referred to Figure 4.9. The relative velocity varies as the turbine is pitched about the z-axis. Although the power of *Case 3* shows oscillation, the amplitude of the signal is 'only' 280.9, which is about half when compared to the power amplitude of the isolated surge. The complete simulation data and results can be found in Appendix E.

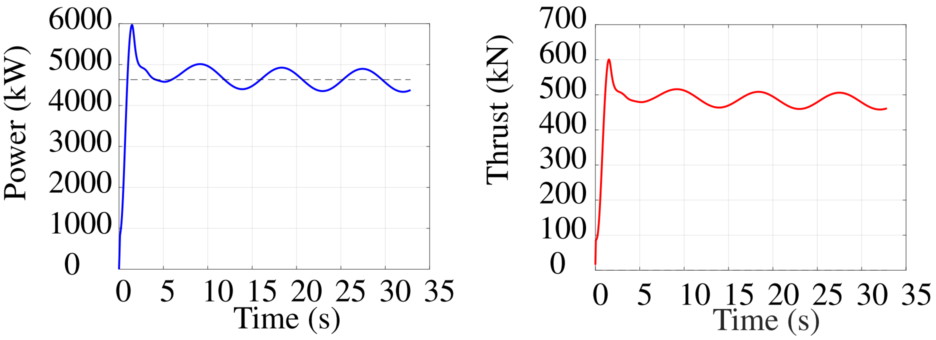

Figure 4.11: Power and thrust curve for isolated pitch (*Sim. C*, *Case 3*).

Table 4.12: Power data of isolated surge simulations

Case nr.	Mean P (kW)	Freq P (Hz)	Amp. P (kW)	Max. P (kW)
1	4615.4	0.1087	63.1	4678.5
2	4615.8	0.1094	172.1	4788.0
3	4615.8	0.1100	280.9	4896.7
4	4294.7	0.1068	60.2	4354.9
5	4294.5	0.1087	163.8	4458.2
6	4294.8	0.1087	267.6	4562.4
7	3312.1	0.1015	11.7	3323.8
8	3356.0	0.1156	146.6	3502.6
9	3355.4	0.1056	236.5	3591.9
10	1841.1	0.1015	20.4	1861.5
11	1773.9	0.1186	25.2	1799.1
12	1872.5	0.1179	195.9	2068.5

The wake profile also shows similar tendencies as that of the isolated surge as seen in Figure 4.12. It is generally steady, but does show the starting vortex as is expected.

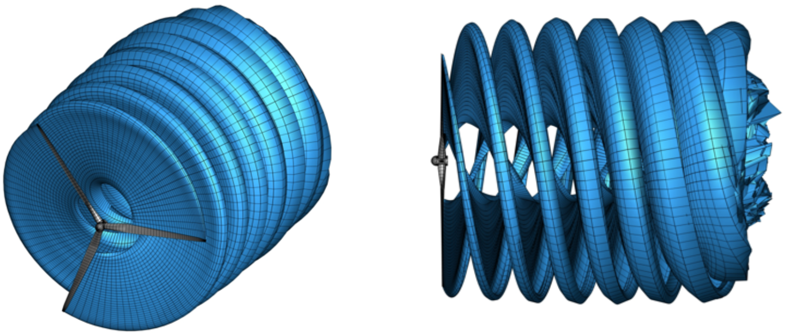

Figure 4.12: Wake profiles of *Sim. C*, *Case 3*, isolated view and side view of the wake propagation.

4.2.2 Combined kinematics

The three motions described in this chapter are then combined creating the following simulations; heave and surge (aligned and unaligned) (*Sim. D* and *Sim. E*, respectively), heave and pitch (*Sim. F*), surge and pitch (*Sim. G*) and lastly heave, surge and pitch (*Sim. H*). The combined simulations share the same simulation values as presented in Table 4.8 and the amplitudes of the motions have the same values as presented in Table 4.9. There is an addition of a phase angle, ϕ_p for the combined cases that include surge and/or pitch. The values of this angle can be found in [10].

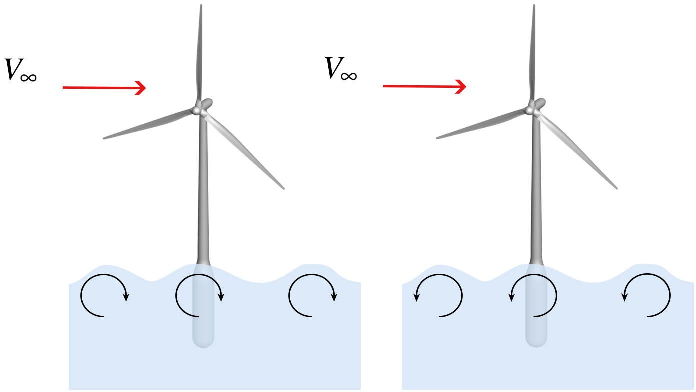

Figure 4.13: Schematic of the aligned and unaligned heave and surge motion.

Combined Heave and Surge

In the case of combining heave and surge, there are two simulation cases; aligned (*Sim. D)* and unaligned (*Sim. E)*. The aligned case is where the circular motion of the waves travels in the same direction as V_∞, and the unaligned case is where the waves travel in the opposite direction of V_∞, as seen in Figure 4.13. In this work, linear wave theory is considered for the waves, for the purpose of simplification. Another option is to consider Stokes drift in the wave motion; however, the focus of this thesis is to investigate the effect that motion has on the final power output, not the physical concept of waves. Therefore, incorporating Stokes drift is beyond the scope of this thesis.

The aligned and unaligned simulations show very similar power and thrust curves, but with a 180° phase angle shift as seen in Figure 4.14. The mean power output in these simulations has values similar to those of the *reference case*, but the amplitudes are significant. *Case 3* has an amplitude of 623.5 kW (aligned) and 614.3 kW (unaligned). It is then clear that the direction of the waves with respect to V_∞ does not greatly affect the power.

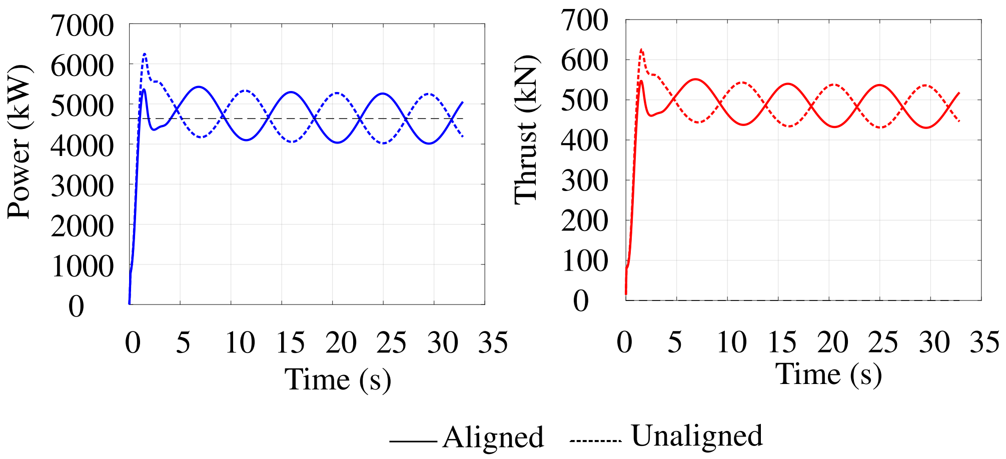

Figure 4.14: Comparison of aligned and unaligned Heave and Surge motion power and thrust curves.

To investigate the origin of the amplitudes seen in Figure 4.14, the power curves of the isolated heave and the isolated surge are compared with the power curve of the combined heave and surge (aligned) in Figure 4.15. It is seen that the power curve of the isolated surge (in green) and the power curve of the heave and surge combined (in red) are nearly identical. Therefore, it is clear that the dominant impact in the power curves of the two simulation cases of combined heave and surge is the surge motion. This can be further verified by comparing the values of the amplitudes of the isolated surge (Appendix D) with the power amplitudes of the combined surge and heave powers aligned and unaligned (Appendix F and Appendix G, respectively).

Further, the wake profile of the unaligned simulation (*Sim. E*, *Case 3*) is analysed. Figure 4.17 shows that the wake profile is generally affected by the heave motion and is characterised by its vertical oscillation. Figure

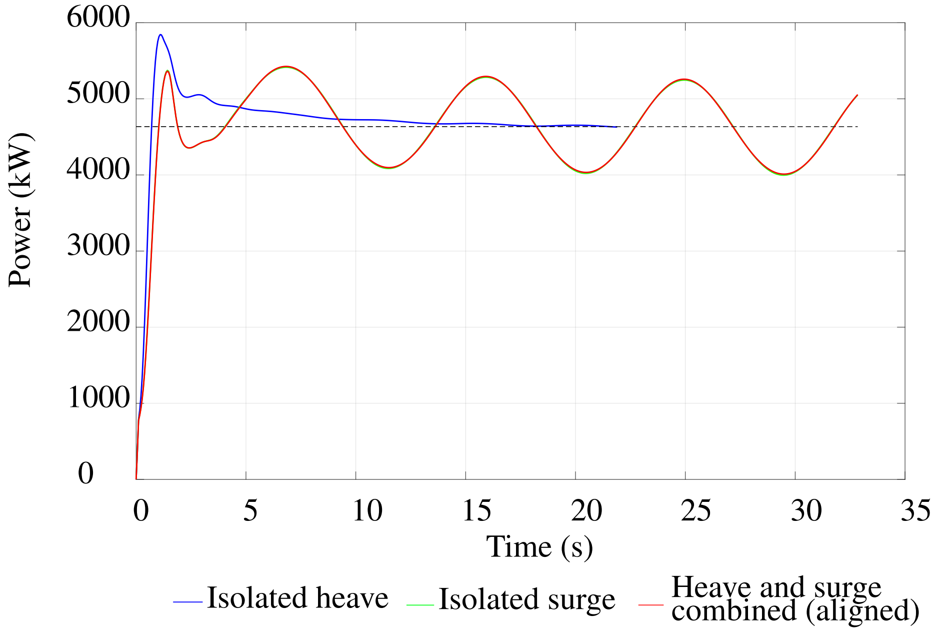

Figure 4.15: Isolated heave and surge power curve compared with the combined power curve of heave and surge (aligned).

4.17 shows the evolution of the wake further downstream of the turbine. The oscillations are more pronounced and irregular, suggesting that the flow has become unstable. This is a common behaviour due to the nature of the UVLM and with enough simulation time, the wake becomes chaotic. The reader should note that the wake profile included is only that of *Sim. E*, the reason being that the wake profiles of the aligned and unaligned simulations are nearly identical for *Case 3*.

The complete simulation data and results of the aligned and unaligned results can be found in Appendix F and Appendix G respectively.

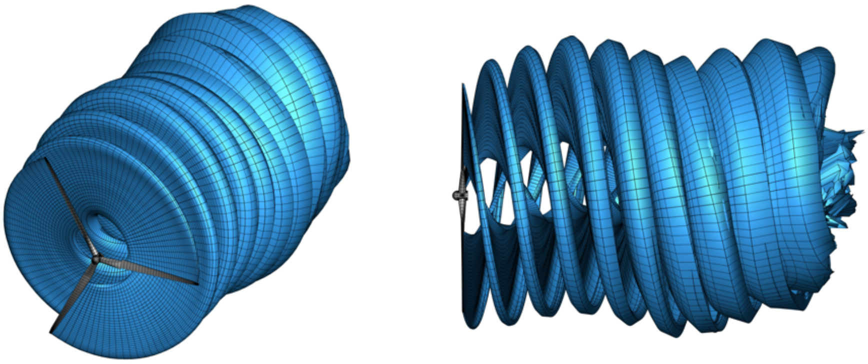

Figure 4.16: Wake profiles of *Sim. E*, *Case 3*, isolated view and side view of the wake propagation.

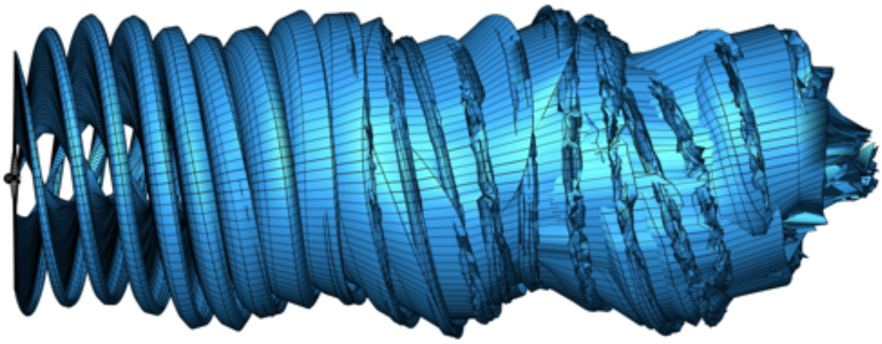

Figure 4.17: Wake profile of *Sim. E*, *Case 3*, sideview with longer simulation time.

Heave and Pitch

The simulation case for the combined heave and pitch (*Sim F*), is defined so that when $\hat{A}_{\text{heave}}$ is at its maximum positive amplitude value, then $\hat{A}_{\text{pitch}}$ is also at its maximum positive amplitude value. A schematic of the simulation can be seen in Figure 4.18.

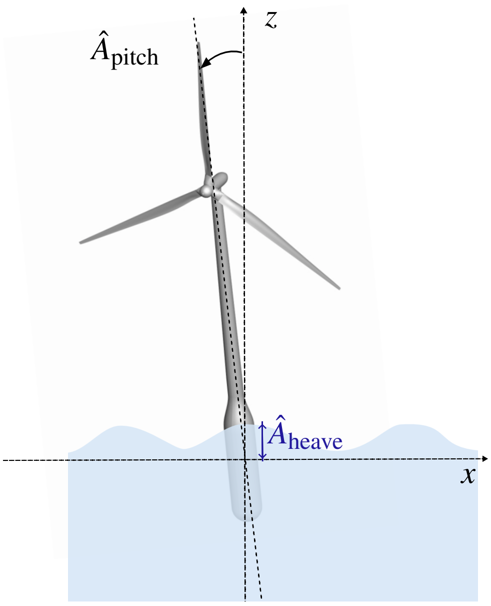

Figure 4.18: Schematic of heave and pitch scenario (*Sim. F*).

The power and thrust of the combined heave and pitch simulation are seen in Figure 4.19 for *Case 3*. There is a clear oscillation about the reference power. The frequency of the power for *Case 3* is 0.1094 Hz, which is close to the frequency of the imposed motions.

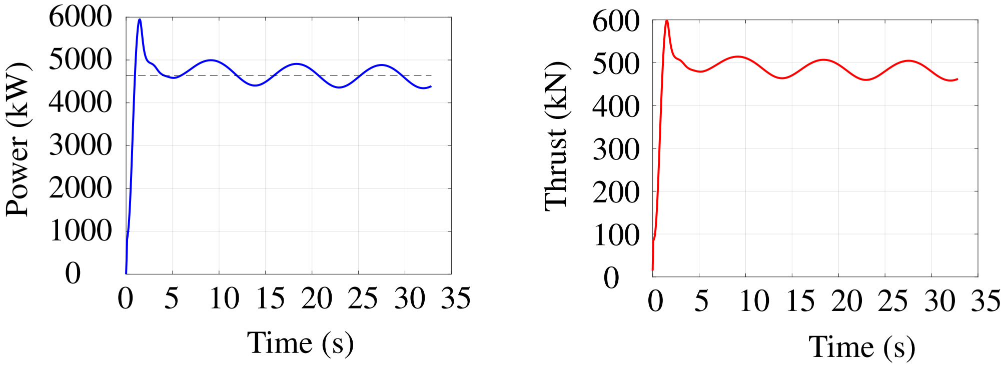

Figure 4.19: Power and thrust curve for heave and pitch simulation (*Sim. F Case 3*).

Figure 4.20 shows a comparison of the power curves of the isolated heave (*Sim. A*) and pitch (*Sim. C*) and the combined heave and pitch (*Sim. F*). It also seen in this scenario that the heave has a small effect on the power output as the power curve of the combined motion is nearly identical to that of the isolated pitch. This is also validated by comparing the amplitudes of the isolated pitch (Appendix E) with the amplitudes of heave and pitch combined (Appendix H). It is clear that the amplitude values of the combined motion are similar to those of the isolated heave.

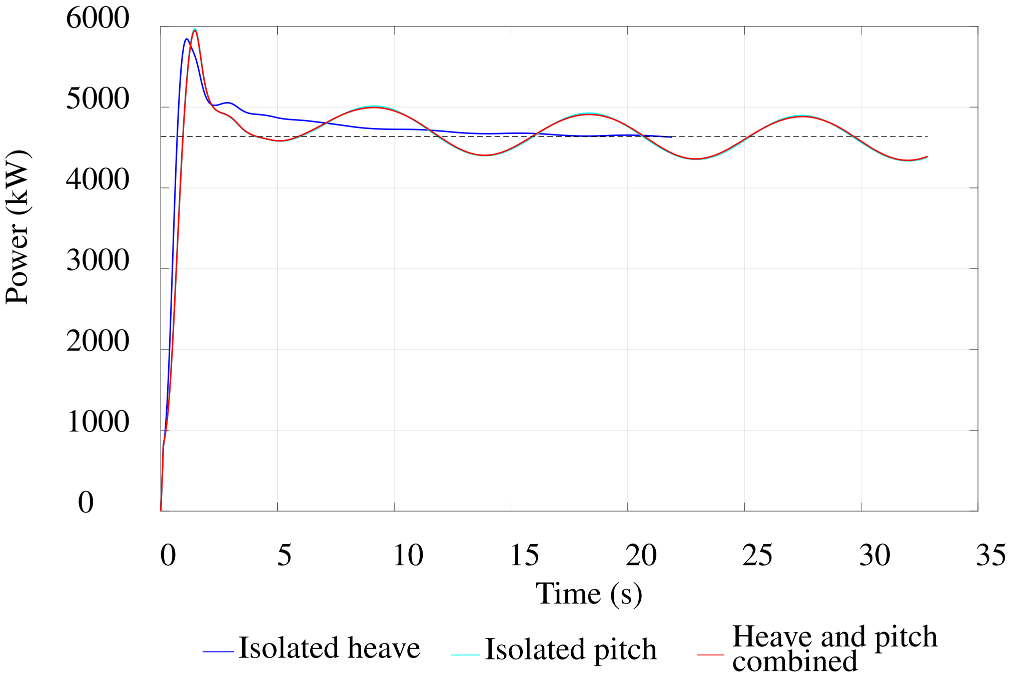

Figure 4.20: Isolated heave and pitch power curve compared with the combined power curve of heave and pitch.

The wake propagation is influenced by the heave motion, as seen previously. Figure 4.21 shows the isolated view as well as the rear end of the wake profile. In the rear of the FOWT we can observe the structure of the starting vortex, which is irregular and jagged, indicating a chaotic flow. The side view of the wake profile seen in Figure 4.22 shows the same oscillating trend as for the combined heave and surge simulation (*Sim. E*).

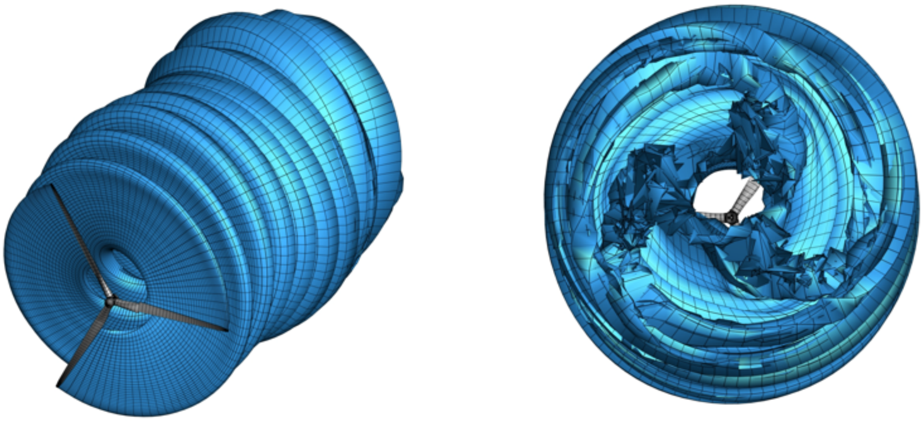

Figure 4.21: Wake profiles of *Sim. F*, *Case 3*, isolated view and rear view of the wake propagation.

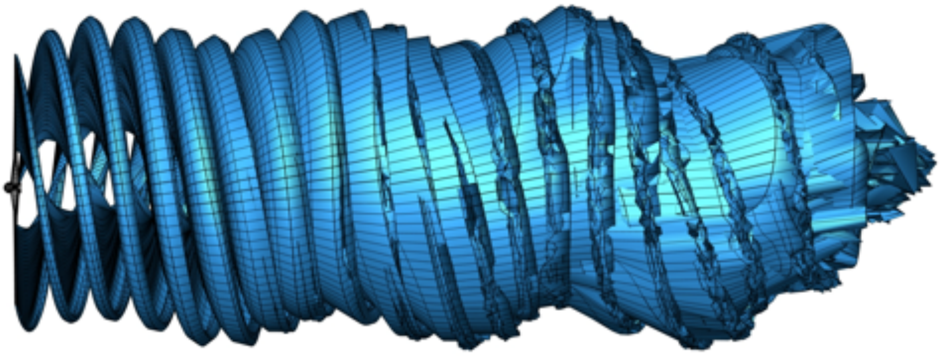

Figure 4.22: Wake profile of *Sim. F*, *Case 3*, sideview with longer simulation time.

Surge and Pitch

Further, the combined surge and pitch simulation is investigated (*Sim. G*). Here, the amplitudes of the motions are inspired by the work in [10]. It is seen from the previous simulations that the motions that affect the signal of the power output the most are the surge and the pitch, making this simulation case especially interesting. Figure 4.23 shows how the power and thrust signal oscillates about the reference power. Like in previous simulations, the mean power of *Sim. G*, *Case 3* is very similar to that of *the reference case*. The frequency value is 0.1107 Hz, which approximately match the frequency of the imposed motions, which is 0.11 Hz.

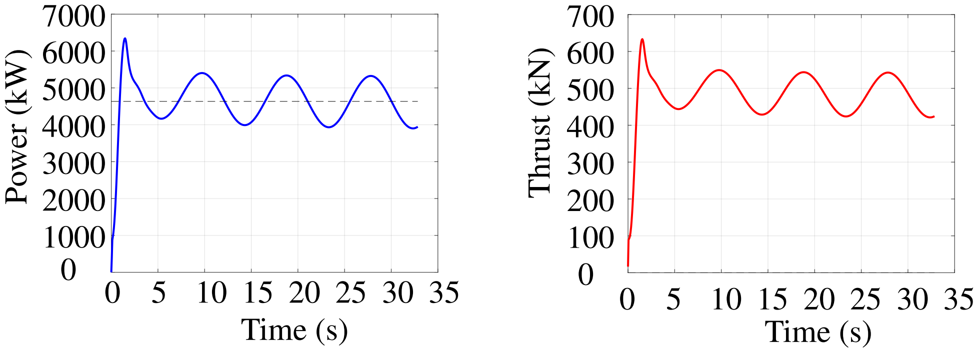

Figure 4.23: Surge and Pitch motion

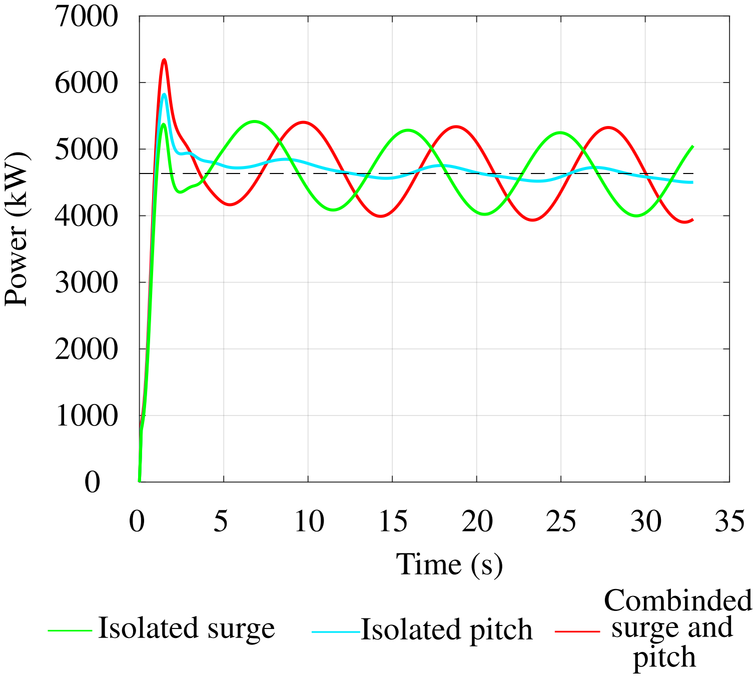

Figure 4.24: Isolated surge and pitch power curve compared with the combined power curve of surge and pitch.

To investigate which of the two motions has the greatest influence on the combined power, the power of the combined case is plotted together with the power of the isolated surge and pitch for *Case 3* as seen in Figure 4.24. It is observed that the power curve of the combined motion is more similar to that of the isolated surge, but experiences a slight shift. The power amplitudes of the combined surge and pitch can be found in Appendix I. The amplitudes of the individual motions can be found in Table 4.12 and Table 4.11. From these tables, it is further verified that the power amplitudes of the combined surge and pitch has more similar amplitude values to that of the isolated surge.

Further, the wake profile of the simulation is analysed. Figure 4.25 shows that the wake profile is more steady compared to the simulations in which the heave is involved. The starting vorticies can also be seen in this scenario as discussed previously.

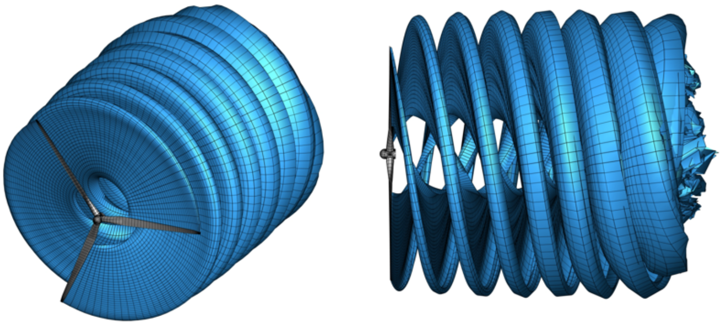

Figure 4.25: Wake profiles of *Sim. G*, *Case 3*, isolated view and side view of the wake propagation.

Surge, Pitch and Heave

Lastly, all three kinematics are combined (*Sim. H*). Figure 4.26 shows the power and thrust curve of *Case 3*. The mean power of this case is also similar to that of *the reference case*, but the amplitude is much larger. The frequency of the power of *Case 3* is 0.1107 Hz.

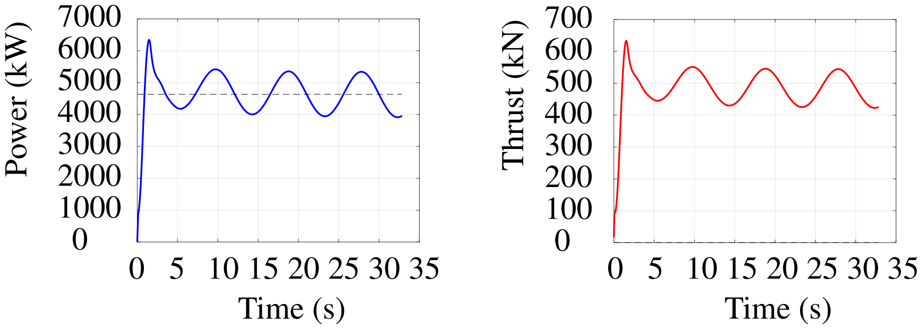

Figure 4.26: Power and thrust curve for combined heave, surge and pitch (*Sim. H Case 3*).

From previous simulations, we see that the power is most greatly affected by the surge. To conduct a final certification of this, the power curves of all three isolated motions are plotted and compared with the power curve of the motion combining all three as seen in Figure 4.27. It is confirmed that the surge motion is the dominant one in the combined power, as the shapes of the curves are very similar. However, the power curve of the combined motion displays a slight shift, which is likely due to the pitch motion.

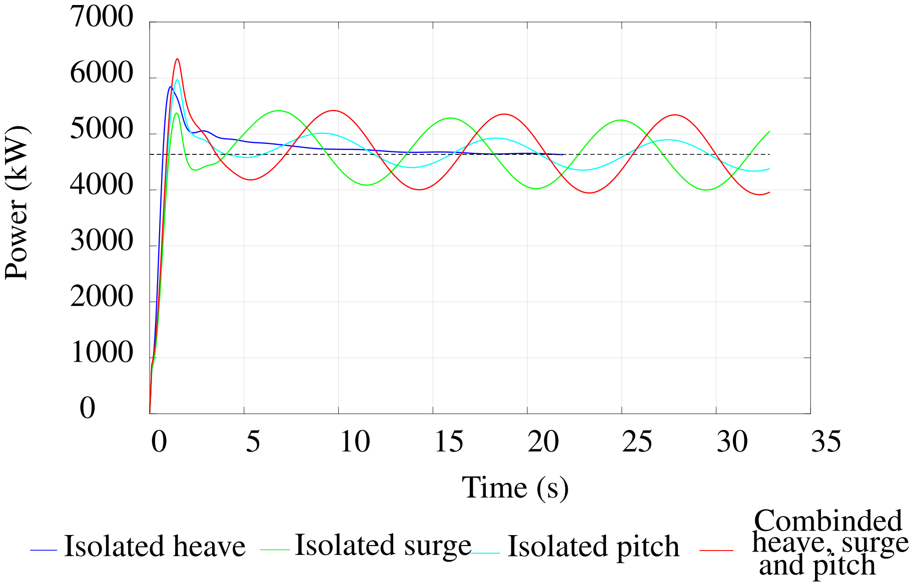

Figure 4.27: Isolated heave, pitch and surge power curve compared with the combined power curve of heave, pitch and surge.

The wake propagation is, as expected, influenced by the heave motion as seen in Figure 4.28. Starting vorticies can be observed also in this simulation by analysing the rear of the turbine. Figure 4.29 shows a side view of the wake propagation, and it is seen that the flow becomes irregular further downstream.

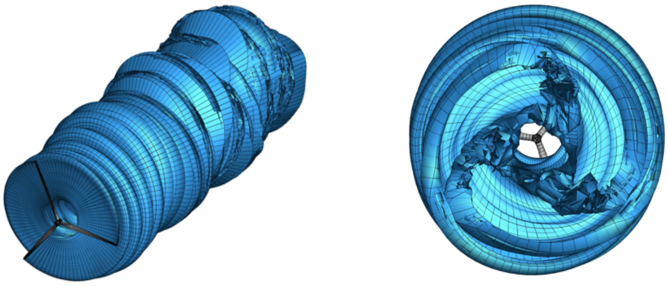

Figure 4.28: Wake profiles of *Sim. H*, *Case 3*, isolated view and rear view of the wake propagation.

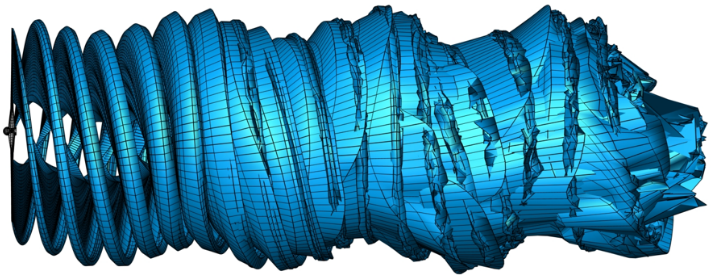

Figure 4.29: Wake profile of *Sim. H*, *Case 3*, side view with longer simulation time.

4.3 Wave Effect on the Output Power

Until now, I have investigated the influence of three motions on the turbine. These motions were imposed though somewhat inspired by known wave patters [10]. In this part, I will analyse how waves with different amplitudes affect the power output of the FOWT (*Sim. I*). However, the FOWT is considered without motion. It is beyond the scope of this thesis to calculate the forces done on the structure by the wave. Therefore, I present only the effect that a wave has on a stand-still structure where $\Psi = 0\,^{\circ}$. The wave is modelled as a boundary surface to the UVLM and its kinematic is imposed. The propagation of the sea waves is aligned with the free stream velocity.

There are three wave simulations with different amplitudes; *Case 1*:$A_{\text{wave}} =$ 5m, *Case 2*:$A_{\text{wave}} = 10$ m and *Case 3*:$A_{\text{wave}} = 15$ m. The first simulation has the amplitude that is used in [10], and the other two are magnified versions of the same wave to investigate the influence of the A_{wave}. All three waves have common simulation parameters as seen in Table 4.13.

Table 4.13: Waves simulation parameters

Parameter	Value
Sea depth, h	70 m
Wave number, k	0.0498
Nr. of waves	1
Period of wave, T	9 s

The wave number is determined using the dispersion relation, rearranged from Eq. 2.33 to solve for K:

$$k = \frac{\omega_{wave}^2}{g \cdot \tanh(hk)}, \tag{4.6}$$

where $\omega_{wave} = \frac{2\pi}{T}$, and T is found in [10] and equals 9 s. Even though this parameter is presented in relation to a wave with an amplitude of 5 m, I consider this T for all wave simulations. Eq. 4.6 is a nonlinear equation that can be solved numerically using an iterative method. I use the *Newton-Raphson method* to solve for k, where the function to solve and the derivative of that function is given by:

$$f(k) = gk \cdot \tanh(hk) - \omega_{wave}^2, \tag{4.7}$$

$$f'(k) = g\left(\tanh(hk) + hk \cdot \text{sech}^2(hk)\right), \tag{4.8}$$

where $\text{sech}(x) = \frac{1}{cosh(x)}$. I start with an initial guess for k:

$$k_0 = \frac{\omega_{wave}^2}{g} = \frac{(0.0698 rad/s)^2}{9.81 m/s^2} \approx 0.0497. \tag{4.9}$$

After a few iteration steps using the *Newton-Raphson* formula:

$$k_{n+1} = k_n - \frac{f(kn)}{f'(kn)}, \tag{4.10}$$

I find that k converges to approx. 0.0498. Using these simulation parameters, the waves are generated in `UVLMeshGen` together with a stand-still NREL 5MW turbine, and the power and thrust parameters of the turbine are analysed using the `VLMSim`. The results related to the power output of the turbine can be seen in Table 4.14 and the thrust values can be found in Appendix K.

Table 4.14: Power data of wave Simulations with stand still tower

Case nr.	Mean P (kW)	Freq P (Hz)	Amp. P (kW)	Max. P (kW)
1	4733.4	0.2000	6.2	4739.6
2	4836.8	0.2300	15.6	4852.3
3	4953.4	0.1590	26.5	4980.0

The output frequencies do not equal 0.11 Hz, and it unclear why this is the case. It could be argued that the waves are affecting the FOWT in a similar way to the isolated heave, where it was also seen that the output frquencies did not equal 0.11 Hz. For all the wave simulations, the power values are actually seen to be higher than those of the reference case. I suggest that this is due to the well-known *blocking effect*. Due to the proximity of the turbines to the boundary surface, the airflow pattern is altered around the blades. The result is a cushioning effect in which the induced drag is reduced and the lift is increased [43]. Figure 4.30 shows the power and thrust for *Case 1* and it is seen that the power oscillates around the reference power. The oscillation of the power is a bit larger for *Case 2* as seen in Figure 4.31, whilst *Case 3* shows the largest power oscillation, suggesting that the blocking effect is higher when the amplitude of the wave is greater as seen in Figure 4.32.

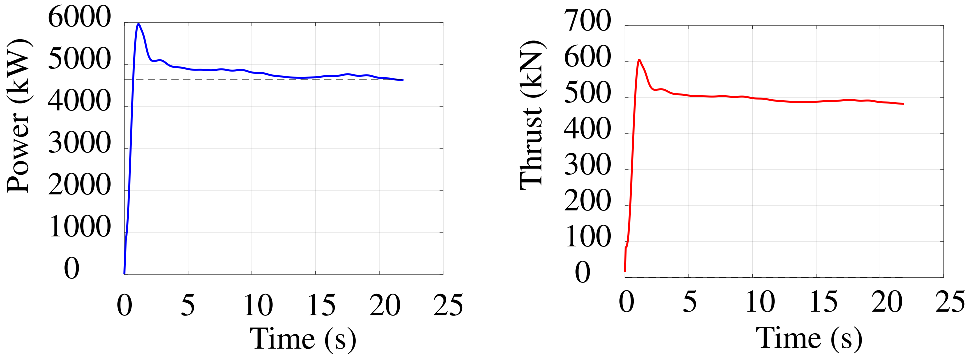

Figure 4.30: Power and thrust curve for wave simulation (*Sim. I Case 1*).

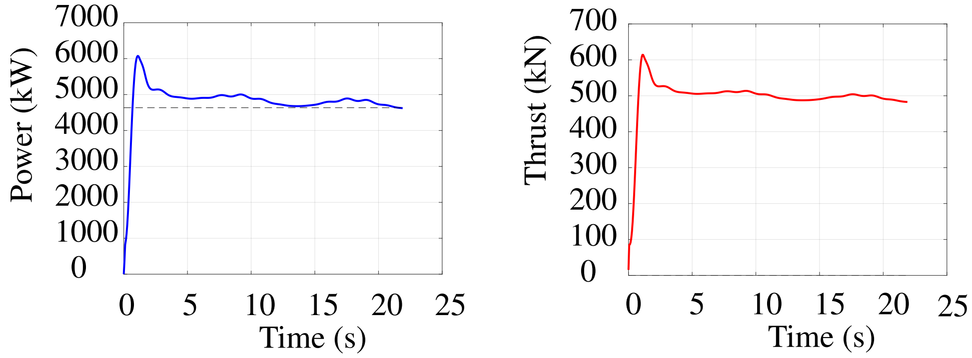

Figure 4.31: Power and thrust curve for wave simulation (*Sim. I*, *Case 2*).

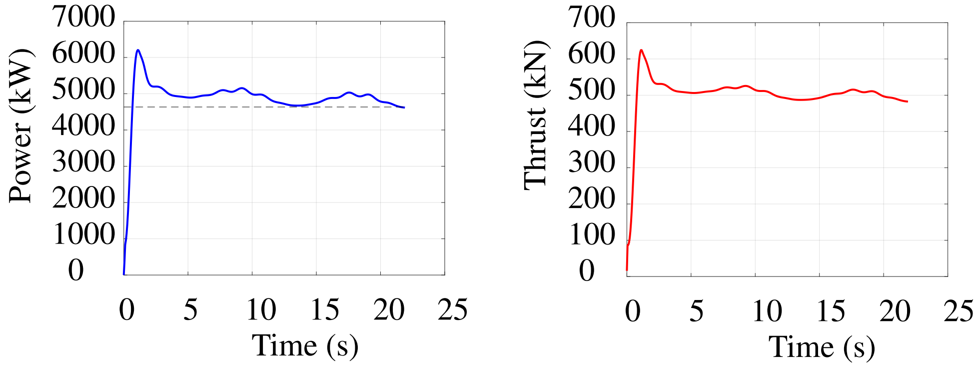

Figure 4.32: Power and thrust curve for wave simulation (*Sim. I*, *Case 3*).

Figure 4.33 shows an isolated view of the wake profiles of the three cases. It is seen that the wave does not significantly influence the wake propagation even at magnified scales. This is further confirmed in Figure 4.34, where the wake profiles are seen from the side. Here, the wake profile does not change significantly either. In this figure, the power curves are also plotted underneath the wake profile for visualisation purposes. A trend is observed; the power curves peak where A_{wave} is at its largest. This further validates the suggestion that the blocking effect is increased when the distance between the FOWT and the sea boundary level is decreased.

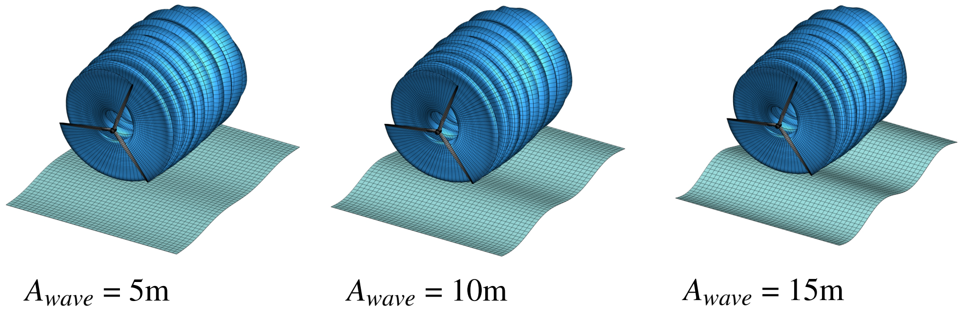

A_{wave} = 5m A_{wave} = 10m A_{wave} = 15m

Figure 4.33: Wake profiles of *Sim. I*, *Case 1, 2* and *3*, isolated view.

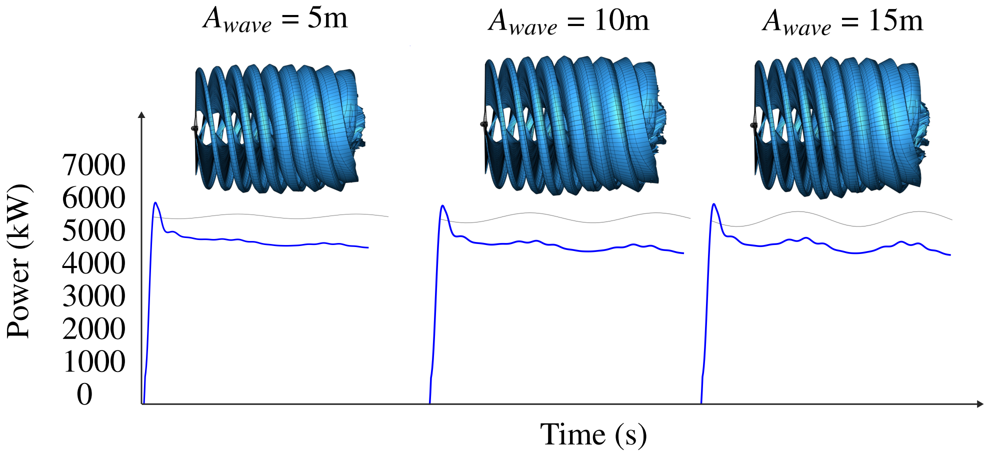

Figure 4.34: Wake profiles (side view) and power curves of *Sim. I*, *Case 1, 2* and *3*.

4.4 Full FOWT Simulation

As described in subsection 4.2, only the turbine blades are simulated. As a showcase, the full FOWT is simulated with no motion except the rotation of the blades and Ψ= 0°(*Sim. J*). There are three simulation cases; *Case 1* is only the FOWT, *Case 2* is the FOWT and a moving sea, and *Case 3* is a FOWT with a heave motion $\hat{A}_{\text{heave}} = 5$ m and a moving sea. The waves have the same simulation parameters as seen in Table 4.13. The power-related results can be found in Table 4.15 and the thrust results can be found in Appendix L. Figure 4.35 shows the three cases plotted in one graph. The three curves are fairly similar, especially *Case 2* and *Case 3*. However, *Case 3* show slightly smaller peaks, which is likely because the other two cases experience a larger blocking effect as described in subsection 4.3. It is seen that the signal oscillates and ruptures. This is expected and is likely due to the inclusion of the tower in the FOWT. Also in this simulation is the frequencies seen to not equal 0.11 Hz. This might be due to the rupture wake when passing in front of the tower (*tower shadow*), because of the heave motion as seen previously, or a combination of these phenomena.

Table 4.15: Power data of full FOWT simulations

Case nr.	Mean P (kW)	Freq P (Hz)	Amp. P (kW)	Max. P (kW)
1	4652.4	0.2000	0.2	4652.6
2	4652.8	1.6600	3.5	4656.3
3	4653.1	1.3100	0.1	4653.2

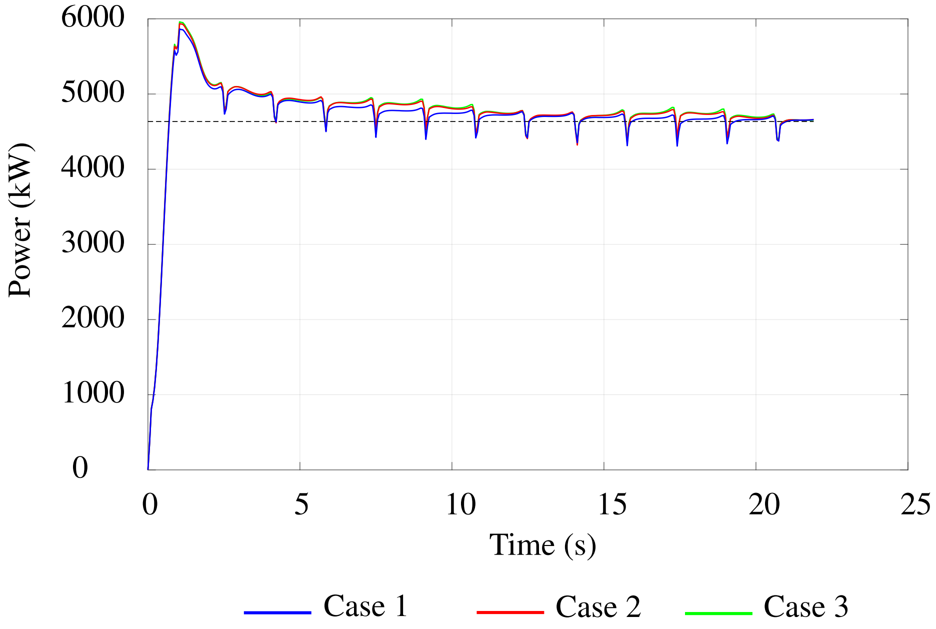

Figure 4.35: Power and thrust curves of full FOWT *Sim. J*.

Figure 4.36 shows the wake profile of *Case 1*. The propagation is generally stable, although further downstream the wake becomes disrupted, which once again can be explained by the formation of starting vorticies.

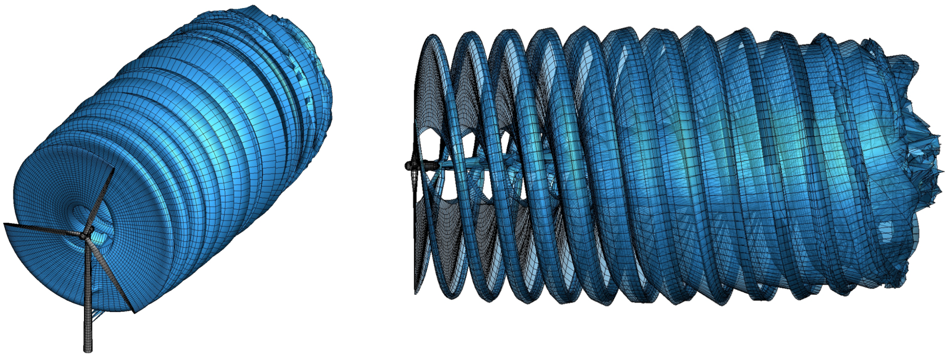

Figure 4.36: Wake profile for *Sim. J*, *Case 1*.

Another important point to note is the interaction between the wakes and the tower. It can be seen in Figure 4.37 that the flow experiences a rupture. It is likely that the troughs seen in the power curve of *Case 1*(Figure 4.35) are caused by this phenomenon.

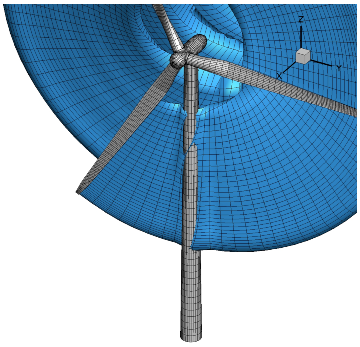

Figure 4.37: Wake and tower interaction.

4.5 Multiple FOWTs Simulation

Lastly, two showcases consisting of two FOWTs are presented. The two wind farms investigated each consist of two turbines placed in different layouts (*Sim. K*). In both cases, the motion imposed on the turbine is the heave motion where $\hat{A}_{\text{heave}}$= 5m. The waves have the same simulation parameters as seen in Table 4.13.

In *Case 1*, one turbine is placed downstream of another, so FOWT2 is influenced by the wake of FOWT1. The waves are aligned with V_∞ which has a 0°angle with respect to the FOWTs, so $\Psi = 0°$. The layout of the wind farm can be seen in Figure 4.38.

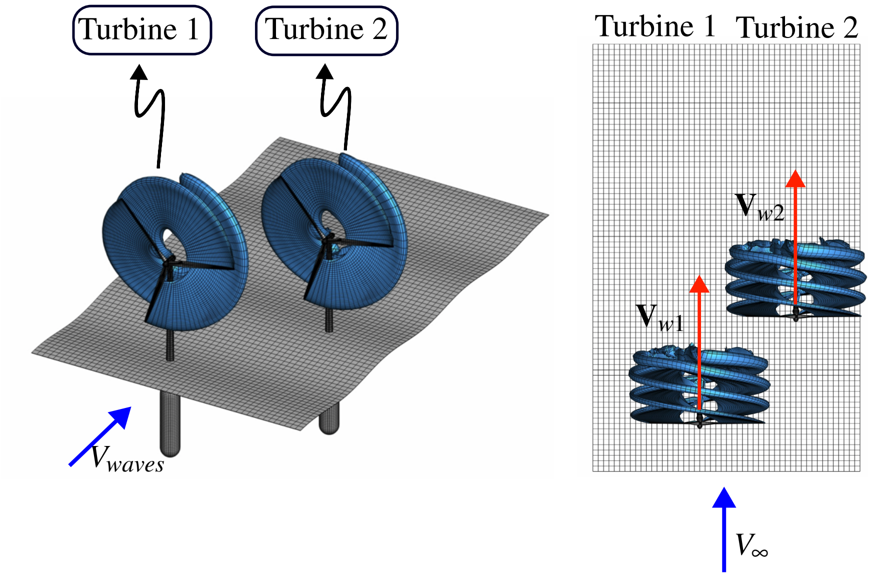

Figure 4.38: WT farm layout of *Case 1*.

The mean power of FOWT2 is lower than the mean power of FOWT1 by 5,7 %. The amplitudes of FOWT2 are also much higher than those of FOWT1 as seen in Table 4.16. The frequencies of the power are seen to not equal 0.11 Hz. This is likely because heave is the only motion imposed in this simulation, and we recall that for the case of isolated heave, $f \neq 0.11$ Hz. In Figure 4.39 it is seen that the signal of FOWT2 starts to oscillate at $t \approx 8s$ (indicated in yellow). This is where the wake of the first FOWT reaches the second FOWT. In this figure, the power curve of *Sim. J*, *Case 3* is also plotted, as this simulation has the exact same parameters as the other two FOWTs. Therefore, it serves as a reference of how the FOWTs would act if they were not impacted by each other. It is seen that the power curve of the stand alone FOWT is similar to the power curve of FOWT1. It is however, not identical, indicating that both FOWTs are actually affected by the wind farm layout, not just the downstream one. However, the second FOWT is partially influenced by the $\mathbf{V}_w$ downstream of FOWT1. The velocity of $\mathbf{V}_w$ is reduced and turbulence is increased. Recalling eq. 2.1, where the V_∞ is cubed, it is evident that the incoming velocity that the turbine experiences is significant in power production. The interference between the FOWTs can be seen in Figure 4.40, where the power curves are plotted with the wake propagation.

The reader should note that the two turbines are simulated simultaneously in time and that the power curves are actually parallel, as seen in Figure 4.39. However, for visualisation purposes, I have plotted the power curves with a shift of approximately 8 s which is the time it takes for the wake of FOWT1 to start overlapping with the wake of FOWT2.

Table 4.16: Power data of multiple FOWT simulations (*Case 1*).

FOWT nr.	Mean P (kW)	Freq P (Hz)	Amp. P (kW)	Max. P (kW)
1	4678.6	0.50	288.5	4967.1
2	4412.5	2.61	572.9	4985.4

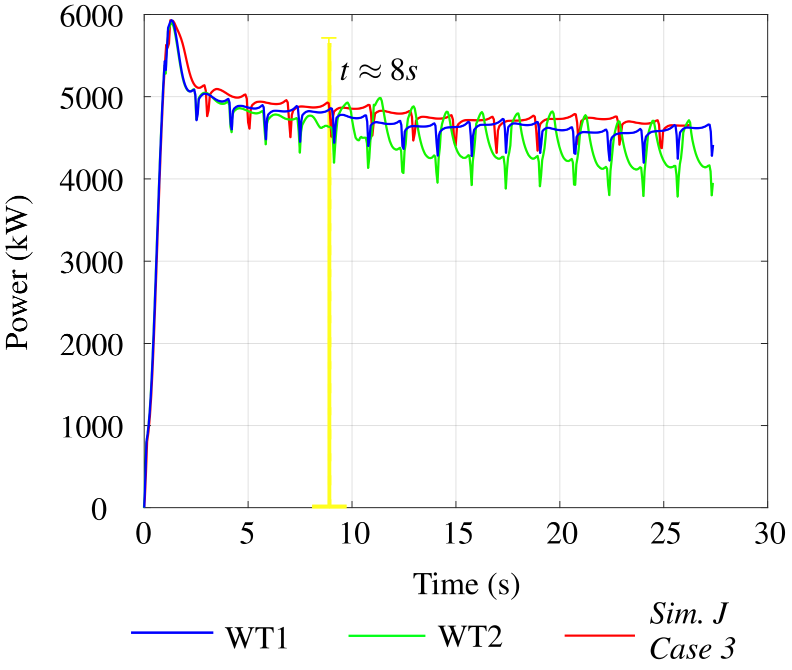

Figure 4.39: Power and thrust curve for multiple FOWTs (*Sim. K*, *Case 1*).

It is also evident from 4.41 that the wake of the FOWTs heavily influences each other. It is seen that the wakes are generally not influenced by each other before the interfere at approx. 8 s, and that the shape of the wake from a side view is influenced by the heave motion. This is again in line with the wake propagation of profiles studied before for heave motion. When wake 1 reaches wake 2, both wake profiles are affected. The wake of the downstream turbine is not only affected by the upstream turbine's wake but also contributes to a combined wake effect that reduces the power output of both turbines. The reader should also note that due to the presence of the wave, the results are also influenced by the blocking effect as discussed in subsection 4.3.

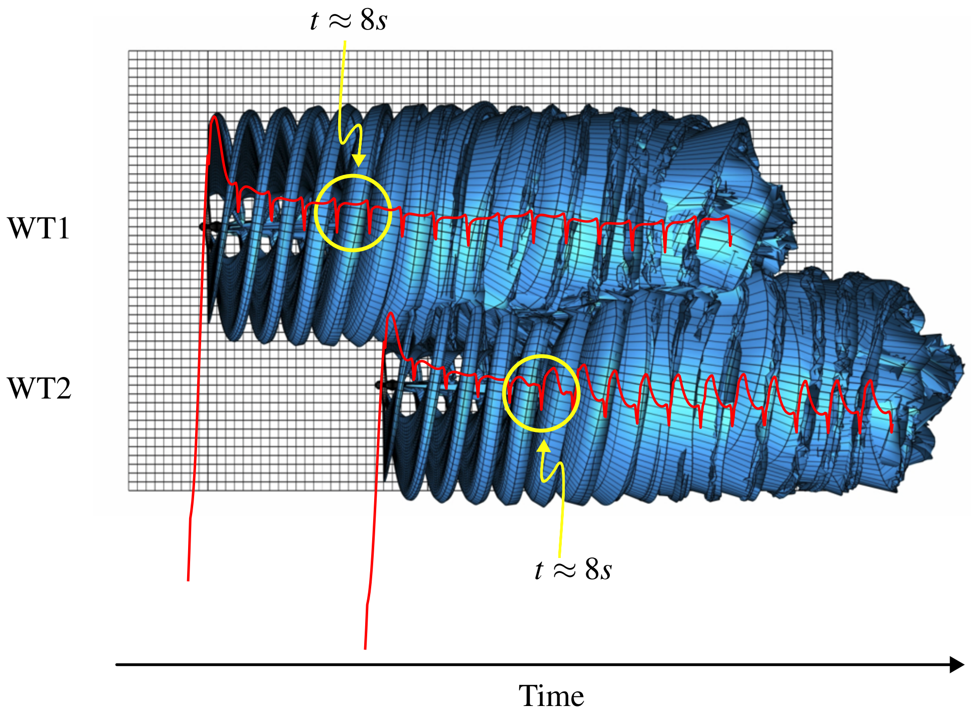

Figure 4.40: Wake propagation (side view) and power curves of *Case 1*.

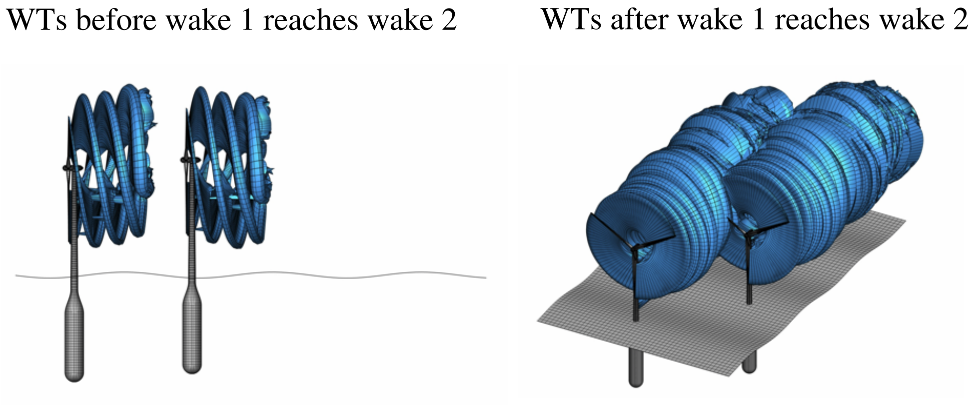
WTs before wake 1 reaches wake 2

WTs after wake 1 reaches wake 2

Figure 4.41: Wake propagation of *Case 1*, side view and isolated view.

Lastly, a final simulation of multiple FOWTs is analysed (*Case 2*). In this case, two turbines are located next to each other as seen in Figure 4.42. The turbines are placed facing the wind so that Ψ=0°, whilst the direction of the velocity of the waves V_{waves} is perpendicular to V_{∞}.

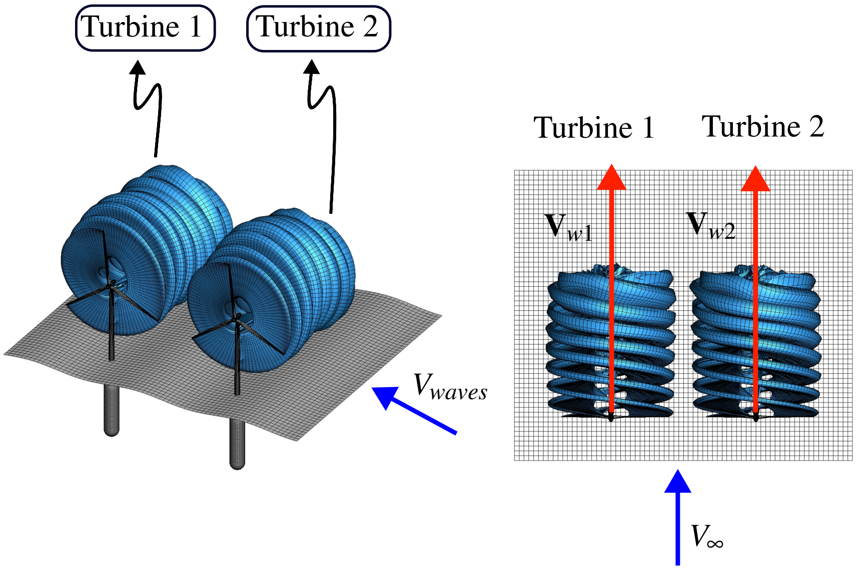

Figure 4.42: Wind Farm layout for *Case 2*.

Since the wakes of the FOWTs do not overlap, there is no visible influence on the power as seen in Figure 4.43. The power curves are very similar; this is further confirmed by examining the values in Table 4.17, where the mean powers, frequencies, amplitudes, and maximum powers are very similar. The mean powers of both FOWTs are close to those of *the reference case*. This is likely due to that the only motion imposed on it is heave, which was previously seen to not affect the power significantly. The presence of only heave motion could also explain why the frequencies do not equal 0.11 Hz for both *Case 1* and *Case 2*.

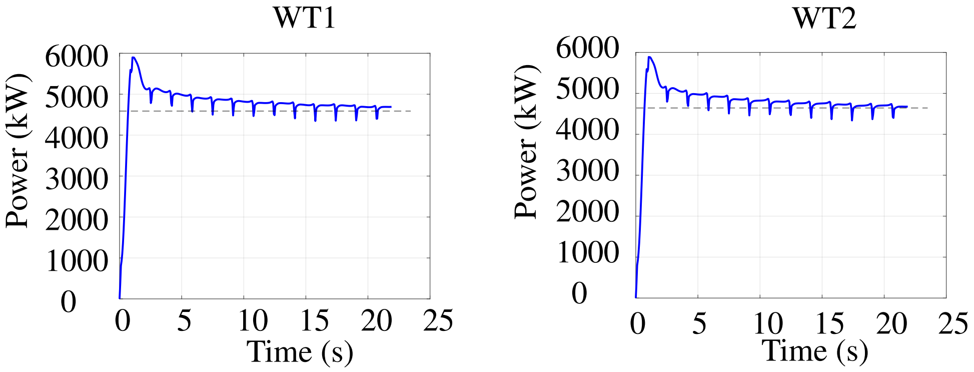

Figure 4.43: Power and thrust curve for multiple FOWTs (*Sim. K*, *Case 2*).

Table 4.17: Power data of multiple WT simulations (*Case 2*).

FOWT nr.	Mean P (kW)	Freq P (Hz)	Amp. P (kW)	Max. P (kW)
1	4691.1	1.30	23.2	4714.3
2	4675.5	1.30	63.2	4738.7

The wake propagation of *Case 2* is mainly influenced by the heave movement imposed on the FOWTs. Since the wakes do not overlap, in contrast to *Case 1*, the output is primarily affected by its own motion rather than by the wake of the neighbouring turbine. Figure 4.44 how the FOWTs are affected by the heave motion imposed on them. The top view shows that the wakes do not overlap, and the rear view shows the stating vortices.

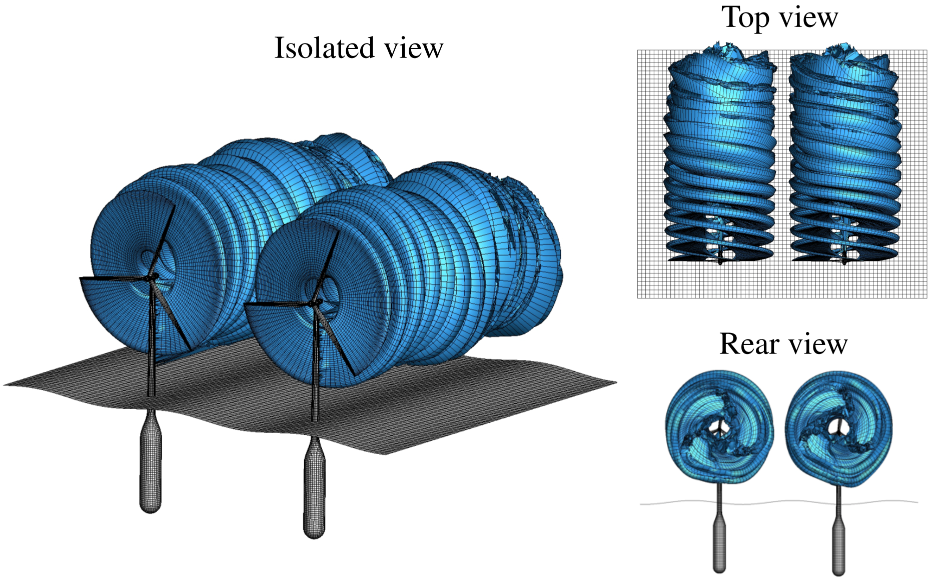
Isolated view

Top view

Rear view

Figure 4.44: Wake propagation of *Case 2*, isolated view, top view and side view.

In this section, I have explored the aerodynamic behavior and power output of FOWTs under the substructure motions of heave, surge and pitch. The isolated and combined effects of these motions were simulated and analysed, providing insights into how each type of motion influences the overall performance of the turbine. Some further simulations were conducted to investigate the effects a boundary layer had on the power output of a FOWT. Finally, some showcases of the whole FOWT and multiple FOWTs were presented.

Chapter 5

Conclusions and Future Work

This thesis has addressed how the power output of a FOWT is affected when motion is imposed on its substructure in an offshore environment. The motions of interest were heave, surge, and pitch, which are typical motions that a FOWT can experience due to a wave acting on the structure. This was done by generating and implementing a spar-type substructure and a wave mesh into the UVLM-based geometric processor `UVLMeshGen`, and simulating various scenarios using the aerodynamic simulator `VLMSim`. First, a verification of the simulation framework was conducted considering three turbines: The NREL 5MW, the DTU 10MW RWT and the Sandia 13.2 MW. Some adjustments were made to better develop a reference case based on the NREL 5MW turbine. Then, various simulation scenarios were defined to investigate the motions individually, combined, the presence of a sea wave, a full FOWT and multiple FOWTs in a wind farm.

It was found that the isolated motions of heave, surge, and pitch each affect the power output of the FOWT in different ways. The heave motion had a minimal impact on the power output, mainly due to its vertical nature, which does not significantly alter the relative velocity with respect to the wind. However, the wake propagation of the heave showed significant oscillation. The surge and pitch motions had more pronounced effects on the power, with surge motion being particularly impactful due to large displacement in the horisontal direction, altering the AoA and consequently the amplitudes of the power.

When combined, it was further confirmed that the surge had the predominant influence on the power output. It was seen that heave generally had a small influence on the power but continued to impact the wake profile even when combined with surge and/or pitch.

The inclusion of a wave boundary surface revealed that the presence of waves can significantly impact the power output of a stand-still FOWT. Different wave amplitudes were tested, showing that higher wave amplitudes can lead to more substantial variations in power output, underscoring the importance of considering wave dynamics in the design and analysis of FOWTs. It is suggested that this could be due to the well-known blocking effect.

Simulations involving multiple FOWTs highlighted the complex interactions between turbine wakes. The presence of neighbouring turbines and their respective wakes can significantly influence the power output of each turbine. Specifically, a FOWT located downstream of another FOWT showed reduced power output and increased disturbances in the flow.

The findings of this thesis provide a solid foundation for understanding the aerodynamic performance and power output of FOWT's. However, there are several areas where further research could significantly advance this field as there are some limitations to the simulation framework. First, including a probabilistic distribution of the wind would further increase the quality of the results as it more similar to real-life situations, than the wind profile used in this work. Secondly, the effect the wave boundary layer has on the power output of the FOWT should be further investigated. More complex wave spectrums can be imposed to investigate how more irregular waves will affect an FOWT. After this is done, integrating advanced hydrodynamic solvers to `UVLMeshGen` and `VLMSim` could capture the full range of interactions between the waves and the FOWTs. However, it is suggested to first investigate complex imposed waves to a stand still FOWT. Lastly, there are countless possibilities of wind farm layouts. I suggest that further research be conducted where the multiple FOWTs are placed in closer and farther proximity of each other compared to the simulations in this work. Further, it would be interesting to conduct simulations including more than two FOWTs to see how the power output of each individual turbine changes.

In summary, this thesis has presented the responses of FOWTs to various motions and wave interactions. These findings not only advance the current state of aerodynamic modelling for offshore wind turbines but also provide valuable insight to optimise the placement of FOWTs to maximise their power output and operational efficiency.

Appendix A

NREL 5 MW Validation

Table A.1: Varying the blade pitch angle with fixed rated conditions

Pitch angle (deg)	Power (kW)
8.0	2415.3
7.0	2971.2
6.0	3407.8
5.0	3725.2
4.0	3923.0
3.0	4001.7
2.0	3962.2
1.0	3805.5
0.0	3532.3
-1.0	3145.7
-2.0	2646.5
-3.0	2037.2
-4.0	1320.0
-5.0	498.2

Table A.2: Table of NREL 5 MW turbine performance under interpolation.

Θ (deg)	V_∞ (m/s)	Power (kW)	Thrust (kN)
4.5	12.25	4480.6	507.5
5.5	12.60	4549.2	473.3
7.3	13.30	4520.6	414.1
8.0	13.60	4463.3	392.2

Appendix B

DTU 10MW RWT Validation

Table B.1: DTU 10 MW RWT Simulation data and results

Θ (deg)	V_∞ (m/s)	Power (kW)	Thrust (kN)
0.000	8	1504.8	815.2
0.896	6	1233.3	512.8
2.751	4	773.9	242.7
4.502	12	7946.0	1277.6
7.266	13	9612.1	1086.7
9.292	14	10306.0	967.6

Appendix C

Isolated Heave Motion

Table C.1: Power data of isolated heave simulations

Case nr.	Ψ (deg)	$\hat{A}_{\text{heave}}$ (m)	Mean P (kW)	Freq P (Hz)	Amp. P (kW)	Max. P (kW)
1	0	1	4634.0	-	-	-
2	0	3	4645.4	0.06	0.2	4645.6
3	0	5	4647.2	0.215	6.0	4653.2
4	15	1	4314.7	6525	0.0	4314.7
5	15	3	4324.2	0.6299	1.4	4325.5
6	15	5	4326.8	0.2342	8.0	4334.8
7	30	1	3371.6	0.6299	6.2	3377.8
8	30	3	3375.7	0.7026	4.0	3379.8
9	30	5	3380.5	0.7942	1.4	3381.9
10	45	1	1886.0	0.6299	17.2	1903.2
11	45	3	1894.6	0.6198	14.4	1909.0
12	45	5	1903.0	0.567	10.5	1913.6

Table C.2: Thrust data of isolated heave simulations

Case nr.	Mean T (kN)	Amp. T (kN)	Max. T (kN)
1	483.7	-	-
2	484.7	0.1	484.6
3	484.7	0.7	484.0
4	440.8	0.0	440.8
5	440.2	0.1	441.3
6	441.4	0.7	440.6
7	325.8	0.4	325.4
8	325.8	0.3	325.5
9	325.7	0.1	325.6
10	178.2	0.8	177.4
11	178.2	0.7	177.4
12	178.1	0.6	177.5

Appendix D

Isolated Surge Motion

Table D.1: Power data of isolated surge simulations

Case nr.	Ψ (deg)	$\hat{A}_{\text{surge}}$ (m)	Mean P (kW)	Freq P (Hz)	Amp. P (kW)	Max. P (kW)
1	0	0.20	4620.5	0.1100	127.4	4747.9
2	0	0.61	4620.9	0.1107	378.8	4999.7
3	0	1.01	4622.2	0.1107	624.5	5246.7
4	15	0.20	4299.9	0.1121	121.4	4421.2
5	15	0.61	4300.6	0.1114	362.7	4663.3
6	15	1.01	4302.0	0.1107	598.0	4900.0
7	30	0.20	3264.1	0.1137	0.4	3264.5
8	30	0.61	3366.6	0.1142	317.3	3683.9
9	30	1.01	3367.8	0.1135	523.2	3891.0
10	45	0.20	1881.5	0.1137	1.4	1882.9
11	45	0.61	1885.7	0.1179	258.1	2143.8
12	45	1.01	1888.3	0.1156	417.1	2305.4

Table D.2: Thrust data of isolated surge simulations

Case nr.	Mean T (kN)	Amp. T (kN)	Max. T (kN)
1	482.5	10.9	471.6
2	482.6	32.4	450.2
3	482.7	53.3	429.3
4	439.6	10.0	429.6
5	439.7	29.9	409.8
6	439.8	49.2	390.6
7	317.9	22.2	340.1
8	325.5	23.2	302.3
9	325.6	38.3	287.2
10	173.6	11.9	185.5
11	178.4	15.0	163.4
12	178.5	24.4	154.1

Appendix E

Isolated Pitch Motion

Table E.1: Power data of isolated pitch simulations

Case nr.	Mean P (kW)	Freq P (Hz)	Amp. P (kW)	Max. P (kW)
1	4615.4	0.1087	63.1	4678.5
2	4615.8	0.1094	172.1	4788.0
3	4615.8	0.1100	280.9	4896.7
4	4294.7	0.1068	60.2	4354.9
5	4294.5	0.1087	163.8	4458.2
6	4294.8	0.1087	267.6	4562.4
7	3312.1	0.1015	11.7	3323.8
8	3356.0	0.1156	146.6	3502.6
9	3355.4	0.1056	236.5	3591.9
10	1841.1	0.1015	20.4	1861.5
11	1773.9	0.1186	25.2	1799.1
12	1872.5	0.1179	195.9	2068.5

Table E.2: Thrust data of isolated pitch simulations

Case nr.	Mean T (kN)	Amp. T (kN)	Max. T (kN)
1	482.1	5.4	476.7
2	482.1	14.7	467.4
3	482.1	24.0	458.1
4	439.2	5.0	434.2
5	439.2	13.6	425.6
6	439.2	22.2	417.0
7	324.9	4.2	320.8
8	324.8	10.9	314.0
9	324.8	17.6	307.2
10	175.7	1.0	174.7
11	177.8	7.5	170.3
12	177.7	11.8	165.9

Appendix F

Surge and Heave (Aligned)

Table F.1: Power data of combined heave and surge simulations (aligned)

Case nr.	Ψ (deg)	$\hat{A}_{\text{heave}}$ (m)	$\hat{A}_{\text{surge}}$ (m)	Mean P (kW)	Freq P (Hz)	Amp. P (kW)	Max. P (kW)
1	0	1	0.20	4620.8	0.1100	127.4	4748.2
2	0	3	0.61	4625.7	0.1107	378.7	5004.4
3	0	5	1.01	4634.6	0.1107	623.5	5258.1
4	15	1	0.20	4300.8	0.1121	120.5	4421.3
5	15	3	0.61	4304.5	0.1114	360.0	4664.5
6	15	5	1.01	4313.3	0.1107	593.3	4906.6
7	30	1	0.20	3266.9	0.1790	299.7	3566.6
8	30	3	0.61	3367.6	0.1142	310.0	3677.6
9	30	5	1.01	3373.9	0.1128	510.4	3884.3
10	45	1	0.20	1877.7	0.1740	127.0	2004.7
11	45	3	0.61	1674.3	0.2280	481.4	2155.7
12	45	5	1.01	1888.8	0.2260	417.8	2306.6

Table F.2: Thrust data from combined heave and surge simulations (aligned)

Case nr.	Mean T (kN)	Amp. T (kN)	Max. T (kN)
1	482.6	10.9	471.7
2	482.9	32.4	450.6
3	483.6	53.3	430.3
4	439.7	10.0	429.7
5	439.9	29.8	410.1
6	440.5	49.2	391.3
7	325.4	7.9	317.5
8	325.5	23.2	302.2
9	325.7	38.3	287.4
10	173.7	11.6	185.3
11	178.3	16.2	194.5
12	178.3	24.7	204.2

Appendix G

Combined Surge and Heave (Unaligned)

Table G.1: Power data of combined heave and surge simulations (unaligned)

Case nr.	Ψ (deg)	$\hat{A}_{\text{heave}}$ (m)	$\hat{A}_{\text{surge}}$ (m)	Mean P (kW)	Freq P (Hz)	Amp. P (kW)	Max. P (kW)
1	0	1	0.2	4620.7	0.1100	118.2	4738.9
2	0	3	0.61	4625.2	0.1107	369.7	4994.9
3	0	5	1.01	4633.8	0.1107	614.4	5248.2
4	15	1	0.2	4299.9	0.1087	115.2	4415.1
5	15	3	0.61	4303.3	0.1100	357.7	4661.0
6	15	5	1.01	4309.7	0.1107	594.0	4903.7
7	30	1	0.2	3363.1	0.1164	108.4	3471.5
8	30	3	0.61	3365.2	0.1068	323.2	3688.4
9	30	5	1.01	3368.0	0.1081	533.3	3901.3
10	45	1	0.2	1828.8	0.1194	168.9	1997.7
11	45	3	0.61	1885.2	0.1038	289.7	2174.9
12	45	5	1.01	1886.0	0.1056	462.0	2348.0

Table G.2: Thrust data of heave and surge simulations (unaligned)

Case nr.	Mean T (kN)	Amp. T (kN)	Max. T (kN)
1	482.5	10.1	472.5
2	482.9	31.6	451.3
3	483.5	52.5	431.0
4	439.6	9.4	430.2
5	439.9	29.3	410.6
6	440.4	48.6	391.8
7	325.3	7.7	317.5
8	325.4	23.2	302.2
9	325.6	38.3	287.3
10	175.6	8.8	184.4
11	178.1	16.2	194.3
12	178.1	25.8	203.9

Appendix H

Combined Heave and Pitch

Table H.1: Power data of combined heave and pitch simulations

Case nr.	Ψ (deg)	$\hat{A}_{\text{heave}}$ (m)	$\hat{A}_{\text{pitch}}$ (deg)	Mean P (kW)	Freq P (Hz)	Amp. P (kW)	Max. P (kW)
1	0	1	0.06	4615.4	0.1087	61.3	4676.7
2	0	3	0.17	4614.0	0.1087	166.1	4780.1
3	0	5	0.28	4612.0	0.1094	270.6	4882.6
4	15	1	0.06	4294.7	0.1062	59.2	4353.9
5	15	3	0.17	4293.0	0.1094	160.6	4453.6
6	15	5	0.28	4290.4	0.1100	262.1	4552.5
7	30	1	0.06	3312.1	0.1015	12.7	3324.8
8	30	3	0.17	3353.0	0.2370	202.5	3555.5
9	30	5	0.28	3346.8	0.1056	237.0	3583.8
10	45	1	0.06	1839.6	0.1202	22.2	1861.8
11	45	3	0.17	1770.1	0.1186	32.7	1802.8
12	45	5	0.28	1864.1	0.1186	209.0	2073.1

Table H.2: Thrust data of combined heave and pitch simulations

Case nr.	Mean T (kN)	Amp. T (kN)	Max. T (kN)
1	482.1	5.2	476.8
2	481.8	14.2	467.7
3	481.5	23.1	458.4
4	439.2	4.8	434.4
5	438.9	13.1	425.9
6	438.5	21.3	417.2
7	324.9	4.0	320.8
8	324.5	10.4	314.1
9	323.9	16.8	307.1
10	175.8	1.0	174.8
11	171.8	1.4	170.4
12	176.9	11.1	165.8

Appendix I

Combined Surge and Pitch

Table I.1: Power data of combined surge and pitch simulations

Case nr.	Ψ (deg)	$\hat{A}_{\text{surge}}$ (m)	$\hat{A}_{\text{pitch}}$ (deg)	Mean P (kW)	Freq P (Hz)	Amp. P (kW)	Max. P (kW)
1	0	0.20	0.06	4613.9	0.1100	141.5	4755.4
2	0	0.61	0.17	4613.7	0.1107	431.2	5044.9
3	0	1.01	0.28	4613.3	0.1107	711.1	5324.4
4	15	0.20	0.06	4296.6	0.1100	136.5	4433.1
5	15	0.61	0.17	4295.7	0.1107	415.4	4711.1
6	15	1.01	0.28	4295.4	0.1107	684.7	4980.1
7	30	0.20	0.06	3361.0	0.1156	153.3	3514.3
8	30	0.61	0.17	3359.0	0.1087	368.6	3727.6
9	30	1.01	0.28	3358.6	0.1094	604.9	3963.5
10	45	0.20	0.06	1797.4	0.2370	401.9	2199.3
11	45	0.61	0.17	1874.0	0.1044	299.1	2173.1
12	45	1.01	0.28	1872.6	0.1062	486.6	2359.2

Table I.2: Thrust data of combined surge and pitch simulations

Case nr.	Mean T (kN)	Amp. T (kN)	Max. T (kN)
1	482.0	12.1	469.9
2	482.0	36.9	445.1
3	482.0	60.8	421.2
4	439.2	11.2	428.0
5	439.1	34.1	405.0
6	439.1	56.2	382.9
7	325.0	11.3	313.7
8	324.9	26.9	298.0
9	324.9	44.3	280.6
10	176.4	4.7	171.7
11	177.9	17.7	160.2
12	177.8	28.9	148.9

Appendix J

Combined Heave, Surge and Pitch

Table J.1: Simulation parameters for heave, surge and pitch

Case nr.	Ψ (deg)	$\hat{A}$heave (m)	$\hat{A}$surge (m)	$\hat{A}_{\text{pitch}}$ (deg)
1	0	1	0.20	0.5
2	0	3	0.61	1.6
3	0	5	1.01	2.7
4	15	1	0.20	0.5
5	15	3	0.61	1.6
6	15	5	1.01	2.7
7	30	1	0.20	0.5
8	30	3	0.61	1.6
9	30	5	1.01	2.7
10	45	1	0.20	0.5
11	45	3	0.61	1.6
12	45	5	1.01	2.7

Table J.2: Power data of combined heave, surge and pitch simulations

Case nr.	Mean P (kW)	Freq P (Hz)	Amp. P (kW)	Max. P (kW)
1	4614.5	0.1107	142.3	4756.8
2	4618.6	0.1107	433.2	5051.8
3	4627.9	0.1107	713.0	5340.9
4	4296.9	0.1100	136.5	4433.4
5	4301.2	0.1107	414.8	4716.0
6	4310.7	0.1114	682.4	4993.1
7	3361.5	0.1156	150.1	3511.6
8	3363.4	0.1114	363.7	3727.1
9	3371.6	0.1114	596.1	3967.7
10	1799.7	0.1095	194.5	1994.2
11	1876.8	0.1163	284.5	2161.3
12	1881.2	0.1135	462.8	2344.0

Table J.3: Thrust data of combined heave, surge and pitch simulations

Case nr.	Mean T (kN)	Amp. T (kN)	Max. T (kN)
1	482.0	12.1	469.9
2	482.5	37.0	445.5
3	483.5	60.9	422.6
4	439.2	11.3	427.9
5	439.6	34.3	405.3
6	440.4	56.3	384.1
7	325.0	11.2	313.8
8	325.2	27.2	298.0
9	325.8	44.6	281.2
10	178.0	6.4	171.6
11	178.1	18.0	160.1
12	178.4	29.3	149.1

Appendix K

Wave Effect on the Output Power

Table K.1: Power data of wave effect on the output power

Case nr.	Ψ (deg)	A_{wave} (m)	Mean P (kW)	Freq P (Hz)	Amp. P (kW)	Max. P (kW)
1	0	5	4733.4	0.2000	6.2	4739.6
2	0	10	4836.8	0.2300	15.6	4852.3
3	0	15	4953.4	0.1590	26.5	4980.0

Table K.2: Thrust data of the wave effect on the output power

Case nr.	Mean T (kN)	Amp. T (kN)	Max. T (kN)
1	491.8	0.3	491.5
2	500.2	0.8	499.3
3	509.6	1.4	508.2

Appendix L

Full FOWT Simulations

Table L.1: Power data of full FOWT simulations

Case nr.	Mean P (kW)	Freq P (Hz)	Amp. P (kW)	Max. P (kW)
1	4652.4	0.2000	0.2	4652.6
2	4652.8	1.6600	3.5	4656.3
3	4653.1	1.3100	0.1	4653.2

Table L.2: Thrust data of full FOWT simulations

Case nr.	Mean T (kN)	Amp. T (kN)	Max. T (kN)
1	478.7	10.3	468.4
2	485.6	0.2	485.4
3	485.7	0.0	485.7

Bibliography

[1] Vestas:vestas v236-15.0 mw wind turbine. `https://www.vestas.com/en/products/offshore/V236-15MW`, 2024. Accessed: March 2024.

[2] U.S. Department of Energy. Offshore wind market report: 2021 edition. Technical report, U.S. Department of Energy, 2021. Accessed: March 2024.

[3] K.S. Hansen, R.J. Barthelmie, L.E. Jensen, and A. Sommer. The impact of turbulence intensity and atmospheric stability on power deficits due to wind turbine wakes at horns rev wind farm. *Wind Energy*, 15(1):183–196, 2012.

[4] Equinor ASA. Hywind tampen. `https://www.equinor.com/energy/hywind-tampen`, 2021. Accessed: March 2024.

[5] S-H. Ju, Y-C. Huang, and Y-Y. Huang. Study of optimal large-scale offshore wind turbines. *Renewable Energy*, 154:161–174, 2020.

[6] J. Leishman. Challenges in modeling the unsteady aerodynamics of wind turbines. *Wind Energy*, 5:85–132, 2002.

[7] H. Glauert. *Airplane Propellers*, pages 169–360. Springer Berlin Heidelberg, Berlin, Heidelberg, 1935.

[8] J. Hernández and A. Crespo. Aerodynamic calculation of the performance of horizontal axis wind turbines and comparison with experimental results. *Wind Engineering*, 11(4):177–187, 1987. Accessed March 2024.

[9] M.O.L. Hansen. *Aerodynamics of Wind Turbines: second edition*. Earthscan, 2 edition, 2008.

[10] T. Sant and K. Cuschieri. Comparing three aerodynamic models for predicting the thrust and power characteristics of yawed floating wind turbine rotors. *Journal of Solar Energy Engineering*, 138, 2016.

[11] B.A. Roccia. Introduction to aerodynamics of wind turbines, 2024. Course: Energi321, University of Bergen, Online; accessed 15 May 2024.

[12] K. Karamcheti. *Principles of Ideal-fluid Aerodynamics*. Wiley, 1966.

[13] H. Bui, M. Bakhoday-Paskyabi, and M. Mohammadpour-Penchah. Implementation of a simple actuator disc for large eddy simulation (sadles-v1.0) in the weather research and forecasting model (v4.3.1) for wind turbine wake simulation. *EGUsphere*, 2023:1–24, 2023.

[14] M.L. Verstraete, L.R. Ceballos, C. Hente, B.A. Roccia, and C.G. Gebhardt. Code-to-code benchmark for simulation tools based on the unsteady vortex-lattice method. *Journal of Aerospace Information Systems*, 20(11):719–746, 2023.

[15] B.A. Roccia, S. Preidikman, J.C. Massa, and D.T. Mook. Modified unsteady vortex-lattice method to study flapping wings in hover flight. *AIAA Journal*, 51(11):2628–2642, 2013.

[16] M.L. Verstraete, S. Preidikman, B.A. Roccia, and D.T. Mook. A numerical model to study the nonlinear and unsteady aerodynamics of bioinspired morphing-wing concepts. *International Journal of Micro Air Vehicles*, 7:327–345, 2015.

[17] C.G. Gebhardt, S. Preidikman, and J.C. Massa. Numerical simulations of the aerodynamic behavior of large horizontal-axis wind turbines. *International Journal of Hydrogen Energy*, 35(11):6005–6011, 2010. 3rd Argentinean and 2nd Latin American Congress in Hydrogen and Sustainable Energy Sources.

[18] C.G. Gebhardt and B.A. Roccia. Non-linear aeroelasticity: An approach to compute the response of three-blade large-scale horizontal-axis wind turbines. *Renewable Energy*, 66(C):495–514, 2014.

[19] B.A. Roccia, L.R. Ceballos, M.L. Verstraete, and C.G. Gebhardt. Development and application of a mesh generator intended for unsteady vortex-lattice method simulations of wind turbines and wind farms. *Wind Energy Science*, 9:385–416, 2024.

[20] A. Betz. The maximum of the theoretically possible exploitation of wind by means of a wind motor. *Wind Engineering*, 37, 2013.

[21] J. Perkins. Book review: Renewable energy: A first course. robert ehrlich, 2013. crc press, boca raton, fl. 442 pages, hardcover. isbn 978-1-4398-6115-8. $104.95. *Environmental Practice*, 15:483–484, 2014.

[22] N.F. Smith. Bernoulli and newton in fluid mechanics. *Physics Teacher*, 1972. Retrieved from ProQuest.

[23] M. Salem. *Design of a pitch angle control system for a horizontal axis small wind turbine*. PhD thesis, 2016.

[24] I. Tuncer and M. Platzer. *A computational study of flow separation characteristics and wake profiles behind a flapping airfoil*. 1999.

[25] K. Karamcheti. *Principles of Ideal-fluid Aerodynamics*. Wiley, 1966.

[26] J. Katz and A. Plotkin. *Low-Speed Aerodynamics*. Cambridge Aerospace Series. Cambridge University Press, 2001.

[27] C. Hente, B.A. Roccia, R. Rolfes, and C.G. Gebhardt. Analytical linearization of aerodynamic loads in the uvlm for nonlinear aeroelastic applications. *AIAA Journal, In Press*, 2024.

[28] M. Bhagwat and J. Leishman. Generalized viscous vortex model for application to free-vortex wake and aeroacoustic calculations. *58th Annual Forum and Technology Display of the American Helicopter Society International*, 2002.

[29] H.B. Squire. The growth of a vortex in turbulent flow. *Aeronautical Quarterly*, 16:302–306, 1965.

[30] S. Ananthan and J. Leishman. Role of filament strain in the free-vortex modeling of rotor wakes. *Journal of The American Helicopter Society - J AMER HELICOPTER SOC*, 49, 2004.

[31] B.A. Roccia, M.L. Verstraete, O. Brüls, G. Dimitriadis, and S. Preidikman. *Unsteady aerodynamics and nonlinear dynamics of free-falling rotating seeds*, page 15. 2018.

[32] M.L. Verstraete, S. Preidikman, B.A. Roccia, and D.T. Mook. A numerical model to study the nonlinear and unsteady aerodynamics of bioinspired morphing-wing concepts. *International Journal of Micro Air Vehicles*, 7(3):327–345, 2015.

[33] J. Lee. A potential based panel method for the analysis of marine propellers in steady flow. *Ph.D. Dissertation, Massachusetts Inst. of Technology, Cambridge, MA*, 1987.

[34] B. Cocciaro, S. Faetti, and C. Festa. Experimental investigation of capillarity effects on surface gravity waves: non-wetting boundary conditions. *Journal of Fluid Mechanics*, 246:43–66, 1993.

[35] R.L. Jaffe and W. Taylor. *The Physics of Energy*. Cambridge University Press, 2018.

[36] Analytic geometry of some rectilinear figures. *International Journal of Mathematical Education in Science and Technology*, 23(6):895–913, 1992.

[37] C. Bak, F. Zahle, R. Bitsche, T. Kim, A. Yde, L.C. Henriksen, P.B. Andersen, A. Natarajan, and M.H. Hansen. Design and performance of a 10 mw wind turbine. *Wind Energy*, 124, 2013.

[38] Sandia Report, Daniel Todd Griffith, and Thomas D. Ashwill. The sandia 100-meter all-glass baseline wind turbine blade: Snl100-00. 2011.

[39] B.R. Resor. Definition of a 5mw/61.5m wind turbine blade reference model. 2013.

[40] J. Jonkman, S. Butterfield, W. Musial, and G. Scott. Definition of a 5-mw reference wind turbine for offshore system development. 2009.

[41] C.G. Gebhardt. *Desarrollo de simulaciones numéricas del comportamiento aeroelástico de grandes turbinas eólicas de eje horizontal*. PhD thesis, 2012.

[42] C. Bak, F. Zahle, R. Bitsche, T. Kim, A. Yde, L.C. Henriksen, M. H. Hansen, J. P. A. A. Blasques, Mac G., and A. Natarajan. The dtu 10-mw reference wind turbine, 2013. Danish Wind Power Research 2013 ; Conference date: 27-05-2013 Through 28-05-2013.

[43] Z. Xiao, B. Wu, M. Wang, Q. Hu, and W. Yang. Investigation of the influence of blocking effect on the aerodynamic and hydrodynamic characteristics of a powered aircraft model. *IOP Conference Series: Materials Science and Engineering*, 751:012013, 2020.